



UNIVERSITÀ
DEGLI STUDI
DI PADOVA

University of Padova

Department of Chemical Sciences

Ph.D. SCHOOL IN: MATERIALS SCIENCE AND ENGINEERING

CYCLE: XXIX

Magneto-plasmonic nanostructures based on laser ablated nanoparticles of Au and
 FeO_x for nanomedicine applications

School director : Ch.mo Prof. Gaetano Granozzi

Supervisor : Ch.mo Prof. Moreno Meneghetti

PhD Student: Fabrizio Bertorelle

Table of contents

Abstract	1
Chapter 1	3
An introduction to nanotechnology	5
Nanoparticles.....	6
Nanomedicine	7
Cancer nanotechnology	15
Gold nanoparticles in cancer research	16
Iron oxide nanoparticles in cancer research.....	18
Magneto-plasmonic nanoparticles in cancer research	20
Cancer: principal characteristics	22
Antibodies: structure and functions	23
Immune response to tumors.....	25
Prostate cancer.....	26
Synthesis of nanoparticles: top-down and bottom-up methods	27
Gold nanoparticles	29
Synthesis strategies.....	30
Localized surface plasmon resonance (LSPR)	32
Surface enhanced Raman scattering (SERS)	37
Plasmonic photothermal effect	44
Iron oxide nanoparticles	46
Synthesis strategies.....	48
Magnetic properties	51
Chemical properties.....	54
<i>A sol-gel approach to surface modification</i>	56
Common synthesis for magneto-plasmonic materials	59
The importance of being green: Laser Ablation Synthesis in Solution	67
Aim of this thesis	75
References	77
Chapter 2	89
Gold and iron oxide nanoparticles aggregates for cell guiding and sorting	91
Synthesis of AuFeO_x nanoclusters	92
Results	95
In vitro application	101
Conclusion	103

Table of contents

References	105
Chapter 3	109
FeO_xNP@dye-doped Silica@AuNP core-shell-satellite nanostructures.....	111
Synthesis of core-shell-satellite nanostructures	113
Synthesis of gold and iron oxide nanoparticles	113
Assembling of antibody functionalized core-shell-satellite (CSS-Ab) nanostructures	113
Characterization of antibody functionalized core-shell-satellite (CSS-Ab) nanostructures	116
Immunomagnetic sorting of cancer cells	122
Methods.....	122
Results.....	123
Photothermal treatment of cancer cells.....	132
Experimental section	133
Results	135
<i>Hydrogel</i>	<i>135</i>
<i>Irradiation of PSMA+ (PC3-PIP) cells not incubated with CSS-Ab</i>	<i>137</i>
<i>Effect of irradiation time on PSMA+ (PC3-PIP) cells.....</i>	<i>139</i>
<i>Photothermal effect on adherent cells.....</i>	<i>139</i>
<i>Evaluation of bystander effect.....</i>	<i>141</i>
From core-shell-satellite to core-shell-shell: tuning the plasmon to NIR	143
Methods.....	143
Results	144
Conclusion.....	147
References	149
Conclusion	153
Publications and conferences.....	153
Aknowledgements.....	157

Abstract

In the last years, gold and iron oxide nanoparticles have received an increasing interest in nanomedicine and biotechnology thanks to their properties. Gold nanoparticles (AuNPs) are biocompatible and possess useful optical properties that make them a powerful imaging tool using, for example, SERS spectroscopy. On the other hand, iron oxide nanoparticles (FeO_xNPs , in particular those made of magnetite) are interesting because of their magnetic properties. Combining gold and iron oxide nanoparticles in a unique system, one obtains a magneto-plasmonic material in which the characteristics properties of the two nanoparticles are present. The use of magneto-plasmonic nanostructured materials in nanomedicine is a quite young research topic and one of the reasons is the elaborated synthesis often required. Several passages are needed also for the purification of these nanosystem from chemicals used during synthesis, which is a crucial point when the final application is in nanomedicine or nanobiology. In this work we will show the synthesis of two magneto-plasmonic systems made of gold and iron oxide nanoparticles. AuNPs and FeO_xNPs are synthesized with the laser ablation synthesis in solution (LASiS) method. LASiS is a green chemistry method, which allows to obtain chemical-free and stable nanoparticles in water solution. With LASiS, purification passages are unnecessary or reduced to a minimum and no chemicals that could interfere in biological environment are present. In chapter 2 it will be reported the synthesis of gold and iron oxide nanoclusters (AuFeO_xNC) in which the aggregation between particles is performed without the use of chemicals, but exploiting the surface charges of nanoparticles. The use of such nanoclusters in cells guiding and sorting and imaging will be also shown.

In chapter 3, the synthesis of another magneto-plasmonic system in which AuNPs and FeO_xNPs are arranged in a core-shell-satellite structure, is reported. Also in this case, purification passages are reduced thanks to the laser ablation synthesis. This system is conjugated with an antibody and shows high performance in immunomagnetic sorting and photothermal treatment of cancer cells.

The arguments developed in the thesis are introduced in the first chapter.

Abstract

Chapter 1



An introduction to nanotechnology

The word “nanotechnology” is nowadays being listened and read more and more often also in non-specialist sources like, for example, newspaper, television news and in all that journals that write about science for a non-scientist audience. For a layman it could be difficult to visualize the “nano” dimension; however the interest for this branch of science is clearly present for the perspectives that can be perceived.

The concept of manipulating atoms at the nanoscale was first introduced by Richard Feynman in 1959 in his lecture “*There’s plenty of a room at the bottom*”¹ in which he described the possibility of synthesis directly manipulating atoms. However, the term “nanotechnology” was first used by a Japanese scientist called Norio Taniguchi in a conference², to describe semiconductor processes such as thin film deposition and ion beam milling with a control of the order of nanometer. The term was later used by K. Eric Drexler which, inspired by Feynman, proposed the idea of a nanoscale assembler able to replicate itself with atomic precision in his book “*Engines of Creation: The Coming Era of Nanotechnology*”.³ Nanotechnology had a bootstrap in 1981 with the invention of the scanning tunneling microscope (STM) by Gerd Binnig and Heinrich Rohrer at IBM Zurich Research Laboratory.^{4,5} STM, which is based on the concept of quantum tunneling, can be used for imaging of surfaces with atomic resolution and also to manipulate atoms: in 1989 Don Eigler and co-workers at the IBM Research Lab in Almaden, California, used an STM to write the IBM logo with 35 xenon atoms on a nickel surface (Figure 1.1).⁶

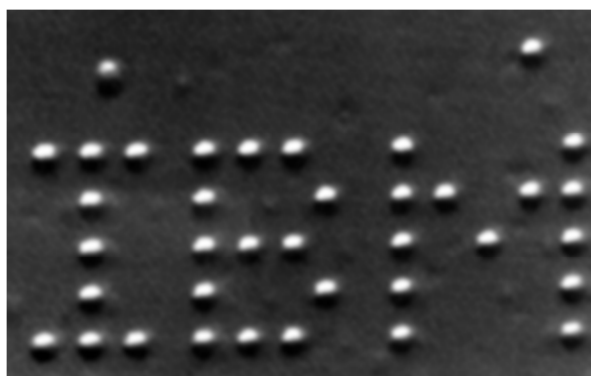


Figure 1.1 IBM logo wrote using a STM microscope.

Thanks to advances in technology it was possible to observe the nano dimension and to control it.

Few years later these advances in technology leads to the discovery of fullerenes (C_{60}) and carbon nanotubes, new promises for semiconductor science.⁷

Although it seems nanotechnology has its first development in '80s, scientists (and not only scientists) have been dealing with nanomaterials long time before, for example when scientific studies, like those of Faraday on colloidal solutions, were conducted in the XIX century.

Nanoparticles

Nanoparticles (NPs) are objects with nanometric size, usually in the range of 1-100 nm. At the beginnings they weren't associated to nanotechnology because they were studied in an interdisciplinary science between physics and chemistry called interface and colloids science (which includes also particles of dimensions up to 1000 nm). NPs have a long history, in particular those made of gold and silver because of the most attractive properties among all metal nanoparticles. Gold nanoparticles (AuNPs) are found in the 4-th century Lycurgus cup in which they affect the color of the glass depending on the location of the light source.⁸ Gold, silver and copper nanoparticles were often used in glazes or glasses to obtain different colors since bronze ages.⁹ In middle ages, AuNPs solutions were believed to have curative properties to various diseases. In 1618 Francisci Antonii, philosopher and member of medical profession, wrote a book entitled "Panacea Aurea, sive tractatus duo de ipsius Auro Potabili" ("Gold potion, or two treatments of potable gold").¹⁰ The first to provide a scientific description of gold nanoparticles was Michael Faraday in 1850s: in 1857 he prepared the first pure sample of colloidal gold reducing gold chloride with phosphorus and, subsequently, he recognized that the typical ruby red color of AuNPs was due to the reduced size of gold.¹¹ Apart from Faraday other pioneering studies on gold nanoparticles were conducted by R.A. Zsigmondy, who coined the term "nanometer" for characterize particle size¹² and Gustav Mie, who provided the theory for scattering and absorption by spherical particles.¹³ Research on nanoparticles accelerated in the first decades of '900 with advances in technology, as happened with nanotechnology, in particular with the development of electron microscopy and atomic force microscopy. Although AuNPs were and are the most studied type of NPs (thanks to their attractive properties and their easy synthesis), nowadays nanoparticles can be made of many different materials with many different methods and shape and they can be either suspended in solvents (generically called

colloidal solutions) or used in powder as well. They are interesting because chemical and physical properties of nanoparticles strongly depend on the material they are made and can differ a lot from those of the bulky material. For example, thanks to their dimension, they have a high surface to volume ratio (1 kg of particles of 1 mm^3 has the same surface area as 1 mg of particles of 1 nm^3) which make them suitable, for example, for uses in catalysis where a large accessible surface is preferred.¹⁴ Applications of NPs in biological and medical fields are also very common thanks to their nanometric size, which makes possible to have, to control and to study direct interactions with tissues at subcell levels.¹⁴

Engineering of the surface of nanoparticles is obviously a crucial point: how they interact with the environment depends on what is present on the surface and, clearly, the surface itself has properties that differ depending on the material. In this thesis we will focus on nanoparticles, in particular those made of gold and iron oxide, for biomedical application. So we will see why these two materials are important for this kind of applications, how they can interact with biological environment and how their surface can be engineered for new useful properties. Having different materials different properties and being possible to modify their surface, a lot of applications can be foreseen.

Nowadays nanoparticles gave a great boost to nanoscience and find applications in chemical industry¹⁵, pharmaceuticals, biotechnology, medicals^{16,17}, microfluidics, semiconductors among others.

Nanomedicine

Since researches on nanoparticles began to establish, the understanding of their importance in biology and medicine was only a matter of time. In January 2000 the US president Bill Clinton announced an investment of \$475 million on nanotechnology research development via the National Nanotechnology Initiative (NNI).¹⁸ Investments in NNI reached about \$1500 million in 2014-2016 with a 30% for the Department of Health and Human Services (DHHS).¹⁹

Chapter 1

Nanomedicine was a new field emerging from the interest of applying nanotechnology to medicine. The purpose is that of diagnoses, treating and preventing diseases and traumatic injury, relieving pain, improving and preserving human health using molecular tools and knowledge of the human body.

The field of nanomedicine has been rapidly expanding since first years of 2000, Table 1.1 gives an idea of the many directions in which researches on nanomedicine are splitted.¹⁸

A partial nanomedicine technologies taxonomy

Raw nanomaterials	Cell simulations and cell diagnostics	Biological research
Nanoparticle coatings	Cell chips	Nanobiology
Nanocrystalline materials	Cell simulators	Nanoscience in life sciences
Nanostructured materials	DNA manipulation, sequencing, diagnostics	Drug delivery
Cyclic peptides	Genetic testing	Drug discovery
Dendrimers	DNA microarrays	Biopharmaceutics
Detoxification agents	Ultrafast DNA sequencing	Drug delivery
Fullerenes	DNA manipulation and control	Drug encapsulation
Functional drug carriers		Smart drugs
MRI scanning (nanoparticles)	Tools and diagnostics	
Nanobarcodes	Bacterial detection systems	Molecular medicine
Nanoemulsions	Biochips	Genetic therapy
Nanofibers	Biomolecular imaging	Pharmacogenomics
Nanoparticles	Biosensors and biodetection	
Nanoshells	Diagnostic and defense applications	Artificial enzymes and enzyme control
Carbon nanotubes	Endoscopic robots and microscopes	Enzyme manipulation and control
Noncarbon nanotubes	Fullerene-based sensors	
Quantum dots	Imaging (cellular, etc.)	Nanotherapeutics
	Lab on a chip	Antibacterial and antiviral nanoparticles
Artificial binding sites	Monitoring	Fullerene-based pharmaceuticals
Artificial antibodies	Nanosensors	Photodynamic therapy
Artificial enzymes	Point of care diagnostics	Radiopharmaceuticals
Artificial receptors	Protein microarrays	
Molecularly imprinted polymers	Scanning probe microscopy	Synthetic biology and early nanodevices
		Dynamic nanoplatform "nanosome"
Control of surfaces	Intracellular devices	Tecto-dendrimers
Artificial surfaces—adhesive	Intracellular assay	Artificial cells and liposomes
Artificial surfaces—nonadhesive	Intracellular biocomputers	Polymeric micelles and polymersomes
Artificial surfaces—regulated	Intracellular sensors/reporters	
Biocompatible surfaces	Implants inside cells	Biotechnology and biorobotics
Biofilm suppression		Biologic viral therapy
Engineered surfaces	BioMEMS	Virus-based hybrids
Pattern surfaces (contact guidance)	Implantable materials and devices	Stem cells and cloning
Thin-film coatings	Implanted bioMEMS, chips, and electrodes	Tissue engineering
	MEMS/Nanomaterials-based prosthetics	Artificial organs
Nanopores	Sensory aids (artificial retina, etc.)	Nanobiotechnology
Immunoisolation	Microarrays	Biorobotics and biobots
Molecular sieves and channels	Microcantilever-based sensors	
Nanofiltration membranes	Microfluidics	Nanorobotics
Nanopores	Microneedles	DNA-based devices and nanorobots
Separations	Medical MEMS	Diamond-based nanorobots
	MEMS surgical devices	Cell repair devices

Table 1.1 Application of nanotechnology to medicine led to the appearance of many topics of research.¹⁸

In a very general way we can divide researches in nanomedicine in the following four topics:

1. Nanomedicine applications for use inside the body: this include, for example, anticancer drugs, gene therapy or prostheses applications of nanotechnologic materials.

2. Nanomedicine applications for diagnostic techniques: some examples are nanoparticle biolabels, nanoscale visualization, biochips/microarrays, nanoproteomic-based diagnostics, nanoparticle-based nucleic acid diagnostics, nanoparticle-based immunoassays, DNA nanomachines, nanobiosensors, biobarcode assays, and nanopore technology.²⁰
3. Nanomedicine in drug based approaches: in this case nanostructured materials are used as vectors to deliver drugs specifically to damaged or unhealthy tissues.²¹⁻²³
4. Lab-on-a-chip techniques: here nanostructured materials can be used to build or to operate in small devices (that usually have the sizes of millimeters/centimeters) which incorporate numerous laboratory tasks. Healthcare services can use Lab-on-a-chip technology to check patients at point-of-care facilities or in remote or resource-poor locations, therefore reducing checking time from days to minutes.²⁴

There are five general steps in the development of nanomedicine (Figure 1.2). This means that although the literature is very extensive on this argument, due to the novelty of the field, nanomedicine products that are currently under clinical investigation or already commercialized are no more than a pair of hundreds.

Most of these products are nanoparticles²⁵ which we can divide in two main groups:

1. Hard nanoparticles
2. Soft nanoparticles

Hard nanoparticles used in nanomedicine, as the name suggests, consists of gold, silver, iron oxide, ceramic and carbon. Soft nanoparticles, in contrast to hard NPs, includes liposomes, micelles, dendrimers, emulsions, protein and polymeric nanostructures.²⁵

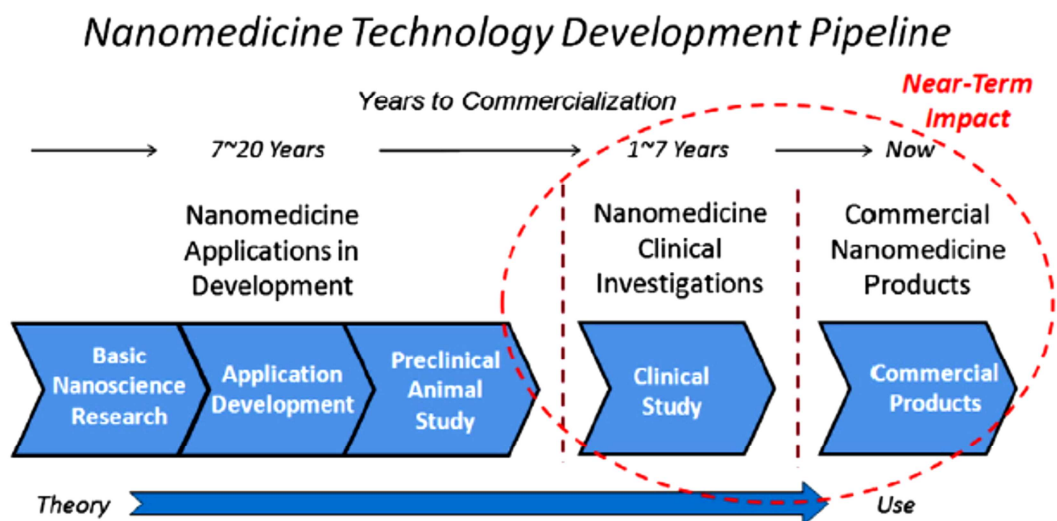


Figure 1.2 General steps in the development of nanomedicine. Approved or under clinical investigations products will have the strongest impact on the direction of nanomedicine.²⁵

Table 1.2 provides an outlook on the type of nanostructures for nanomedicine products approved by FDA in diverse development status (investigational or commercial). It is interesting to notice the relevance of hard nanoparticles in commercial products and of soft nanoparticles (in particular liposomes) in investigational products.

Nanocomponent	Investigational			Commercial		
	Therapeutic	Device	Total	Therapeutic	Device	Total
Hard NP	3	12	15	0	28	28
Nanodispersion	5	0	5	1	1	2
Polymeric NP	23	0	23	9	0	9
Protein NP	4	0	4	2	0	2
Liposome	53	0	53	7	1	8
Emulsion	18	1	19	9	0	9
Micelle	8	0	8	3	1	4
Dendrimer / Fleximer	2	2	4	0	3	3
Virosome	6	0	6	2	0	2
Nanocomposite	0	0	0	0	18	18
NP Coating	0	2	2	0	6	6
Nanoporous Material	0	3	3	0	2	2
Nanopatterned	0	2	2	0	2	2
Quantum Dot	0	1	1	0	4	4
Fullerene	0	1	1	0	0	0
Hydrogel	0	0	0	0	1	1
Carbon Nanotube	0	1	1	0	0	0
Totals	122	25	147	33	67	100

Table 1.2 Type of nanostructures for confirmed and likely nanomedicine applications and products, by development status.²⁵

Applications of these nanomedicine products can be as therapeutics or as devices. The first one refers to products that intend to directly remedy a medical condition (i.e. cancer treatment, diseases and disorders of various types). Devices category includes for example products for *in vitro* testing, *in vivo* imaging, *in vivo* device coatings, medical dressing/textiles and others.

Regarding therapeutics applications, most of nanomedicine products are for cancer treatment: in particular two-third of the investigational products are for cancer treatment while the number of approved commercial products are quite the same for each category (Figure 1.3A). Regarding their use as device, *in vitro* testing and *in vivo* imaging seems to be the more promising categories (Figure 1.3B).

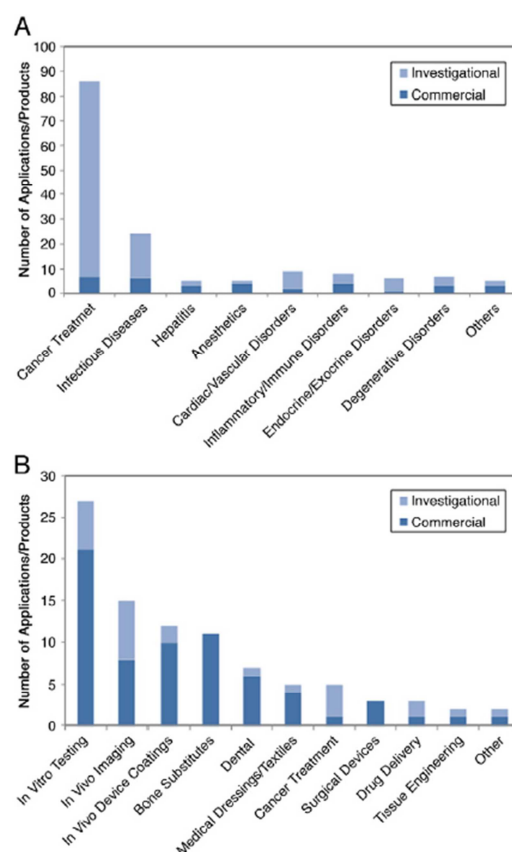


Figure 1.3 Medical uses for confirmed and likely therapeutics (A) and devices (B).²⁵

One of the most relevant biomedical characteristics of nanostructured materials are the unique biodistribution profiles they achieve once administered, which is not possible with conventional molecular or microscale delivery. Nanosystems can be appositely designed to target specific tissues or areas of the body. Confirmed and likely applications and products mainly focus on intravenous administration (73%,

Figure 1.4). After administration a nanosystem can behave in different manner depending of the sophistication of targeting, which is distinguished in passive or active.

The passive targeting is used by those nanosystems which take advantage of the enhanced permeability and retention (EPR) effect, a size and geometry dependent mode of action. On the other side the active targeting uses mechanisms that are beyond the simple dependency by size and geometry to enhance preferential delivery to a specific tissue or area of the body. Usually active targeting nanostructures are functionalized with ligands (like antibodies) which bind to specific receptors. Anyway most of the nanomedicine confirmed, and likely intravenous-administered products, make use of the passive targeting (Figure 1.4).²⁵

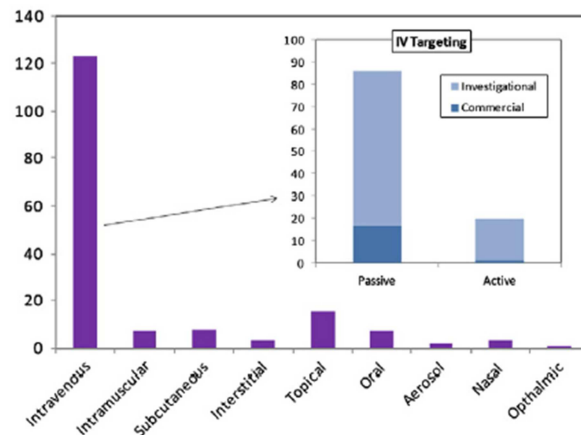


Figure 1.4 Different routes of administration for confirmed and likely nanomedicine products. Most of intravenous-administered products make use of passive targeting.²⁵

To finish this brief overlook on nanomedicine it's appropriate to make some observations on currently commercialized nanomedical products.

Table 1.3 summarizes products that have been approved by FDA in last years. Most of these are nanoparticles. Hydroxapatite nanocrystals are used as bone substitutes, ceramic or silica nanoparticles find their use in dentistry, silver nanoparticles exploit their antimicrobial activity as device or dressing coatings. The thesis focuses in particular on gold or iron oxide nanoparticles based structures. As reported in table 1.3, these nanoparticles are only used for in vitro assay applications. Magnetic nanoparticles (CellTrack[®], CellSearch[®]) functionalized with an antibody are used to magnetically select cells (active targeting) with a technique called immunomagnetic sorting. On the other side, optical properties of antibody-labeled gold nanoparticles

(NicAlert, Verigene) are used for the detection of biomarkers. In this thesis we will see the possibility of combining both iron oxide and gold nanoparticles properties in a unique system.

Use	Application(s)/Product(s)	Company	Approval Year	Nanocomponent Description
Bone Substitute	Vitoss [14]	Orthovita	2003	100-nm Calcium-Phosphate Nanocrystals
	Ostim [87]	Osartis	2004	20-nm Hydroxapatite Nanocrystals
	OsSatura [62]	Isotis Orthobiologicals US	2003	Hydroxapatite Nanocrystals
	NanOss [77]	Angstrom Medica, Inc.	2005	Hydroxapatite Nanocrystals
	Alpha-bsm, Beta-bsm, Gamma-bsm, EquivaBone, CarriGen [92]	ETEX Corporation	2009	Hydroxapatite Nanocrystals
Dental Composite	Ceram X Duo [94]	Dentsply	2005	Ceramic NPs
	Filtek [95]	3M Company	2008	Silica and Zirconium NPs
	Premise [14]	Sybron Dental Specialties	2003	"Nanoparticles"
	Nano-Bond [96]	Pentron® Clinical Technologies, LLC	2007	"Nanoparticles"
Device Coating	ON-Q SilverSoaker / SilvaGard™ [97]	I-Flow Corporation / AcryMed, Inc.	2005	Antimicrobial Nanosilver
	EnSeal Laparoscopic Vessel Fusion [39]	Ethicon Endo-Surgery, Inc.	2005	NP-Coated Electrode
In Vitro Assay	NanoTite Implant [98]	Biomet	2008	Calcium Phosphate Nanocrystal Coating
	CellTracks® [14]	Immunicon Corporation	2003	Magnetic NPs
	NicAlert [14]	Nymox	2002	Colloidal Gold
	Stratus CS [62]	Dade Behring	2003	Dendrimers
	CellSearch® Epithelial Cell Kit [99]	Veridex, LLC (Johnson & Johnson)	2004	Iron Oxide NPs
	Verigene [100,101]	Nanosphere, Inc.	2007	Colloidal Gold
	MyCare™ Assays [102]	Saladax Biomedical	2008	"Nanoparticles"
Medical Dressing	Acticoat® [97,103]	Smith & Nephew, Inc.	2005	Antimicrobial Nanosilver
Dialysis Filter	Fresenius Polysulfone® Helixone® [104]	NephroCare	1998	Nanoporous Membrane
Tissue Scaffold	TiMESH [39]	GfE Medizintechnik GmbH	2004	30-nm Titanium Coating

Table 1.3 List of nanomedicine products approved by FDA.²⁵

We will see the application in cancer cell treatment of a nanosystem composed by AuNPs and FeO_xNPs. When a nanostructure, beyond active targeting, induce a mechanism of action beyond purely size dependent biological and chemical interactions it is said to have an "active behavior". Confirmed and likely nanomedicine products that show this behavior are listed in table 1.4.

Use	Application(s)/Product(s)	Company	Status	Nanocomponent	Active Mechanism
Solid Tumor Hyperthermia	NanoTherm [77]	MagForce Nanotechnologies AG	Approved	Iron Oxide NPs	AC Magnetic Heating
	Targeted Nano-Therapeutics [105]	Aspen Medisys, LLC. (Formerly Triton BioSystems, Inc.)	Pre-Clinical	Iron Oxide NPs	AC Magnetic Heating
	AuroShell [83]	Nanospectra Biosciences	Phase I	Gold Nanoshell	IR Laser Heating
Solid Tumor Treatment	NanoXray [77]	Nanobiotix	Phase I	Proprietary NP	X-Ray-Induced Electron Emission
In Vivo Imaging	Feridex IV, GastromarkCombidex (Ferumoxtran-10) [79,106]	Advanced Magnetics	Approved (1996)Phase III	Iron Oxide NPs	Enhanced MRI Contrast
	Endorem, Lumirem, Sinerem [79,106]	Guebert	Approved / Investigational	Iron Oxide NPs	Enhanced MRI Contrast
In Vitro Imaging	FeraSpin [107]	Miltenyi Biotec	Research Use Only	Iron Oxide NPs	Enhanced MRI Contrast
	Clariscan [79]	Nycomed	Phase III	Iron Oxide NPs	Enhanced MRI Contrast
	Resovist [79,106] Supravist [80]	Schering	Approved (2001)Phase III	Iron Oxide NPs	Enhanced MRI Contrast
	Qdot Nanocrystals [108]	Invitrogen Corporation	Research Use Only	Quantum Dot	Fluorescent Emission
	Nanodots [109]	Nanoco Group PLC	Research Use Only	Quantum Dot	Fluorescent Emission
	TriLite™ Nanocrystals [110]	Crystalplex Corporation	Research Use Only	Quantum Dot	Fluorescent Emission
In Vitro Cell Separation	eFluor Nanocrystals [111]	eBiosciences	Research Use Only	Quantum Dot	Fluorescent Emission
	NanoHC [112]	DiagNano	Investigational (Research Only)	Quantum Dot	Fluorescent Emission
	CellSearch® EpithelialCell Kit [99]	Veridex, LLC (Johnson & Johnson)	Approved (2004)	Iron Oxide NPs	Magnetic Separation
	NanoDX [113]	T2 Biosystems	Research Use Only	Iron Oxide NPs	Magnetic Separation

Table 1.4 Confirmed and likely nanomedicine products which show active behavior beyond active targeting.²⁵

In this case, most of the products are iron oxide nanoparticles: they are used as MRI contrast agents or in magnetothermia therapy which consists on killing targeted cells using heat that FeO_xNPs generates when stimulated under an appropriate alternated magnetic field. Also gold nanoparticles exhibit this behavior when irradiated with an appropriate laser light. Surprisingly no drug-loaded nanoparticles are present in the list, meaning that there is much work to do under this aspect.

Concluding, we can resume some relevant aspect of nanomedicine in the following points:

- Most of nanomedicine products (currently approved or likely) are hard or soft nanoparticles
- Most of the investigational nanomedicine therapeutics products are intended to be used in cancer treatment
- Devices products are mostly designed to be used in in vitro testing or in vivo imaging
- Passive targeting currently is the preferred targeting mechanism although active targeting is more specific and desirable

- Nanoparticles (in particular those made of iron oxides or gold) are commercialized and used as cancer hyperthermal treatment agents.

Cancer nanotechnology

Cancer is a major cause of mortality: only in US over 1.500.000 new cases are estimated in 2016 with almost 600.000 deaths.²⁶ With these numbers it's no wonder why nanomedicine is mostly centering on cancer diagnosis and treatment. It is a highly complex disease which initially is localized but can spread in distant sites within the body becoming difficult to cure. Current diagnostics tools consists on radiology or histopathological examinations while most common treatments consists on chemotherapy, radiotherapy and, when possible, surgical removal.²⁷ There are several drawbacks in using these therapies like non-specific distribution of drugs which lead to inadequate dose delivery to tumor site, high cytotoxicity, difficulties in monitoring therapeutic responses and possibility of the development of drug resistancy.²⁸ However, as any other cancer therapy, the aim of cancer nanotechnology is to achieve the optimal drug concentration in tumor site in order to destroy cancer cells while leaving unaltered healthy cells or tissues. To overcome these problems several ligand-targeted therapeutic strategies have been developed like immunotoxins, radioimmunotherapeutics and drug immunoconjugates²⁸ but limitations in their delivery are still a problem.

Nanosystems have four characteristics that distinguish them from other cancer therapeutics:

1. They can themselves have a therapeutic or diagnostic function and can eventually carry a huge therapeutic payload.
2. Nanosystems can be functionalized with targeting ligands (i.e. antibodies) ensuring high affinity and specificity for target cells.
3. Can be designed to accommodate multiple drug molecules enabling combinatorial cancer therapy.
4. Can bypass drug resistance mechanism and immunity defense.

Categories of nanosystems used in cancer nanotechnology with their principal uses are listed in table 1.5 and, as said before, they can act both with active or passive mechanism.

Categories	Structure	Uses	References
Liposomes	Prospolipidic vesicles	Drug delivery	29
Nanoparticles	Metallic (Au, FeO _x etc.). Different shapes and dimensions.	<ul style="list-style-type: none"> • Drug delivery • Imaging • Contrast agents • Hyperthermal treatment • Radiotherapy • Combined techniques • Diagnosis/Assay 	14,17,20,25,28,30-32
Polymeric micelles	Micelles of amphiphilic surfactant molecules	Drug delivery	33,34
Dendrimers	Macromolecular compounds with branches around an inner core	<ul style="list-style-type: none"> • Drug delivery • Imaging • Contrast agents 	35
Nanocantilevers / Nanopillars	Micro/nano array made of different materials	Biomarker detection	36
Carbon nanotubes	Single or multi walled carbon nanotubes	<ul style="list-style-type: none"> • Biomarker detection • Imaging • Hyperthermal treatment 	37
Quantum dots	PbS, PbSe, CdSe, CdS, InS, InP (semiconductor nanoparticles)	<ul style="list-style-type: none"> • Biolabels • Imaging 	38

Table 1.5 Categories of nanotechnologic materials with their principal uses in cancer research (adapted from reference²⁸).

Metallic nanoparticles seem to be promising tools in cancer treatment and diagnosis. This is due to their interesting chemical and physical properties which make them a very versatile tool. In particular, future directions of cancer nanotechnology are the development of theranostic nanosystems which, by definition, are able to simultaneously provide diagnosis and treatment of cancer. Gold and iron oxide nanoparticles possess very peculiar properties that make them a perfect theranostic tool either as separated entities or in a unique composite system.

Gold nanoparticles in cancer research

Gold nanoparticles possess very unique features that can't be found in other metallic nanoparticles. First of all gold is known to be an almost chemically inert material and

for this reason is considered a biocompatible metal (either in bulk or nanoparticle form). Biologically speaking his biocompatibility derives from the fact that pure AuNPs does not release ions in solution which can bind to proteins or other biological entities thus affecting their function. This happen, for example, with silver nanoparticles: Ag ions can form complexes with biomolecules thus resulting in a toxic effect. For this reason AgNPs are commonly used as antimicrobial agents.³⁹ In addition gold hardly oxidize, thus meaning a practically inexistent reactivity in biological water-based environments.^{40,41}

Functionalization of the surface of gold nanoparticles is possible exploiting their affinity for sulphur or nitrogen. Molecules (polymers, drugs, dyes etc.) possessing thiols or amine groups are the most used to labels the surface of AuNP. In the same way bioconjugation with antibodies, DNA fragments, peptides etc. can be performed giving AuNP active targeting properties.¹⁴

Optical properties of gold nanoparticles are used in cancer research for the development of imaging and diagnosis techniques. There are two ways to perform imaging or diagnosis using gold nanoparticles. The first consists in exploiting Surface Enhanced Raman Scattering (SERS), which consists on the enhancement of the Raman signal of a reporter molecule when it's close to the surface of a gold nanoparticle. In this way, using a micro-Raman equipment, it is possible to track gold nanoparticles in cells or tissues. This technique is very sensitive (only few molecules on AuNP surface are necessary to obtain a clear signal) and allows multiplexed mode analysis, but is limited by the depth penetration of the laser used.^{31,42,43} The second way consists in labelling AuNP with fluorescent probes sufficiently distant from their surface (usually using a spacer molecule between the surface and the fluorescent probe) to avoid SERS effect and subsequent fluorescent quenching. Imaging is performed using a fluorescence microscope and is usually useful to track gold nanoparticles on tissues or cells. Clearly this technique is faster than SERS, at the present moment, but usually is very less sensitive and greater numbers of particle are needed to be visible.⁴⁴

Finally gold nanoparticles can also show active behavior beyond active targeting, becoming a complete theranostic tool. In this case there are three ways to perform cancer treatment using gold nanoparticles. First, gold nanoparticles can be loaded with drugs, which had to be released when the tumor site is reached. Assuming an efficient and selective targeting, the control of the release mechanism is a key issue.

Valid solutions consist in a release triggered by an external stimulus like a temperature change or pH variations. In this case AuNP are functionalized with polymers which change their conformation when a certain temperature or pH condition is reached. Before reaching the opportune condition the drug is entrapped in the polymeric matrix, but when conformation change the drug is released. pH responsive systems usually take advantage of the slightly acidic environment of tumor cells while temperature responsive systems are triggered using an external laser source which heat the nanoparticles.^{22,45,46} A second strategy consists in radiotherapy enhanced by gold nanoparticles: loading high Z materials into the tumor could result in greater photoelectric absorption within the tumor than in surrounding tissues, and thereby the dose delivered to a tumor during radiation therapy is enhanced.²⁸

The third method for tumor treatment which does not include the use of drug is plasmonic photothermal therapy (PPT). When gold nanoparticles are irradiated with an appropriated laser sources, the light absorbed is converted into heat. Locally, the temperature that can be reached is sufficient to provoke cancer cell death. Usually, near infrared or infrared laser sources are preferred because their penetration depth is higher than visible lasers.⁴⁴

In this thesis gold nanoparticles will be used, in combination with iron oxide nanoparticles, for imaging technique, using the SERS effect, of cancer cells and then for treating cancer cells with PPT technique.

Iron oxide nanoparticles in cancer research

Iron oxide nanoparticles (FeO_xNPs) are of particular interest in the field of nanomedicine and cancer research thanks to their magnetic properties.^{16,47} These nanoparticles are, most of the time, composed of magnetite (Fe_3O_4) but sometimes, depending on the synthesis, other iron oxides are found like maghemite ($\gamma\text{-Fe}_2\text{O}_3$) or both maghemite and magnetite. For this reason one usually refers to iron oxide nanoparticles as a general way to indicate these types of nanoparticles instead of specify the iron phase.

Like gold nanoparticles, FeO_xNPs show very low toxicity and this also encourages biomedical use of these NP. Functionalization of the surface is performed exploiting iron oxides affinity for molecules possessing carboxylates or phosphates groups. It's also a common practice to cover iron oxide nanoparticles with a silica shell to

provide new functionalities or properties or simply to have different functional groups on the surface to perform other reactions. This is usually realized with a sol-gel synthesis (Stöber synthesis).⁴⁷

FeO_xNPs have four main uses in biomedical and cancer research: magnetic resonance imaging (MRI) contrast agents, in vitro bioseparation (immunomagnetic sorting), drug delivery and hyperthermia.^{47,48}

In MRI, the effect of relaxation times of iron nuclei on water protons is used to perform imaging of cells and tissues. Currently, several iron oxide nanoparticles formulations have been approved by Food and Drug Administration like Feridex, Endorem and Resovist.²⁵ The use of FeO_xNPs as MRI contrast agents instead of common gadolinium chelated complexes permits to overcome potential toxicity of these complexes.

FDA approved MRI contrast agents like Endorem consists in non-targeting (without antibodies) superparamagnetic iron oxide nanoparticles which accumulate in normal lymph tissue after injection at tumor site. Since no accumulation takes place in metastatic nodes, lymphatic staging can be performed using MRI.⁴⁹

Future direction of FeO_xNPs as MRI contrast agents involves the use of targeted nanoparticles so that they can specifically label tumor tissues or cells.⁴⁸

Another application of iron oxide nanoparticles in MRI is specific cell tracking. This consist in loading cells with a sufficient quantity of FeO_xNPs (micromolar Fe concentration) and then track these cells in vivo by MRI. If a cell is sufficiently loaded with iron oxide nanoparticles MRI can provide cell tracking with a resolution approaching the size of a cell.⁴⁷

The second relevant application, which is important also for this project, is bioseparation. This consists in exploiting magnetic properties of FeO_xNPs for an in vitro separation/purification of proteins or cells from other biological entities. In this case usually nanoparticles are functionalized with specific antibodies and the entire process is called immunoseparation or immunosorting. Bioseparation have several advantages in comparison with traditional separation procedures. For example all passages take place in one test tube, avoiding long and expensive chromatographic purifications. Another advantage of immunosorting is the possibility to concentrate biological samples in smaller volume. This is useful in rare cell separation, when cells that have to be detected are rare like in circulating tumor cells (CTC) detection.^{47,48,50-53}

Regarding drug delivery, iron oxide nanoparticles utilizes the same release strategies as gold nanoparticles (temperature or pH release trigger) but the difference is that FeO_xNPs accumulation to delivery site can be performed using external magnets.^{47,48} Lastly, iron oxide nanoparticles can be used for therapeutic purposes in hyperthermia treatment. This time hyperthermia is not provoked by an adsorption of light, like in gold nanoparticles, but from the absorption of the energy of an oscillating magnetic field and conversion into heat. Heating is most due to relaxation process and hysteresis losses that transform energy into heat. Treatment is performed injecting iron oxide nanoparticles directly to tumor site and then thermoablation is performed using a RF emitter implanted in the interested area. Less intrusive method consists on irradiating the pathological area with an array of external microwave emitters.^{47,48,54} In this thesis project iron oxide nanoparticles will be used for cell guiding and immunosorting of specific cancer cells in combination with AuNP, thus exploiting their capacity of migrate in solution if exposed to a magnetic field gradient.

Magneto-plasmonic nanoparticles in cancer research

Magneto-plasmonic nanoparticles, as the name suggests, combine the magnetic properties of iron oxide nanoparticles with optical-plasmonic properties of gold nanoparticles. Magneto-plasmonic materials are not necessarily made only of gold and iron oxide. Other common studied materials are, for example, a combination of Ag (for plasmonics) and Co (for magnetics) substituting gold and iron oxide respectively.^{55,56}

However, gold and iron oxide nanoparticles are the most attractive magneto-plasmonic materials for nanomedicine applications because of their biocompatibility and versatility, as recalled above.

Combination of gold and iron oxide in a unique nanomaterial gives birth to a powerful tool for cancer research which makes possible to perform simultaneously diagnostic, imaging and treatment using combined techniques previously developed for the individual gold or iron oxide nanoparticles.

The synthesis of these kinds of nanoparticles is rather complex and different morphologies or structures can be obtained (see “Common synthesis for magneto-plasmonic materials” at pag 59). Also for this reason, currently, no commercial products with these characteristics are available, but they are one of the major focuses in nanomedicine because of the great potential of this type of nanostructures.

For example Urries et al. synthesized 100-200 nm diameter hollow and partially hollow nanoparticles with a magnetic core and gold shell which potentially can be used as theranostic agents.⁵⁷ These nanoparticles proved to be useful as MRI contrast agents thanks to magnetite core and for NIR hyperthermia tool thanks to the gold shell. Furthermore, the cavity is capable to hosts small molecules like drugs for drug delivery options.

Recently, from the group in which I developed this thesis it was reported the synthesis of gold and iron alloy nanoparticles (AuFeNPs) and their use as multimodal MRI-SERS and computed x-ray tomography (CT) imaging tool.⁵⁸ These alloy nanoparticles showed good applicability in in vivo experiments and also an almost absent cytotoxicity.

Bao et al synthesized hybrid iron oxide@gold core-shell nanoparticles for magnetic protein separation and purification. In this case gold surface is needed to take advantage of the easy functionalization with thiolated molecules.⁵⁹

Antibody functionalized Fe₂O₃@Au core-shell nanoparticles have been used for immunoseparation of antigens in solution with subsequent quantitative determination using a SERS assay.⁶⁰ This time a free external gold surface served for SERS effect and as functionalization site.

Since both gold and iron oxide nanoparticles can be utilized separately for photothermal and magnetothermal therapy, when they're combined in a unique nanosystem the two techniques can be performed simultaneously. A very interesting example is found in a work of Espinosa and coworkers.⁶¹ They synthesized aggregates composed of a core with multiple iron oxide nanoparticles covered with a gold shell. After injection in an implanted tumor (mice) aggregates were stimulated simultaneously with an alternated magnetic field (110 kHz, 25 mT) and laser light (680 nm, 0.3 W cm⁻²) showing a doubled performance with respect to the two separated techniques.

Other many valid examples of magneto-plasmonic nanoparticles for detection or treatment of cancer or pathogens are present in literature⁶²⁻⁶⁷, but only in few cases biologically active (antibody-labeled) magneto-plasmonic nanosystems were obtained.⁶⁸⁻⁷¹ Furthermore, quantitative determination of the targeting activity of these systems is still absent or incomplete and more work is to be done before they reach the necessary quality for clinical trials.

Infographic in figure 1.5 provides a schematic summary of gold and iron oxide nanoparticles properties and applications of interest in cancer research.

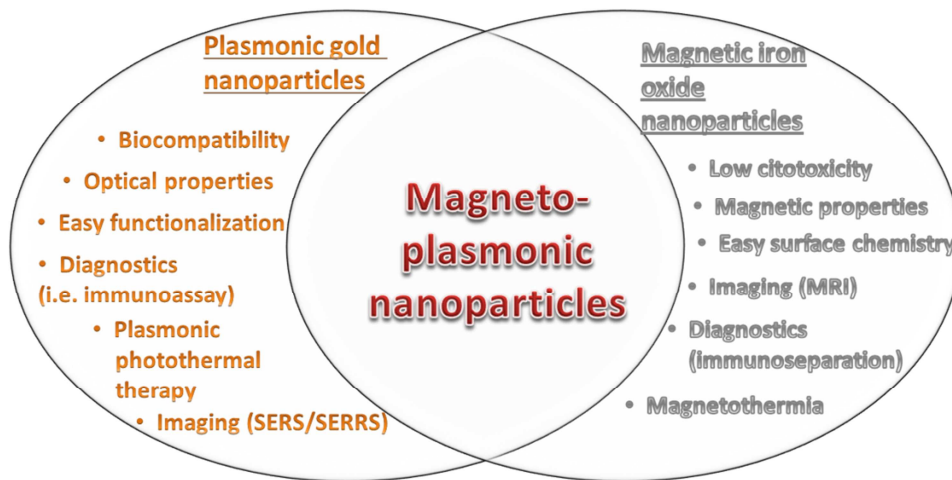


Figure 1.5. Infographic with properties and applications of interest in nanomedicine of gold and iron oxide nanoparticles.

Magneto-plasmonic nanosystems made of gold and iron oxide nanoparticles are the object of this thesis, in particular their application in cell guiding, immunoseparation/imaging and photothermal treatment.

Cancer: principal characteristics

Cancer is characterized by an irregular growth of cells and the possibility of a diffusion of the same in other regions of the body.⁷² Tumor is a mass of cells, a visible expression of a formation process of neoplastic tissues that may have developed for years.⁷³ It is thought that cancer development is due to random succession of genetic mutations of DNA of cells that proliferate for many cycles and long periods.

Unlike healthy cells, tumor cells show an abnormal proliferation due to a lack in self-regulatory intracellular mechanisms and, frequently, also an abnormal angiogenesis affects involved tissues. Another important characteristic connected to tumors is the presence of so-called markers or biomarkers. These are substances, usually proteins, that can be found on blood or other corporal fluids and demonstrate the presence of the disease. Some of these markers have a concentration which is proportional to tumor mass and for this reason their monitoring is useful for diagnosis or to follow the progress of ongoing therapy.⁷²

Cancer is diagnosed when the involved tissue is sufficiently diversified from surrounding cells. However there isn't a unique diagnostic method and usually histological analysis is firstly performed, also with contrast agents that help recognition and detection of specific tumor cells (imaging techniques).

On the contrary, benign tumors usually are similar to original tissues. They can develop and grow in any environment, but they are not invasive and keep separate from circumstantial tissues because of a connective tissue capsule that cover them. However problems can emerge when they become large enough to generate pressure in neighboring organs.

On the other side, malignant tumor have two distinctive characteristics: cell abnormalities if compared to neighboring cells and the invasion of surrounding tissues. This last is the definitive proof when observing a malignant tumor in fact, in contrast with benign tumors, they're not surrounded by a connective tissue capsule and they grow in a cluttered and disorganized way. Because of this, tumor cells can penetrate the lymphatic or circulatory system thus leading to the formation of tumoral mass in other parts of the body: the so-called metastasis.⁷³

Antibodies: structure and functions

Antibodies (Ab), also called immunoglobulins (Ig), are glycoproteins with the function of localizing antigens and trigger a response from the immune system. They are synthesized by lymphocyte T cells and can either be expressed on cell surface or released in soluble form in the organism.

Soluble antibodies act as immune system mediators binding to external antigens and triggering the immune system response.

Thanks to their unique synthesis, immune system can, in theory, produce specific antibodies for every antigen.

This feature makes antibodies a very interesting experimental, diagnostic and therapeutic tool.

Antibodies have typical "Y" shape and are formed by four polypeptide chains equal two by two: two heavy chains and two light chains (Figure 1.6).

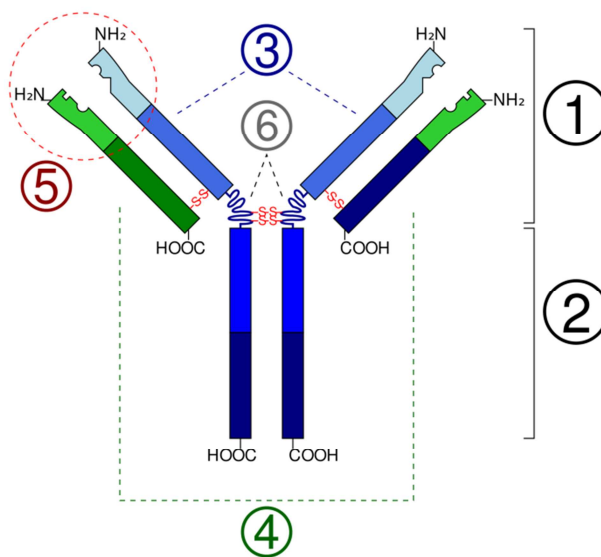


Figure 1.6 1. Fab region 2. Fc region 3. Heavy chain (blue) with one variable (V_H) domain followed by a constant domain (C_{H1}), a hinge region, and two more constant (C_{H2} and C_{H3}) domains. 4. Light chain (green) with one variable (V_L) and one constant (C_L) domain 5. Complementarity determining region (CDR), antigen binding site (paratope) 6. Hinge regions.⁷⁴

The four polypeptide chains are bonded together through disulfide bridges.

Light chains are formed by one variable (V_L) and one constant (C_L) domain while heavy chains are formed by a variable domain (V_H), a hinge region and one or more constant domains (C_{H1}, C_{H2}, C_{H3}...).

Fragment antigen-binding (Fab) region is the most important site of the antibody because it's responsible of antigen recognition and binding. It is composed of one constant and one variable domain from each heavy and light chain of the antibody. Every variable region of heavy and light chain contains three ipervariable regions or CDR (Complementarity determining regions). CDR portions determine the specificity to an antigen and most contributes to the bonding.

The base of the Y with the rest of the two heavy chains is called Fragment crystallizable (Fc) and play a role in modulating immune cell activity. This region is responsible for the appropriate immune response to a given antigen, this by binding to specific receptors or complement proteins.

There are two classes of antibody if referring to the production methods.

Polyclonal antibodies (pAb) are produced by a population of different lymphocyte clones treated with the same antigen. Monoclonal antibodies (mAb) are obtained

from a population of the same lymphocyte clones so they will have the same specificity against one antigen.⁷⁵

Immune responses to tumors

It's a common opinion that immunity strengthening against tumors could be a promising approach to cancer therapy.

One of the physiological functions of acquired immunity is the prevention of transformed cell growth and their destruction before they can generate a tumor mass. This phenomenon is called immune surveillance.

Many experimental data corroborate the hypothesis that immune surveillance plays an important role in preventing tumor growth; however the fact that tumors develop also in perfectly healthy subjects from the immune point of view suggests that anti-tumor response is quite weak, and easily overtaken by fast-growing tumors.

As recalled above, malignancies express different types of molecules (biomarkers) that can be recognized as extraneous molecules by the immune system. If the immune system responds to a tumor, evidently, it expresses antigens that are recognized as non-self (extraneous).

In experimental tumors, induced by carcinogenic chemical substances or radiations, antigens consist of mutant forms of normal protein cells.

On the other hand, in many spontaneous human malignancies antigens that provoke an immune response seem to be perfectly normal proteins. The difference is that they are overexpressed or their expression, which is usually limited to particular tissues or stages of development, is deregulated.

Although an immune response for self-normal antigens is not normally expected, their aberrant expression is sufficient to activate immune system.

The principal mechanism by which the immune system acts against tumors is the killing of neoplastic cells by cytotoxic lymphocyte T cells (CTL) specific for tumoral antigens. Most of the time immune response can't compete with such a fast neoplastic growth, also because a malignancy develops particular mechanisms to overcome immune response. For example, some neoplastic cells lose the expression of target antigens of the immune response: if such antigens are not essential for the maintenance of neoplastic phenotype, the tumor continues to grow and spread.

Therapy for spread tumors, that can't be surgically removed, is actually based on chemotherapy and radiotherapy with well-known side effects on healthy tissues.

Since immune response is highly specific, a cure based on anti-tumor immunity which can be extremely selective against unhealthy tissues has long been hoped.

In many cancer forms tumor antigen-specific monoclonal antibodies have been tested, usually conjugated with powerful toxins; these antibodies bind to target cells activating host's immune system or delivering toxins to neoplastic cells.

Patient's therapeutic treatment with immunological techniques is called immunotherapy.

Many innovative immunotherapy strategies are based on stimulating patient's immune response against neoplastic cells, for example through vaccinating with cells of its own tumor or with antigens derived from them.

Another technique is called "adoptive cellular immunotherapy" and is performed by inoculating tumor-specific lymphocytes on patient.⁷⁵

As we have seen, antibodies are of crucial interest in cancer research due to their high specificity against antigens which are overexpressed by tumor cells. Nanomedicine takes advantage of this specificity by functionalizing antibodies on nanosystems so they become smart structures. Some examples of antibody functionalized nanosystems were provided in previous subchapter. In this thesis antibody functionalized magneto-plasmonic nanostructures will be synthesized and characterized with particular regard to antibody functionality. It will be shown how selective can be a nanostructure when it is engineered with an antibody.

Prostate cancer

In the last decade, prostate cancer has become the most frequent tumor in the male population of occidental countries. At the basis of this phenomenon, beyond the presence of risk factors, there is the greater probability of diagnosing this disease, which is present in a latent form in 15-30% of individuals over 50 years old and in about 70% of octogenarians.⁷⁶

Prostate cancer is one of the fifth most common cancers: in Europe in 2012 had an incidence of 22.8% with a mortality of 9.5% which make it the third for mortality after lung and colorectal cancer (Figure 1.7).⁷⁷

Actual screening methods consist in the detection of PSA (Prostate Specific Antigen) antigen on blood or in digital rectal exam. However diagnosis is confirmed only after a biopsy of prostatic tissue.

Other antigens, beyond PSA, that are overexpressed by prostatic cancer cells are PSCA (Prostate Stem Cell Antigen) and PSMA (Prostate Specific Membrane Antigen). These antigens can be recognized by specific antibodies. In this thesis we will use the antibodies specific for PSMA antigen, which is called D2B. This antibody, functionalized onto our nanostructure, will help recognizing cells that express PSMA antigen (indicated as PSMA+ cells).

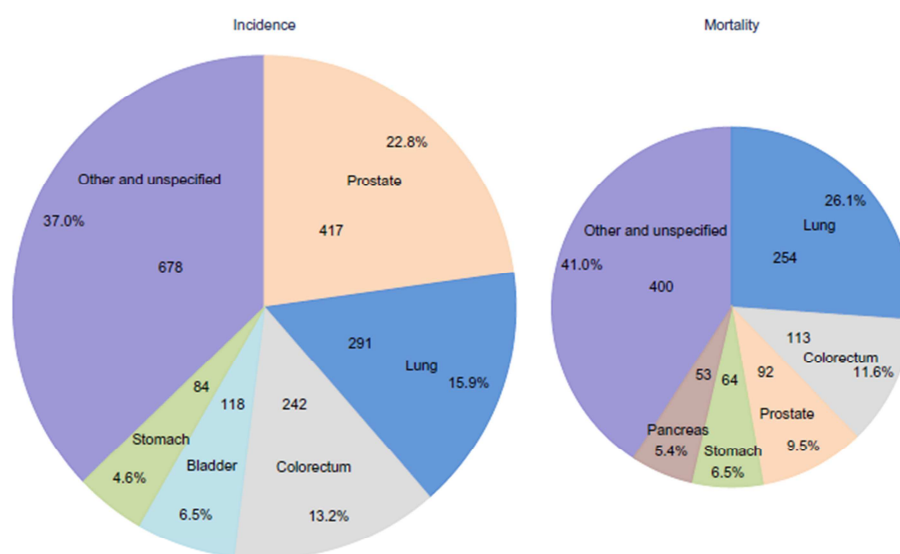


Figure 1.7 Distribution of the expected cases and deaths for the 5 most common cancers in Europe 2012 in males. The area of the segment of the pie chart reflects the proportion of the total number of cases or deaths.⁷⁷

Synthesis of nanoparticles: top-down and bottom-up methods

Several synthesis strategies are available to synthesize nanoparticles of different composition and morphology, but in a very general way there are two approaches: top down and bottom up (Figure 1.8).

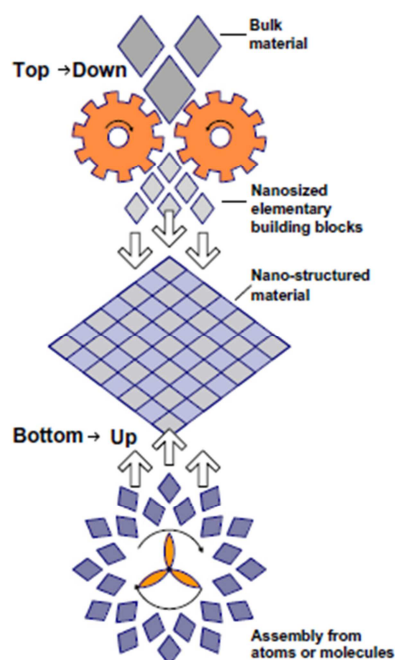


Figure 1.8 Artistic representation of top-down and bottom-up approaches.⁷⁸

A top-down method, called also physical method, consists in a reduction of dimension of bulk material until it reaches desired nano dimensions. This is made through mechanical and/or physical processes which removes or divides bulk material. Some examples are ball milling, lithography, machining, radiolysis, sonolysis, thermolysis, photochemistry and laser ablation. These methods are usually less used than bottom up methods because in some cases they require dedicated or quite expensive instrumentation. Furthermore, if not well optimized, size and morphology of nanoparticles are difficult to control, like in ball milling process. Less use of chemicals is a characteristic of these methods. In this thesis a top-down method to synthesize both gold and iron oxide nanoparticles will be used: Laser Ablation Synthesis in Solution (LASiS), for which a special section is provided at the end of the introduction.⁷⁹

On the other side, bottom-up methods starts from molecules, atoms or even small nanoparticles to build more complex nanoparticles of the desired size and morphology. In this case the most common strategy consists in the controlled reduction of metal ions in solution. Controlling the nucleation and growth processes with the use of stabilizing agents, one obtains nanoparticles of the desired size and morphology. Other conditions, which affect these syntheses are temperature, time, pH, the choice of the reductant, solvents, the metal ion compound, the use of

emulsions or micelles and clearly the proportions between reagents. Since many parameters are involved in bottom-up methods, there are plenty of methodologies to synthesize the same type of nanoparticle. Usually with these strategies one can obtain nanoparticles of the desired morphology and with a narrow size distribution simply choosing the right synthesis and opportunely varying reagents proportions. However, some drawbacks regarding the use of chemicals or stabilizers which could be potentially toxic cannot be underestimated, especially when such nanoparticle are synthesized for biomedical purposes. Besides metal ion reduction, other processes are frequently used like vapor phase deposition (VPD), physical vapor deposition (PVD) and chemical vapor deposition (CVD).

As said above, there are many bottom-up strategies for the synthesis of the same type of nanoparticles. The most common for gold and iron oxide nanoparticles will be briefly described in dedicated paragraphs and one of them will be utilized in trying to create a continuous gold layer in the nanostructures discussed in this thesis.

In this thesis another bottom-up method, which is part of a class of reactions called sol-gel, is used to synthesize a silica shell around iron oxide nanoparticles. Sol-gel methods are quite different with respect to more common salt reduction synthesis. They involve a set of chemical reactions which irreversibly convert a homogeneous solution of a molecular reactant precursor (sol) into a very large molecular weight three-dimensional polymer (gel) forming an elastic solid filling the same volume as the solution. Typically this involves a hydrolysis reaction followed by condensation polymerization. In nanoparticles synthesis, sol-gel methods are commonly used to obtain silica nanoparticles or hybrid metal-silica nanostructures. The process of formation of silica nanoparticles by sol-gel method passes through the same process steps as reduction methods, that is nucleation and growth, and have to be stopped when desired NP size is reached, before a continuous polymer is formed (usually separating formed NP from reagent mixtures). The Sol-gel method used in this thesis is described in section Iron oxide nanoparticles – A sol-gel approach to surface modification.⁷⁹

Gold nanoparticles

We have seen that gold nanoparticles are crucial tools in nanomedicine and due to their properties are fundamental also for other research topics (catalysis,

electrochemistry, supramolecular chemistry, non-linear optics etc.). The size and morphology of nanoparticles can vary considerably their properties and, as a consequence, also the field of application can vary. For this reason several synthesis strategies are available for AuNPs, mainly emerged in 20th century, through which one can obtain gold nanoparticles of the desired size. Below, one can find most employed bottom-up and top-down syntheses for AuNPs, followed by explanation of chemical and optical properties useful for the work in this thesis.

Synthesis strategies

Citrate reduction

Among all synthesis methods this is the most used and consists in the formation of AuNPs of ca. 20 nm reducing Au(III) ions from chloroauric acid (HAuCl₄) with trisodium citrate in water. This is also called Turkevitch method which was introduced in 1951. Modifications were introduced by Frens in 1973: in its studies he obtained gold nanoparticles with sizes from 16 nm to 147 nm varying the proportions between gold and citrate (or other stabilizers). In these nanoparticles citrate is also a stabilizer (unless other stabilizers are used) and for this reason they show a negative surface charge due to deprotonated carboxylic groups of citrate. Although there is a good size control using this method, presence of citrate can influence subsequent surface functionalization since ligand-exchange reactions are involved. Lastly several washing steps are required to eliminate the presence of citrate residues which can interfere with in vivo or in vitro biological experiments.¹⁴

Brust-Schiffrin method

Published in 1994 this method allows to obtain nanoparticles from 1.5 to 5.2 nm with a narrow distribution. Another peculiar characteristic is that as synthesized AuNPs can be dried and redissolved in common organic solvents without incurring in irreversible aggregation.

The synthesis takes place in a two-phase systems and use alkanethiols as stabilizers. AuCl₄⁻ is transferred in toluene using tetraoctylammonium bromide as phase-transfer reagent and reduced using NaBH₄. Varying the proportions between gold and ligands different sizes are obtained. In particular the increasing of ligand concentrations reduces the size of synthesized nanoparticles.¹⁴

Seeding-growth method

This is a very popular method which consists in performing a classical Au (III) reduction from HAuCl_4 in a solution containing pre-existent gold nanoparticles called seeds. Common reductants can be used in this method like citrate, NaBH_4 , formaldehyde or hydroxylamine hydrochloride. In this synthesis, Au ions reduce on seeds surface, increasing their dimension. AuNPs in range between 5-40 nm are obtained by varying seed-metal ion ratio. Gold nanorods can be synthesized using seeding-growth method.¹⁴

Others reduction methods

Perrault method uses hydroquinone to reduce gold ions in a solution containing gold seeds. Nanoparticles between 30-300 nm can be obtained. Citrate or other stabilizers are needed in this synthesis.⁸⁰

Martin method is another reducing method which is interesting because allow to obtain naked gold nanoparticles in water. With the precise control of NaBH_4 -NaOH to HAuCl_4 -HCl ratio one obtains AuNPs between 3-6 nm. These nanoparticles are stable in water thanks to charge stabilization, but should be usually purified from NaBH_4 residues.⁸¹

Navarro method implies the use of sodium acetylacetonate for the reduction of Au(III) to Au(I) immediately followed by addition of citrate for reduction of Au(I) to Au (0). Sodium acetylacetonate impacts on nuclei number and induce a size evolution of the core up to 90 nm with a narrow distribution.⁸²

Concluding, others significant methods involves the use of micelles or microemulsions. Technically speaking these are two-phase methods in which surfactants forms micelles or microemulsions creating a favorable microenvironment for the reduction of metallic ions. Au ions are extracted from aqueous to an organic phase or viceversa depending if normal or reversal micelles are used. This is an advantage respect to the conventional two-phase system because controlling the micelles dimension (also in conjunction with the presence of other stabilizers) one controls AuNPs size.¹⁴

Physical methods

Physical methods differentiate from previous chemical methods because the formation of nanoparticles is not attributable to chemicals (reductants) but is provoked by physical phenomena.

For example light irradiation can be used to synthesize gold nanoparticles in solutions. In literature we find that UV irradiation can reduce HAuCl_4 in water solution in the presence of capping agents⁸³ to form stable AuNP.

Besides UV, other light sources can be used in AuNPs synthesis like NIR⁸⁴ and microwaves.⁸⁵

Sonochemical methods make use of an ultrasonic field to reduce gold ions and form AuNPs.⁸⁶ In this case parameters to be considered are the temperature of the solution, the ultrasound frequency and intensity and the positioning of the reactor. Sonolysis was also used to deposit gold nanoparticles on silica spheres.⁸⁷

Radiolysis and thermolysis are also alternative physical methods for the preparation of gold nanoparticles: the first use γ -irradiation to synthesize or control the size of AuNPs while the second use high temperature to increase size of gold cluster or nanoparticles.¹⁴

Laser ablation synthesis in solution is also part of this category and implies the use of pulsed laser source to synthesize gold nanoparticles.

Although physical methods are less used with respect to chemical methods they have an unquestionable advantage that is the absence, in the synthetic route, of reductants thus making the entire process more clean and green.

Localized surface plasmon resonance (LSPR)

Gold nanoparticles possess very different characteristics with respect to bulk gold which are mainly due to their nanometric size. The most important is the localized surface plasmon resonance (LSPR), which is responsible for the ruby red color of 15-20 nm AuNP in solution. The origin of the phenomenon is the coherent oscillations of the conduction band electrons induced by an interacting electromagnetic field. Small enough (15-20 nm) gold nanoparticles strongly absorb 520 nm green light, meaning that this photon frequency is in resonance with collective oscillation of conduction band electrons which is called localized surface plasmon resonance. The term “localized” is used when surface plasmons are confined to metallic nanoparticles or nanostructures.

Figure 1.9 represents the LSPR behavior in metallic nanoparticles.

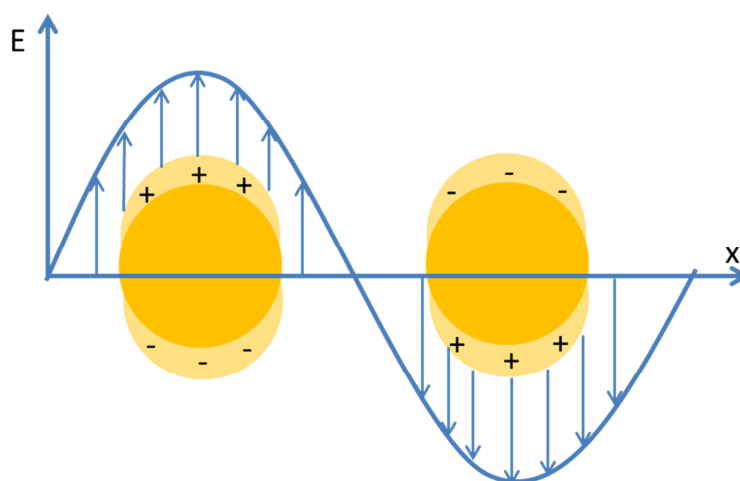


Figure 1.9 In gold nanoparticles, the coherent oscillation of conduction band electrons induced by an interacting electromagnetic field is called localized surface plasmon resonance (LSPR).

When the electric field of an incoming light interacts with a plasmonic nanoparticle it induces a polarization of the free conduction electrons. Positive charges are assumed to be immobile while negative charges (electrons) moves under the influence of the electric field. This movement creates a net charge difference at nanoparticle boundaries which, in turn, gives rise to a linear restoring force. The result is the creation of a dipolar oscillation of electron called surface plasmon oscillation.⁸⁸

For many metals like Pb, In, Hg, Sn, Cd, LSPR lies in the UV region so nanoparticles of these metals doesn't appear colored. But for coinage metals (Au, Ag, Cu) the situation is different and thanks to d-d transitions they have an LSPR in the visible spectrum.^{14,88}

Gustav Mie in 1908 was the first to rationalize the observed red color of gold nanoparticles in water. His theory starts with two assumptions: (i) the particle and the surrounding medium are considered homogeneous and describable by their bulk optical dielectric functions and (ii) particle diameter is much smaller than the incident wavelength ($2R \ll \lambda$ where R is nanoparticle radius and λ the incident wavelength). The last assumption allows considering the electric field constant all along the nanoparticle so the interaction can be considered electrostatic rather than electrodynamic (also called quasi-static approximation).

The solving of Maxwell's equations lead to an expression of extinction cross section σ_{ext} ($\sigma_{\text{ext}} = \sigma_{\text{abs}} + \sigma_{\text{sca}}$ = absorption cross-section + scattering cross-section) for metallic nanoparticles (equation 1.1):

$$\sigma_{\text{ext}}(\omega) = 9 \frac{\omega}{c} \varepsilon_m^{3/2} V \frac{\varepsilon_2(\omega)}{[\varepsilon_1(\omega) + 2\varepsilon_m]^2 + [\varepsilon_2(\omega)]^2}$$

Equation 1.1

where ω is the angular frequency of the exciting light, c is the speed of light, $V=4/3\pi r^3$ is the volume of the spherical particle, ε_m and $\varepsilon(\omega) = \varepsilon_1(\omega) + i\varepsilon_2(\omega)$ are the dielectric functions of the surrounding medium and of the material (real and imaginary part).⁸⁹

When the term at the denominator reaches its minimum, extinction cross-section reaches its maximum, in correspondence of the maximum of the surface plasmon band. Looking at the dielectric function of metals, one finds that this happens when $\varepsilon_1(\omega) \approx -2\varepsilon_m$; in this condition the local electric field of the particle is enhanced.

From Mie theory one can understand the relevance of the material and, clearly, of the solvent in determining the position of the surface plasmon band, since diverse materials and solvents possess different dielectric functions.

LSPR not only depends on material and solvent, but it can considerably change depending on nanoparticles size, morphology and ligands.

For larger nanoparticles (greater than ~40-50 nm for gold nanoparticles) the dipole approximation is no more valid because light can't homogeneously polarize the nanoparticle. In this case multipole forms and, as a consequence, retardation effects of the electromagnetic field across the particle can cause broadening and red-shifting of the LSPR (Figure 1.10 A). On the contrary, reducing the size of gold nanoparticles below 5 – 4 nm leads to a decrease of LSPR intensity accompanied by a slight blue shift (Figure 1.10 B). This is due to the onset of quantum size effects which become important for particles smaller than 2 nm.⁸⁸

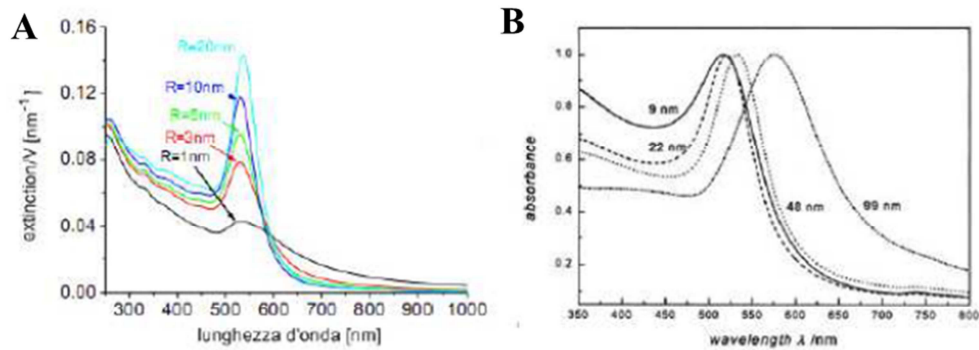


Figure 1.10 LSPR variations for gold nanoparticles with $R < 20$ nm (A) and $R > 20$ nm (B).

The morphology of nanoparticles has also a considerable effect on LSPR. In the case of nanoparticles that deviate from sphericity, Gans's modifications to Mie's theory have to be taken on account. In particular, Mie-Gans theory is valid for ellipsoidal nanoparticles: in this case the longitudinal and transverse dipole polarization does not produce equivalent resonances.

As a consequence two plasmon resonances forms and two peaks appear in the extinction spectra.

Longitudinal plasmon refer to electron oscillation along the major axis of the ellipse and shows a broadened red-shifted peak while transversal plasmon refers to electron oscillation perpendicular to long axis and shows a peak at about 520 nm like for spherical particles (Figure 1.11). This phenomenon is clearly observable in nanorods spectra, for which the distance between the two peaks is correlated with their aspect ratio.^{88,89}

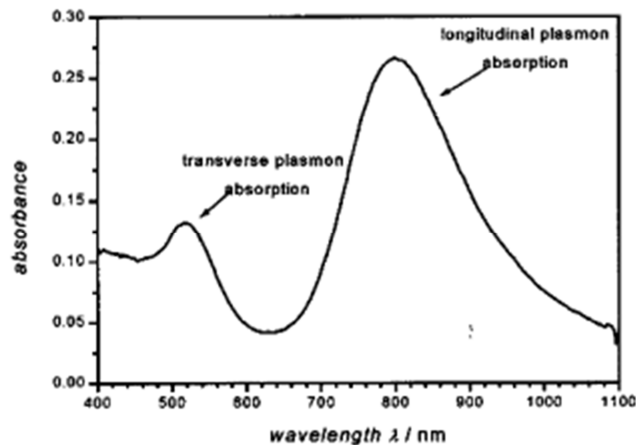


Figure 1.11 The extinction spectra of nanorods (or non-spherical particles) shows two plasmon peaks because transverse and longitudinal dipole polarization doesn't produce equivalent resonances.

Therefore, the extinction spectra of nanoparticles can provide information on the size and the morphology of AuNP. In this thesis, for example, a software developed by the group in which the work for the thesis is done, is used to fit the spectra of just synthesized AuNP to estimate their size, sphericity and concentration using Mie and Mie-Gans theory.⁹⁰

Mie-Gans theory is only applicable to non-interacting nanoparticles, which are well separated from each other.

In the case of aggregates of gold nanoparticles the plasmon oscillation drastically change because now particles are electronically coupled to each other because of dipole-dipole interactions. This leads to more complicated extinction spectra which depend on the size and shape of the formed aggregate. Aggregation causes a coupling of AuNPs plasma modes resulting in a red-shift and broadening of the longitudinal plasmon resonance. Usually extinction spectra of gold nanoparticles aggregates are a composite of conventional plasmon resonance due to single spherical particle (at about 520 nm) and a new red-shifted broadened peak due to particle-particle interactions.⁸⁹ Extinction spectra of AuNPs aggregates can also be predicted with theoretical calculations, however this issue goes beyond the aim of this thesis. A good explanation of optical properties of AuNPs aggregates is provided in the review by Gosh.⁸⁹

LSPR of noble metal nanoparticles has a relevant importance in the explanation of the surface enhanced Raman scattering (SERS) effect, which is fundamental in this work.

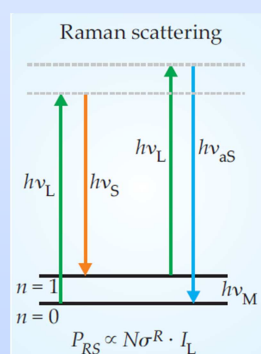
Surface Enhanced Raman Scattering (SERS)

Surface enhanced Raman scattering is a phenomenon in which amplification of the Raman signals of a molecule are observed when it's close to the surface of a noble metal nanoparticle.

In the following box the Raman effect is briefly recalled.

Raman spectroscopy

Raman spectroscopy is a vibrational spectroscopy based on the Raman effect, which was discovered in 1928 by Chandrasekhara Venkata Raman. It is based on the inelastic scattering of photons by matter. The phenomenon can be explained using a molecular energy diagram.



Depending whether the molecule is in its vibrational ground state or first excited state ($n=0, 1$), the Raman scattered photon is shifted to lower or higher energy with respect of the incident photon $h\nu_L$. Lower energy scattered photons are called Stokes scattered and have energy $h\nu_S = h\nu_L - h\nu_M$ while higher energy scattered photons are called anti-Stokes scattered and have energy $h\nu_{aS} = h\nu_L + h\nu_M$. The difference between incident and scattered photons, $h\nu_M$ is the vibrational energy of a normal mode of the molecule (Q_i). The Raman scattering power P_{RS} is proportional to the number of molecules in the probed volume, the Raman cross section of the molecule σ^R and the intensity of incident light I_L . Generally, anti-Stokes signals are weaker than Stokes because, according to Boltzmann statistics, since only a small fraction of molecules are in their excited state. From a classical point of view the incident radiation generate an oscillation of the induced dipole μ_{ind} which, in turn, depends on the molecular polarizability α and the incident electric field $E(t)$ ($\mu_{ind} = \alpha \cdot E(t)$). From this dependence derives the selection rule for Raman spectroscopy, which implies a change in polarizability for the investigated vibrational mode $\left(\frac{\delta\alpha}{\delta Q_i}\right) \neq 0$.

SERS was observed for the first time in 1974 by Martin Fleischmann, who recorded an unexpected strong Raman signal of pyridine electrochemically adsorbed on a roughed silver electrode. Lately, in 1977, Richard Van Duyne and his coworker David Jeanmarie ascertained that the observations by Fleischmann were effectively a genuine enhancement of the Raman signal. This discovery kicked off researches on SERS and its applications in several fields, which nowadays are still of actual importance.

Raman signals are weak because of the low Raman cross section which range between 10^{-30} cm^2 and 10^{-25} cm^2 with the larger value observed in resonant conditions (when the excitation wavelength matches an electronic transition). For comparison, fluorescence cross section ranges between 10^{-17} cm^2 and 10^{-16} cm^2 .^{91,92}

With surface enhanced Raman scattering, Raman signals can be enhanced by a factor from 10^4 to 10^{14} so becoming comparable with fluorescence intensity.

Three parameters have to be considered to obtain good SERS signals: the substrate, the analyte (also called SERS reporter) and the laser wavelength.

Usually, SERS substrates are nanopatterned surfaces or nanoparticles made of noble metals. The phenomenon at the basis of SERS is, in fact, the localized surface plasmon resonance (LSPR). The LSPR plays the major role in explaining one of the two enhancing mechanisms for Raman signal in SERS: the electromagnetic enhancement, which is also the most important.

When light is in resonance with LSPR, the dipolar oscillation generates a strong electromagnetic field E_{SP} on the surface of a nanoparticle. The magnitude of that field depends on the nanoparticle radius r , the dielectric constant of the metal ϵ , its distance d from the molecule and the incident field strength E_0 (Equation 1.2):

$$E_{SP} = \frac{\epsilon - \epsilon_0}{\epsilon + 2\epsilon_0} \left(\frac{r}{r+d} \right)^3 E_0 \quad \text{Equation 1.2}$$

The molecule on the surface of nanoparticle experiences an enhancement of the electromagnetic field which is sum of the two electromagnetic fields (Equation 1.3):

$$E_M = E_{SP} + E_0 \quad \text{Equation 1.3}$$

The enhanced electric field has direct impact in the induced dipole μ_{ind} of the molecule thus leading to a drastic increase in the Raman signals.

The total enhancement factor $G_{\text{SERS}}^{\text{EM}}$ is given by the product of the individual enhancement factor of the laser $|A(\nu_L)|^2$ and of the Raman scattered fields $|A(\nu_S)|^2$ which, in turn, is determined by the ratio E_M/E_0 .

Considering that Stokes shifts are small, ν_S and ν_L are almost the same frequency and the electromagnetic enhancement factor depends, therefore, on E^4 .⁹¹ Recalling equation 1.2, one can also see that the enhancement factor reaches its maximum when the condition $\varepsilon = -2\varepsilon_0$ is satisfied which happens when light is in resonance with surface plasmons and the imaginary part of the dielectric function of the metal nanoparticle is small.

The power of Raman signal in SERS depends on the number of molecules involved, the laser intensity, the two enhancement factors $|A(\nu_L)|^2$ and $|A(\nu_S)|^2$ and the effective Raman cross section of the molecule (Equation 1.4)⁹²:

$$P_{\text{SERS}} \propto N \cdot I_L \cdot |A(\nu_L)| \cdot |A(\nu_S)| \cdot \sigma_{\text{ads}}^R \quad \text{Equation 1.4}$$

However, electromagnetic enhancement is not the only mechanism explaining SERS. In fact, electromagnetic enhancement should be a non-selective amplifier for Raman signal of molecules adsorbed on nanoparticles. In practice, studies reported that CO and N₂ molecules differ by a factor of 200 in their SERS intensities under the same experimental conditions. These observations suggested that another mechanism takes part in SERS enhancement: the chemical enhancement (sometimes called also electronic enhancement).⁹³

Debate is still open on how exactly the chemical enhancement works but electronic interactions between the adsorbed molecule and the metal seems to be the driving force for this mechanism. In fact, it is not uncommon that lowest unoccupied molecular orbital (LUMO) and highest occupied molecular orbital (HOMO) of a molecule are almost symmetrically disposed in energy with respect to Fermi's levels of the metal (Figure 1.12). In this situation, charge-transfer excitations can occur at about half the usual energy and considering that most of common SERS reporters have their lowest-lying electronic transition in the UV region, with this model charge transfer excitations occur in the visible region. When the electron returns to its initial state, emits a Raman shifted photon.^{92,93}

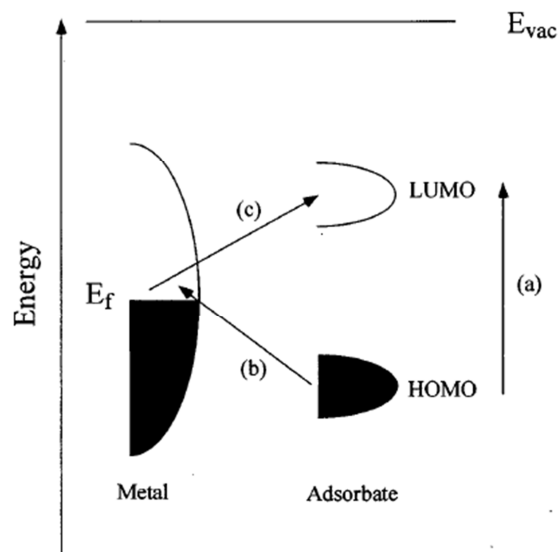


Figure 1.12 Diagram showing interactions leading to charge transfer excitations between HOMO and LUMO of a molecule with Fermi's levels of a metal nanoparticle.⁹³

Metal-molecule interactions like energy transfer to metal nanocore or intramolecular interactions are also involved in the quenching of molecule's fluorescence, allowing the observation of clear Raman signals without being covered by fluorescence emissions (Figure 1.13).⁹⁴

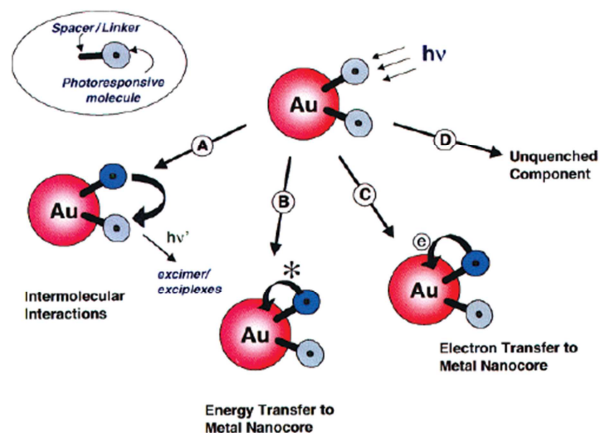


Figure 1.13 Examples of non-radiative processes implied in fluorescence quenching of Raman reporters.⁹⁴

This is important since mostly used Raman reporters are dyes which absorb in the visible region.

Experimental evaluation of enhancement factors can be obtained by equation 1.5:⁹¹

$$EF = \frac{\left[\frac{I_{SERS}}{N_{Surf}} \right]}{\left[\frac{I_{NRS}}{N_{Vol}} \right]}$$

Equation 1.5

in which I_{SERS} and N_{Surf} are the SERS intensity (at a given wavenumber) and the number of molecules bound to the metal substrate while I_{NRS} and N_{Vol} are the normal Raman signal intensity and the number of molecules in the probing volume.

Choosing the right setup for obtaining an enhancement factors of 10^{14} a single molecule SERS spectrum have been recorded, making SERS a very powerful tool.⁴²

There are some parameters which, if optimized, allows to obtain a good enhancement factor, namely a huge Raman signal. As recalled above, three are the parameters to consider: the excitation wavelength, the substrate and the SERS reporter.

Optimization of excitation laser wavelength

The enhancement of the electric field of nanoparticles or nanopatterned surfaces occurs when LSPR or SPR is excited. Noble metal nanostructured materials (Au, Ag Cu) have their LSPR or SPR excitation in the visible range, so most commons laser sources are suitable in performing SERS measurement.⁹¹ Practically, one chooses the wavelength of excitation as a function of the SERS substrate. Other parameters like irradiation time, number of acquisition spectra and laser intensity have to be tuned experimentally, time by time.

Optimization of the substrate

The size and morphology of the nanostructures on the substrate strongly influence the SERS intensity. The following considerations are restricted to gold nanoparticles, considered in this thesis, but can be extended to other metal nanoparticles.

If we consider spherical AuNPs, the upper limit in size to obtain good SERS signal correspond to that in which the dimension of the nanoparticle is comparable to the excitation wavelength ($d > 100$ nm). In this case incident electric field does not polarize homogeneously the nanoparticle, the quasi-static approximation fails and multipole excitations must be considered. Unlike the dipole, these modes are non-radiative and hence are not efficient in exciting Raman excitations. Consequently, going up with size (500-1000 nm) the light is scattered rather than absorbed, so less

inelastic scattering occurs at the surface which leads to a weakening of the electromagnetic field on the surface and the overall SERS intensity.⁹⁵

On the other side of the dimensional scale, when nanoparticles are very small ($d < 5$ nm), the onset of quantum size effects become important, the LSPR is damped and conditions to perform SERS are no longer presents. Taking in account these considerations, the optimal size to perform SERS is with AuNP from 10 nm to almost 90-100 nm.

The morphology plays also an important role in defining the parameters for good SERS signals. Intense signals are obtained using star shaped AuNPs due to huge field enhancement in star tips.⁹⁶

Using spherical nanoparticles, like in this project, huge field enhancement are obtained when nanoparticles are close together forming dimers, trimers, or more large aggregates. If a molecule resides in the region between particles it feels a huge enhancement of the electric field (if compared to the isolated nanoparticle) due to constructive coupling of the two localized surface plasmons. The mutual interaction of the two nanoparticles leads to an increase of the magnitude of the induced dipole which, in turn, leads to amplification in the polarization (Figure 1.14).^{93,95,97}

The region between the two nanoparticles is called hot spot and enhancement until 10^{11} can be easily observed. Since the field around nanoparticles decay with r^{-3} , one condition for hot spot is that interacting particles have to be very close (i.e. < 1 nm) to the surface.⁹⁵ It must also be recalled that when nanoparticles couples their plasmons, new features of LSPR emerge (longitudinal and transversal plasmon excitation), so new component in extinction spectra have to be considered in choosing the right laser excitation wavelength.

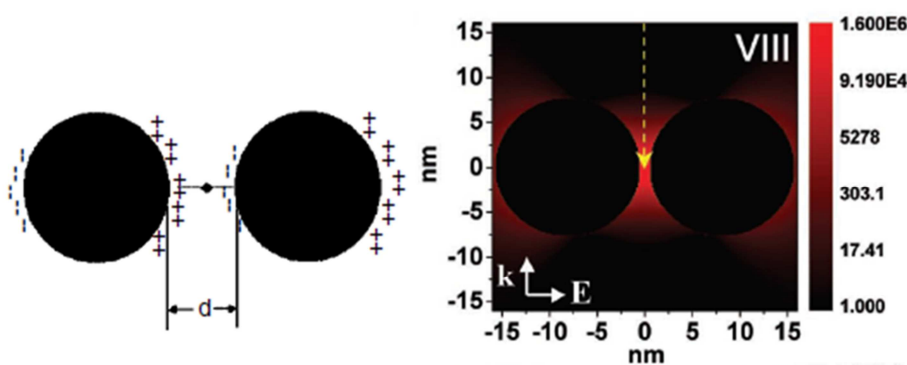


Figure 1.14. Graphical illustration of coupled surface plasmons and their effect on charge density distribution (left) and calculations of electromagnetic enhancement factors between two 15 nm gold nanoparticles (right).^{95,97}

Optimization of the SERS label

SERS label (or SERS reporter) can be considered the independent variable for this spectroscopy. This means that if the molecule it's a prefixed analyte (for example drugs, metabolites, pollutants etc) other parameters (excitation source and substrate) have to be varied to find the best experimental condition to observe the most intense SERS signals. Clearly, conjugated molecules work better than unconjugated ones because molecular vibrations that involves π electrons induces biggest polarizability changes, thus leading to huge Raman responses.

In the case of biological applications, the purpose is to obtain the most intense signals as possible to be able to track or detect nanosystems in the biological environment. For this reason a careful selection of the SERS reporters have to be done. In this case, spectroscopic characteristics of the reporter have to be taken in account. In particular, when the exciting photons energy overlaps the electronic transition energy of the SERS reporter, the Raman scattering intensity are strongly enhanced.⁹⁶ When this condition is satisfied one talks about surface enhanced resonance Raman scattering (SERRS), which allows to obtain enhancement up to 10^{14} .⁴² Since, usually, excitation wavelength and LSPR lie in the visible range, SERRS is performed using dyes with an absorption in this spectrum range.

Another condition for strong SERS signals is that the reporter molecule must reside within the space where the electromagnetic field is enhanced by excitation of LSPR. For favoring this situation, it is usually convenient to conjugate the dye directly to the surface of the nanoparticles. Conjugation can be performed either by physisorption or chemisorption and in both case the characteristics of metal nanoparticles have to be considered. For gold nanoparticles chemisorption of labels is performed exploiting Au affinity for thiols and amino groups, while physisorption usually depends on nanoparticles surface charges. For example for nanoparticles with negative surface charges, cationic dyes are to be used.

In this project, all the considered nanosystems have been engineered to exploit SERRS activity.

An advantage in using SERS/SERRS for biological applications is its high sensibility comparable to fluorescence. Moreover, with SERS nanostructures, more labels can be excited using the same wavelength, and this allows to perform multiplexed analysis in which one spectra can contain information coming from various labels

easily distinguishable in the fingerprint region. This is possible only thanks to the narrow signals of Raman spectra. The same is not possible in the case of fluorescence, where bands from diverse fluorophores overlaps and has to be excited at different wavelengths.

Plasmonic photothermal effect

Another feature of gold nanoparticles directly connected to the presence of LSPR is their ability of generating heat when irradiated. This phenomenon is called plasmonic photothermal effect and can be explained as a four step process (Figure 1.15):

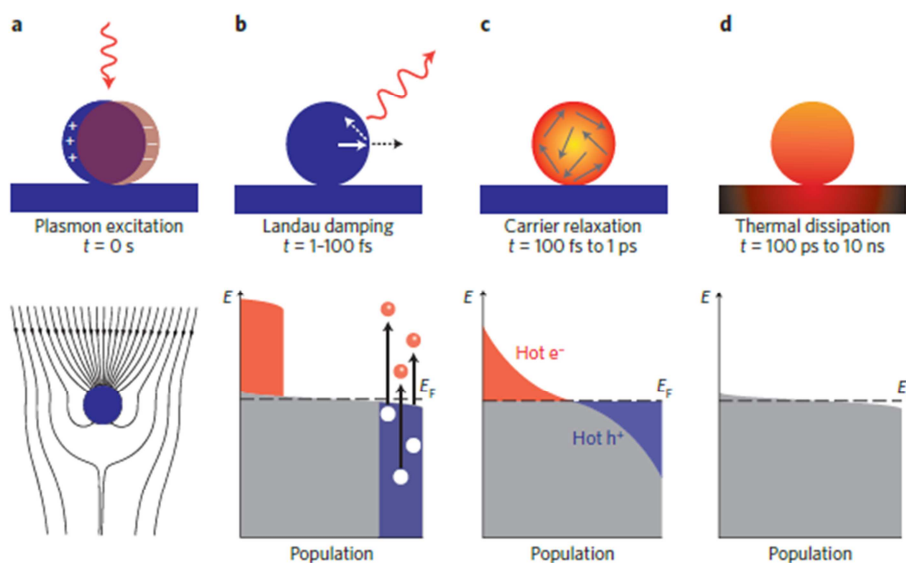


Figure 1.15 Various steps involved in plasmonic photothermal effect. Incident photon is absorbed (a) and then non-radiative effects generate hot carriers (electron-hole pairs) (b). After electron-electron and electron-phonon relaxation (c), thermal dissipation occurs (d).⁹⁸

1. Excitation of a plasmon band creates hot electrons as a consequence of photon absorption by the metal nanoparticle. Absorption is enhanced when light source has the same wavelength of plasmon excitation. (Figure 1.15a)
2. Plasmon resonance relaxes radiatively with re-emission of a photon or non-radiatively with creation of an electron-hole pair via Landau damping. This last is the necessary decay mechanism to obtain photothermal effect. Here a plasmon quantum is transferred to a single electron-hole pair excitation. (Figure 1.15b).
3. The work function (the energy required to emit an electron into vacuum) of metals are generally higher than the LSPR energies $\hbar\omega_{\text{LSPR}}$ so that hot

electrons can have energies ranging between the Fermi level E_F to $E_F + \hbar\omega_{LSPR}$ and do not escape into vacuum. For this reason their energy is first dissipated through electron-electron scattering processes and then electron-phonon interactions.

4. Last step is lattice relaxation and heat transfer to surrounding medium.⁹⁸

The importance of the plasmon resonance and excitation wavelength is relevant. Most efficient photothermal effect is obtained when laser source is in resonance with surface plasmons. As seen above, size and morphology of nanoparticles determines the position of LSPR absorption band and, as a consequence, the excitation wavelength to obtain efficient photothermal effect.^{99,100}

In section “Gold nanoparticles in cancer research” at page 16, it was recalled that heat generated by nanoparticles is used to kill cancer cells. Clearly, an LSPR in NIR is often preferred. In NIR region, light penetration in tissue is optimal because absorptions by tissues and skin pigments are limited. Nanoshells with a silica core and a variable gold shell, nanocages and nanorods are promising structures for NIR plasmonic photothermal therapy (PPTT). They are interesting because even if their synthesis is not so simple, by finely tuning shell thickness in nanoshells, number of holes and wall thickness in nanocages and aspect ratio in nanorods, one can tune the LSPR to a desired position in spectrum (figure 1.16).⁹⁸⁻¹⁰¹

However, visible absorbing gold nanoparticles are a good starting point for PPTT studies and can successfully applied in subcutaneous tumors treatment. Furthermore, their aggregation shifts the plasmon resonance in the NIR spectral region as required by an efficient photothermal effect.

Besides tumor treatment, plasmonic photothermal effect can be used for other purposes. A strange example that could open the way to other applications is the work of Halas’s group in which they used heat from gold nanoparticles to distillate ethanol. The entire process requires less energy than conventional distillation methods and a substantially higher mole fraction is obtained.¹⁰²

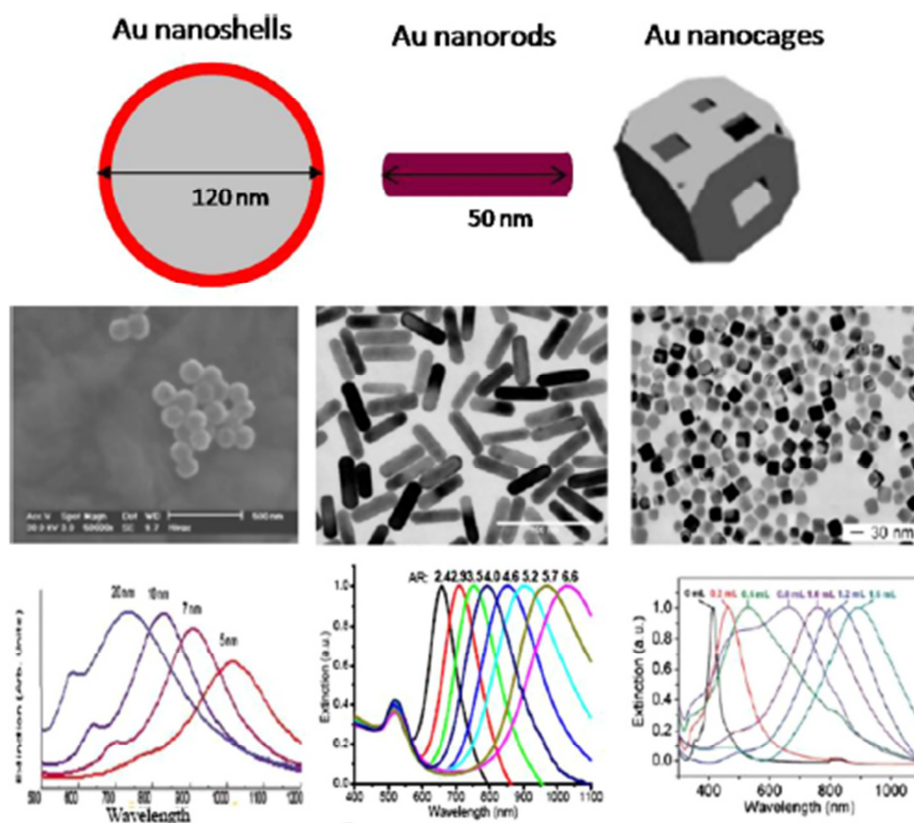


Figure 1.16 By varying morphological aspects of diverse gold nanostructures, one can tune the LSPR from visible to NIR to match the optimal wavelength to perform plasmonic photothermal therapy.⁹⁹

Iron oxide nanoparticles

In subchapter “Iron oxide nanoparticles in cancer research” the importance of FeO_xNPs in biological applications has been recalled, emphasizing the fact that large nanoparticles (above several micrometers) are already commercialized for MRI or bioseparation uses. Many forms of iron oxides exist but three of them are the most commonly used in nanomedicine: magnetite (Fe_3O_4), maghemite ($\gamma\text{-Fe}_2\text{O}_3$) and, in less extent, hematite ($\alpha\text{-Fe}_2\text{O}_3$).

Among these three oxides, magnetite exhibits the strongest magnetism, followed by maghemite.

The structure of the three iron oxides consists on planes of close-packed oxygens anions with iron cations distributed in octahedral or tetrahedral interstitial sites (Figure 1.17). Oxygens anions are in a cubic close-packed arrangement in magnetite and maghemite. Magnetite has a cubic inverse spinel structure with Fe^{2+} cations occupying half of the octahedral sites and Fe^{3+} cations distributed randomly between

tetrahedral and octahedral sites. Similarly to magnetite, maghemite has a spinel structure but with vacancies in the cation sublattice: two third of the sites are filled with Fe^{3+} regularly arranged ions, with two filled sites followed by a vacancy. One can also recall that, differently from magnetite and maghemite, in hematite (a very poor magnetic common iron oxide, $\alpha\text{-Fe}_2\text{O}_3$) oxygen anions are arranged in a hexagonal close-packed lattice with Fe^{3+} cations occupying two-thirds of the sites.^{103,104} Table 1.6 resumes physical and chemical properties of the three iron oxides.

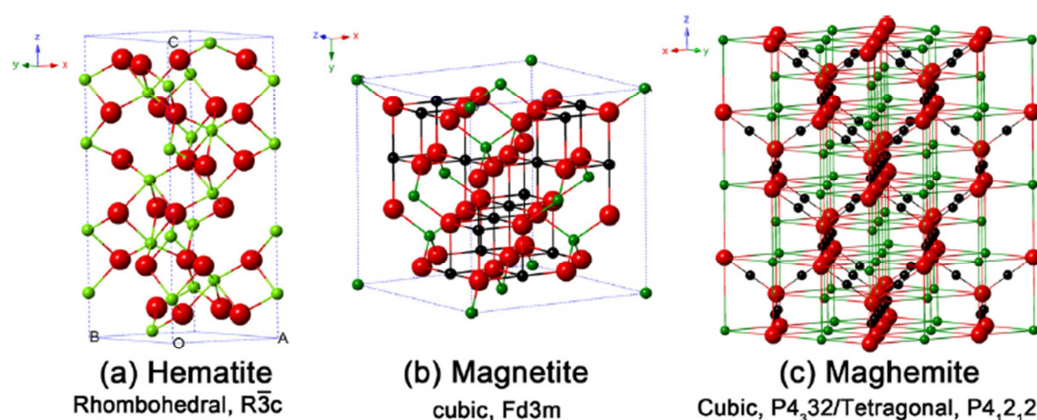


Figure 1.17 Crystal structures of Hematite, Magnetite and Maghemite. (Fe^{2+} =black ball, Fe^{3+} = green ball, O^{2-} = red ball).¹⁰³

Most common synthesis of FeO_xNPs , like AuNPs, involves the use of iron (II) and (III) salts. Clearly, varying the proportions between reagents or reaction conditions, one can obtain the three oxides selectively.

Property	Oxide		
	Hematite	Magnetite	Maghemite
Molecular formula	$\alpha\text{-Fe}_2\text{O}_3$	Fe_3O_4	$\gamma\text{-Fe}_2\text{O}_3$
Density (g/cm^3)	5.26	5.18	4.87
Melting point ($^\circ\text{C}$)	1350	1583–1597	—
Hardness	6.5	5.5	5
Type of magnetism	Weakly ferromagnetic or antiferromagnetic	Ferromagnetic	Ferrimagnetic
Curie temperature (K)	956	850	820–986
M_s at 300 K ($\text{A}\cdot\text{m}^2/\text{kg}$)	0.3	92–100	60–80
Standard free energy of formation ΔG_f° (kJ/mol)	-742.7	-1012.6	-711.1
Crystallographic system	Rhombohedral, hexagonal	Cubic	Cubic or tetragonal
Structural type	Corundum	Inverse spinel	Defect spinel
Space group	$R\bar{3}c$ (hexagonal)	$Fd\bar{3}m$	$P4_332$ (cubic); $P4_12_12$ (tetragonal)
Lattice parameter (nm)	$a = 0.5034$, $c = 1.375$ (hexagonal) $a_{\text{Rh}} = 0.5427$, $\alpha = 55.3^\circ$ (rhombohedral)	$a = 0.8396$	$a = 0.83474$ (cubic); $a = 0.8347$, $c = 2.501$ (tetragonal)

Table 1.6 Physical and chemical properties of iron oxides.¹⁰⁴

Some of the most used synthesis strategies are briefly described below, in particular for obtaining magnetite nanoparticles: the most interesting oxide because of its magnetic properties.

Synthesis strategies

Several methods are available for the synthesis of iron oxide nanoparticles. Like for gold nanoparticles, chemical routes are the most commonly used due to their relative simplicity and inexpensiveness (figure 1.18). However, physical and biological syntheses are sometimes preferred depending on the final applications.

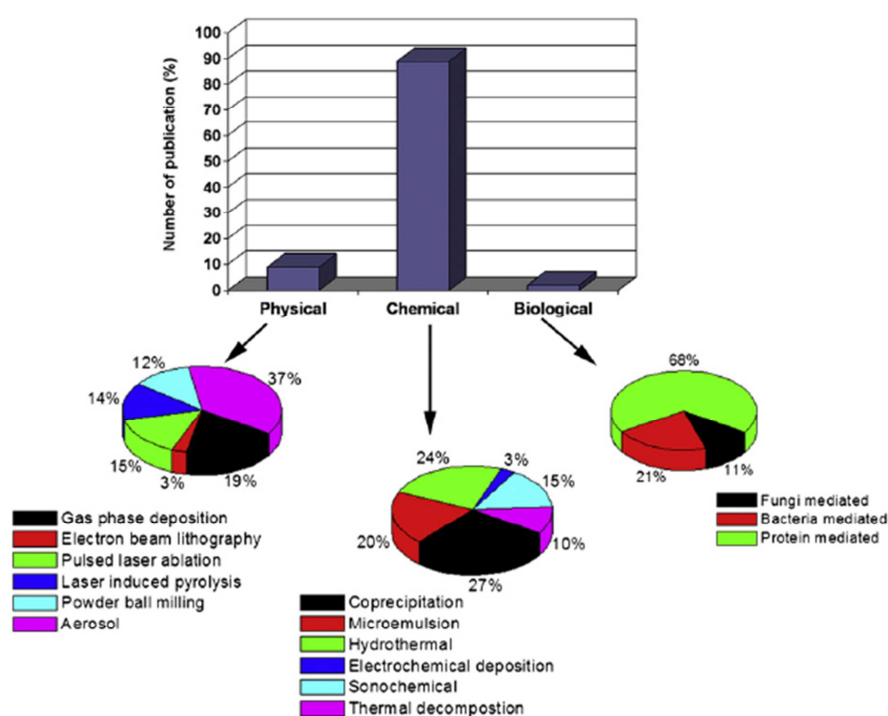


Figure 1.18 Comparison of published works (data of 2011) on the synthesis of iron oxide nanoparticles by chemical, physical and biological methods.¹⁰⁵

Coprecipitation method

This is the most common method for the synthesis of iron oxide nanoparticles. It is based on the simultaneous precipitation of Fe^{3+} and Fe^{2+} ions in basic conditions:



If performed with a stoichiometric ratio of 2/1 ($\text{Fe}^{3+}/\text{Fe}^{2+}$), magnetite nanoparticles are obtained. The pH of the solution has to be within 8 and 14 and reaction has to be performed in a non-oxidizing environment, which is usually obtained with a nitrogen flux. In fact, magnetite is not very stable and is sensitive to oxidation, which leads to the formation of maghemite:



The main advantage in the coprecipitation method is that large amounts of particles can be obtained, with narrow sizes ranging from 2nm to 17 nm. Sizes and shapes can be controlled varying reaction conditions (pH, temperature, time, injection fluxes and ionic strength of the environment). Carboxylated chelating agents (such as citric, gluconic or oleic acid) or polymer surface complexing agents (dextran, starch, carboxydextran or PVA) must be used during the formations, for stabilizing the nanoparticles and allows to control the size of nanoparticles and contribute to their stabilization.⁴⁷

Micelles or water-in-oil microemulsion method

Similarly to AuNPs, micelles or water-in-oil microemulsions are quite often used for the production of iron oxide nanoparticles. The mechanism of nanoparticles formation is based on the coprecipitation method, but nucleation and growth occur inside the micelles/inverse micelles. With this method iron oxide nanoparticles from 2-3 nm up to 100 nm can be obtained. An advantage of this synthesis is a good size control, which in turn depends on micelles/emulsion dimension. Clearly, depending on the surfactant used and solution properties, different sizes can be obtained. Also in this case, the use of stabilizers is needed: they can be in solution but sometimes the micelles are studied to act also as stabilizers when a desired size is needed. One of the drawbacks of this synthesis method is the use of potentially toxic surfactants and solvents, which, in particular sensitive environment, like the biological, can create potential problems.^{47,103,106}

Hydrothermal and thermal decomposition methods

In hydrothermal synthesis, aqueous solutions of iron salts or organometallic precursors are treated in closed vessel at high temperature (130-250°C) and high pressure (0.4-4 mPa). These conditions allow nucleation and growth of iron oxide nanoparticles with narrow size distributions. In thermal decomposition method,

nanoparticles forms after the decomposition at high temperature of organometallic or coordinated iron salts in organic solvents. Common ferric salts include $\text{Fe}(\text{CO})_5$, $\text{Fe}(\text{acac})_3$ (acac = acetylacetonate), iron oleate, $\text{Fe}(\text{Cup})_3$ (Cup = N-nitrosophenylhydroxylamine), Prussian blue ($\text{Fe}_4[\text{Fe}(\text{CN})_6 \cdot 14\text{H}_2\text{O}]$), Fe-urea complex ($[\text{Fe}(\text{CON}_2\text{H}_4)_6](\text{NO}_3)_3$), ferrocene ($\text{Fe}(\text{C}_5\text{H}_5)_2$), and $\text{Fe}_3(\text{CO})_{12}$.

Iron oxide nanoparticles produced with thermal decomposition synthesis show crystallinity and narrower size distribution with respect to the co-precipitation synthesis. With this method stabilizers are needed and nanoparticles are soluble only in non-polar solvents. The use of potentially toxic stabilizers or precursor and the impossibility to dissolve nanoparticles in aqueous solvents make these nanoparticles less suitable for use in nanomedicine.^{103,106}

Other chemical methods

Electrochemical synthesis allows to obtain maghemite or magnetite nanoparticles. The synthesis is performed using an iron electrode immersed in aqueous solution of DMF. Adjusting the current density it is possible to control nanoparticles sizes.

Another method which is a valid alternative to thermal methods is sonolysis. Here ultrasounds generate cavitation bubble which release high quantity of energy when they collapse. This energy, in the form of high pressure and temperature, enable the decomposition of organometallic precursor (like in thermal synthesis) thus leading to formation of iron oxide nanoparticles. Also in this case, stabilizers are needed to limiting the growth of nanoparticles.^{47,103}

Physical methods

Regarding physical methods, the most used are spray and laser pyrolysis. In spray pyrolysis, a solution of ferric salts in organic solvents with a reducing agent is sprayed through reactors at high temperature, where the aerosol solute condenses and solvent evaporates. The dried residue consists of nanoparticles which size is determined by initial droplet size. Laser pyrolysis can be considered a gas-phase synthesis. In this case, an opportune laser heats a gas mixture in which an iron precursor is present. Heating generates small non-aggregated iron oxide nanoparticles.⁴⁷

In this work iron oxide nanoparticles are synthesized with laser ablation method, like for gold nanoparticles. A section dedicated to this physical method is provided below.

Magnetic properties

A material is said to be paramagnetic when the individual atomic magnetic moments are randomly aligned with respect to each other and, because of this, the net magnetic moment is zero (see figure 1.19)

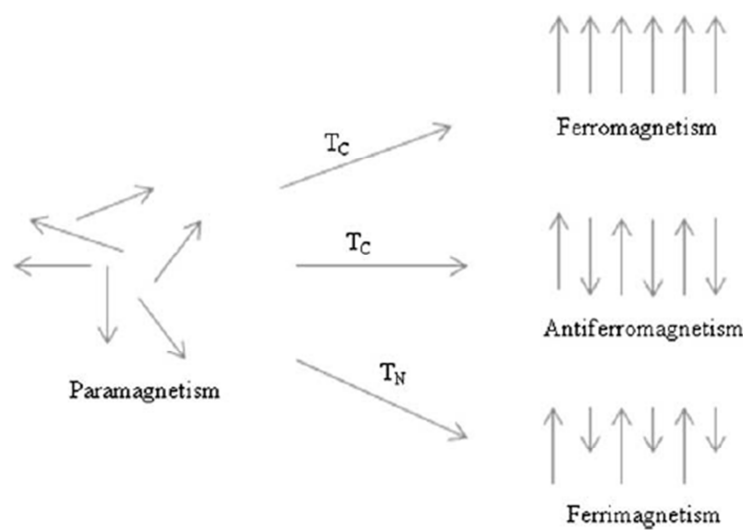


Figure 1.19 The alignment of atomic magnetic moments in different materials.¹⁰⁴

If an external magnetic field is applied, some of these magnetic moments will align and the entire crystal will show a net magnetic moment.

In a ferromagnetic crystal, all magnetic moments are aligned even without an external magnetic field while in a ferrimagnetic crystal (like magnetite) a net magnetic moment is also present, but it comes from two types of atoms with moments of different strength arranged in antiparallel fashion. When antiparallel moments have the same magnitude the crystal is said to be antiferromagnetic and no net magnetic moment is present. In a bulk ferromagnetic material, the magnetization M is defined as the vector sum of all the magnetic moments per unit volume. Bulk material contains domains with each domain having its own magnetization vector arising from the alignment of single magnetic moments. It is also probable that magnetization vectors of domains are not aligned to each other. For this reason the

global magnetization of the material is less than its value when all atoms magnetic moments are perfectly aligned (Figure 1.20).

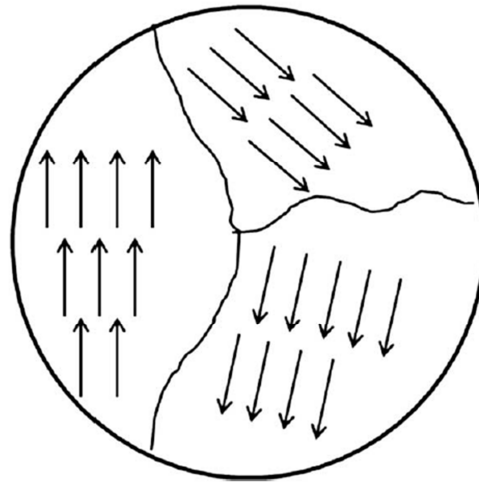


Figure 1.20 Magnetic domains in bulk materials.¹⁰⁴

However, when the length scale of the material become small, the number of domains decreases until a single domain is present, like for iron oxide nanoparticles under a certain critical size.

Figure 1.21, shows the variation of the magnetization M when an external magnetic field with strength H is applied.

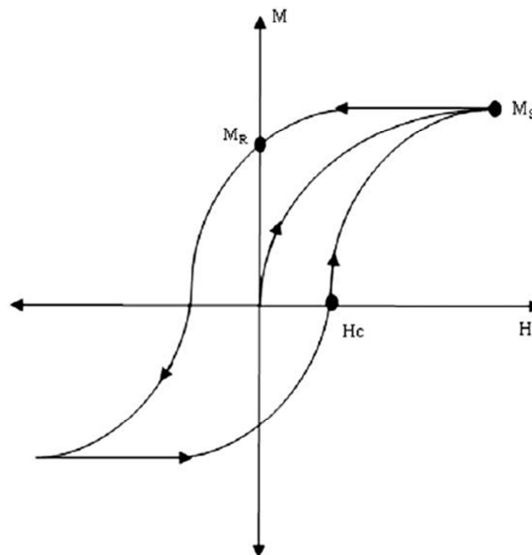


Figure 1.21 Variation of the magnetization M under an external magnetic field H .¹⁰⁴

When the external magnetic field H is applied to a ferromagnet, the magnetization M increase with H untill saturation magnetization value M_S is reached. The curve shows a hysteresis loop because domains do not return to their original orientation when H

decreases. For this reason, when H returns to zero, a residual magnetization M_R is still present. M_R can be removed applying a coercive field H_C in the opposite direction respect of that originally applied.

A single domain magnetic material has no hysteresis loop because no residual magnetization is present after magnetic field removal and is said to be superparamagnetic. Superparamagnetism is typical of iron oxide nanoparticles smaller than a certain size (20-30 nm), namely when their dimensions are comparable with that of a single domain.

Above a certain temperature, magnetic materials lose their magnetization due to thermal fluctuations of individual magnetic moments, which lead to a disordered arrangement of the magnetic moments. For ferrimagnetic and ferromagnetic materials this temperature is the Curie temperature T_C , while for antiferromagnetic materials it is the Néel temperature T_N . Superparamagnetic nanoparticles maintains an ordered arrangement below the blocking temperature T_B .

The strong magnetic moment of iron atom derives from the four unpaired electrons in its $3d$ orbitals.

Hematite is weakly ferromagnetic at room temperature and becomes paramagnetic above its Curie temperature at 956 K. It also undergoes a phase transition to an antiferromagnetic state at 260 K (Morin temperature, T_M). Its magnetic behavior can be improved decreasing nanoparticles size (Morin temperature tends to vanish) while a poor crystallinity and substitution cations can lower also T_C . For this reason, hematite nanoparticles are not the best choice for application like bioseparation because they are not efficient.

On the other hand, magnetite is ferrimagnetic at room temperature and has a Curie temperature of 850 K and also possesses the highest saturation magnetization among the three metal oxides. Magnetite nanoparticles are superparamagnetic below 25-30 nm. However this value depends on the synthesis route and particles morphology and in literature it is quite difficult to find an agreement on that value. Thanks to their magnetic properties, magnetite nanoparticles are the most preferred for biological/nanomedicine uses.

Maghemite is also ferrimagnetic at room temperature, but it's unstable at high temperature and loses susceptibility with time. At approximately 400°C undergoes an irreversible crystallographic change in hematite. For this reason its Curie temperature is difficult to estimate although it is supposed to be between 820 K and

926 K. Maghemite nanoparticles below 10 nm are superparamagnetic at room temperature. However, also in this case synthesis and morphology can affect magnetic properties. Maghemite nanoparticles can also be efficiently used for biological applications, as an alternative to magnetite nanoparticles.

As stated above, magnetic properties of iron oxide nanoparticles strongly depend on the composition, the synthesis adopted, morphology and dimension. However, also subsequent surface modifications have demonstrated to contribute to variations in their properties.¹⁰⁴

Chemical properties

Like gold nanoparticles, the chemical properties of iron oxide nanoparticles have been extensively studied. Surface modifications are, for these nanoparticles, of fundamental importance because they help to (i) improve FeO_xNPs stability and (ii) give new properties to nanoparticles. In this last category the surface chemistry of iron oxide nanoparticles is used to introduce new functional groups, useful for further functionalization, but also to improve their biocompatibility.

The stabilization of nanoparticles helps preventing their aggregation in biological medium and/or when exposed to a magnetic field (like in bioseparation assays). Generally, there are two major forces involved in interparticle interactions: van der Waals short-range attractive forces and electrostatic repulsive forces. The Derjaguin-Landau-Verwey-Overbeek (DLVO) theory well describes these two forces. In the case of magnetic suspension, also magnetic dipolar interactions have to be taken into account.⁴⁷ In the case of superparamagnetic nanoparticles, where no remanence and coercivity is found, the aggregation phenomenon is negligible at room temperature.

With all these parameters, it's easy to understand why the functionalization of iron oxide nanoparticles is a crucial point, especially when their final destination use is in biotechnology or nanomedicine.

In general, nanoparticles can be stabilized exploiting the steric and/or electrostatic repulsions. Steric repulsion is often preferred because, once performed, aggregation is avoided also in the case of important changes in pH or ionic strength of the solution. Long polymer chains physisorbed or chemisorbed on nanoparticles surfaces are used in steric stabilization.

Electrostatic repulsion is extremely sensitive to pH and ionic strength of the solution and can be followed through the knowledge of the Z-potential, a measure of the

surface charges given by the potential that they generate just outside the electrical double layer. However, electrostatic stabilized nanoparticles have the advantage of a bare surface, completely disposable for further functionalizations.

In iron oxide, the iron atoms on the surface act as a Lewis acid and coordinate with molecules that donate lone-pair electrons. In aqueous solution, Fe atoms coordinate with water which readily dissociates leaving iron oxide surface hydroxyl functionalized. Due to amphoteric nature of –OH groups, they may react with acids or bases. For this reason, depending on the pH of the solution, the surface of magnetite can be positively or negatively charged. For magnetite nanoparticles, the isoelectric point (also called point of zero charge, PZC), is observed at a pH of about 6.8, very close to that of biological environments.⁴⁷

At PZC, the charge density on nanoparticle surface is too small and they tend to aggregate, sometimes irreversibly (coagulation).

Controlling both electrostatic and steric repulsion, one obtains stable nanoparticles.

Functional groups like carboxylates, phosphates and sulfates are known to bind to magnetite surface.

Citric acid is a common carboxylated stabilizer: it coordinates via one or two carboxylate groups, leaving the other group exposed to the solvent which is responsible of the negative surface charge and hydrophilicity.⁴⁷

Other frequently used carboxylated compounds are oleic acid and lauric acid, used for synthesis in organic solvents.

To enhance FeO_xNPs biocompatibility, very common coatings are polysaccharides and biopolymers like dextran, carboxymethylated-dextran, carboxydextran, starch, alginate, chitosan and carboxymethylcellulose.

Polyethylenglycole (PEG) is also a common biocompatible stabilizing agent, usually with a carboxy or phosphate terminal group.¹⁰⁶

Other polymers, with their advantages when used in iron oxide nanoparticles are listed in table 1.7.

Polymers	Advantages	
Natural Polymers	Dextran	Enables optimum polar interactions with iron oxide surfaces, improves the blood circulation time, stability, and biocompatibility
	Starch	Improves the biocompatibility, good for MRI, and drug target delivery
	Gelatin	Used as a gelling agent, hydrophilic emulsifier, biocompatible
	Chitosan	Non-toxic, alkaline, hydrophilic, widely used as non-viral gene delivery system, biocompatible, and hydrophilic
Synthetic Polymers	Poly(ethyleneglycol) (PEG)	Enhance the hydrophilicity and water-solubility, improves the biocompatibility, blood circulation times
	Poly(vinyl alcohol) (PVA)	Prevents agglomeration, giving rise to monodispersibility
	Poly(lactide acid) (PLA)	Improves the biocompatibility, biodegradability, and low toxicity in human body
	Alginate	Improves the stability and biocompatibility
	Polymethylmethacrylate (PMMA)	Generally used as thermosensitive drug delivery and cell separation
	Polyacrylic acid (PAA)	Improves stability and biocompatibility as well as bioconjugation

Table 1.7 Organic natural and synthetic polymers used for FeO_xNPs coating.¹⁰⁶

There is another coating, which is very common for iron oxide nanoparticles and provides new surface functionalities: the silica coating.

A sol-gel approach to surface modification

Silica is the most common compound for preparing functionalized iron oxide nanoparticles. This coating has three main advantages¹⁰³:

1. Stability is improved and interparticle interactions (magnetic dipole interactions) are avoided.
2. FeO_x@SiO nanoparticles possess good stability and good biocompatibility and are hydrophilic.
3. The technology for the synthesis of these nanocomposites is already mature and easy to control.

The process involved is a sol-gel reaction and the most common is the Stöber synthesis¹⁰⁷, also used in this project.

Stöber synthesis has been named after the scientist who discovered this reaction in the '60s. In his work, "Controlled growth of monodisperse silica spheres in the micron size range", he describes the synthesis of silica nanoparticle starting from an alcoholic solution of precursor.

This sol-gel synthesis is a two-step reaction: in a first step, an organosilane precursor is dissolved in an alcohol/water solution in the presence of catalytic quantities of a base like ammonia. In these conditions the precursor hydrolyzes. The second step involves condensation of the hydrolyzed precursor in forming spherical silica nanoparticles.

If this reaction is performed in presence of other nanoparticles, like iron oxide nanoparticles, a shell of silica forms around them.

Figure 1.22 shows the Stöber synthesis in the presence of iron oxide nanoparticles.

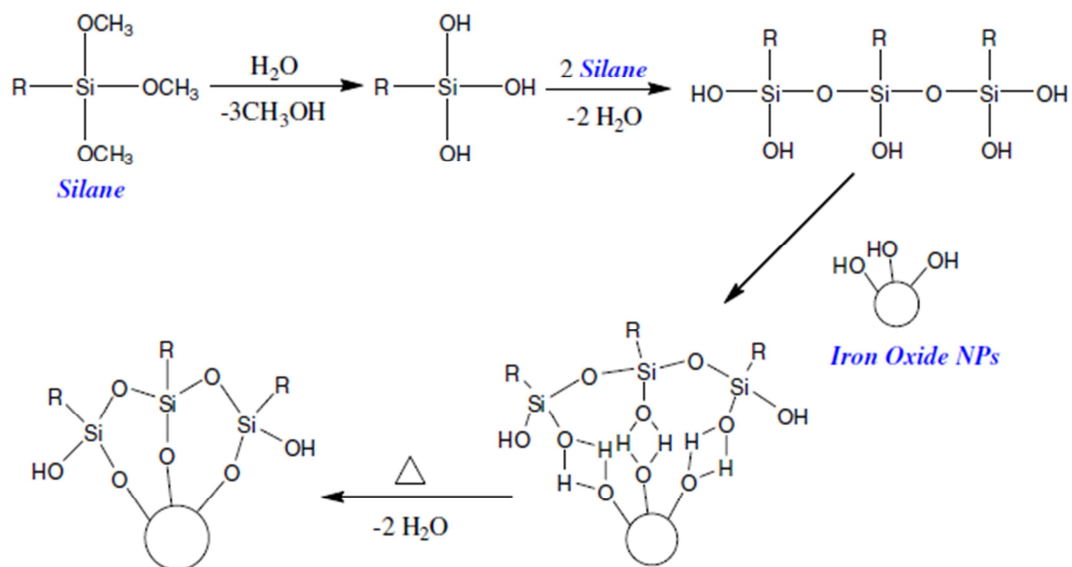


Figure 1.22 Mechanism of the formation of a shell on iron oxide nanoparticles. The firsts two steps are called Stöber or sol-gel synthesis.¹⁰³

Here, the hydroxyl groups on the surface of iron oxide nanoparticles reacted with the methoxy groups of the silane molecule leading to the formation of Si-O bonds and leaving the terminal functional groups (-R) available.

The simplest organosilane which can be used for this synthesis is TEOS (tetraethylorthosilicate). However, there is often the necessity to have specific functional groups on the surface, so that further reaction can be performed.

In this case, precursor like APTES ((3-aminopropyl)triethoxysilane) or MPTMS ((3-mercaptopropyl)trimethoxysilane) provides $-\text{NH}_2$ and $-\text{SH}$ groups respectively (Figure 1.23).

Surface exposed amino groups could serve, for example, as a reaction site for terminal $-\text{COOH}$ groups of a peptide to obtain bioactive nanoparticles.

In chapter 3 of this thesis, the $-\text{SH}$ groups of MPTMS coated iron oxide nanoparticles serves as binding site for gold nanoparticles to create a multifunctional magneto-plasmonic structures.

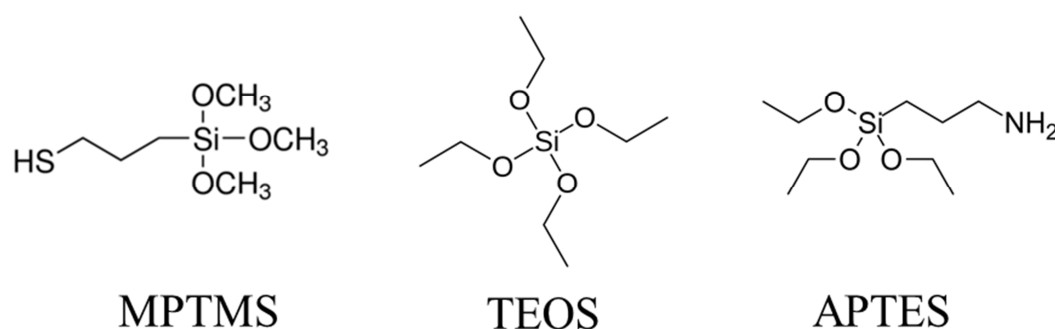


Figure 1.23 TEOS is the most simple organosilane precursor for Stöber reaction. MPTMS and APTES are used to obtain surface exposed thiol and amino groups respectively.

Besides functional groups, the new composite structure can have a different surface charge with respect to iron oxide nanoparticles. MPTMS and TEOS coated nanoparticles present negative charges at physiological pH due to partially unprotonated $-OH$ surface groups. On the other hand APTES gives rise to positively charged nanocomposites due to partially protonated amino groups at physiological pH.

Considering that iron oxide nanoparticles have low Z-potential values (usually 0-10 mV in absolute value) at physiological pH, the silica coating, either performed with TEOS, MPTMS, or APTES (or any other precursor) could give rise to Z-potential values up to 40 mV (in absolute value) thus contributing to a determining electrostatic stabilization.

Magnetic composite nanomaterials can have different morphologies (Figure 1.24) depending on the synthesis strategy or the destination use.¹⁰³ The most common is the core-shell structure with an iron oxide nanoparticle coated with a silica shell (also indicated as $FeO_xNP@Si$ or $FeO_xNP@SiO$ or $FeO_xNP@TEOS$ etc.). Other interesting structures are matrix-disperse structures in which, similarly to this project, more than one nanoparticles is embedded in the silica matrix. This type of nanostructure is useful in bioseparation because when exposed to a magnetic field it migrates faster than a single core-shell structure, so the separation time is drastically reduced.⁵³

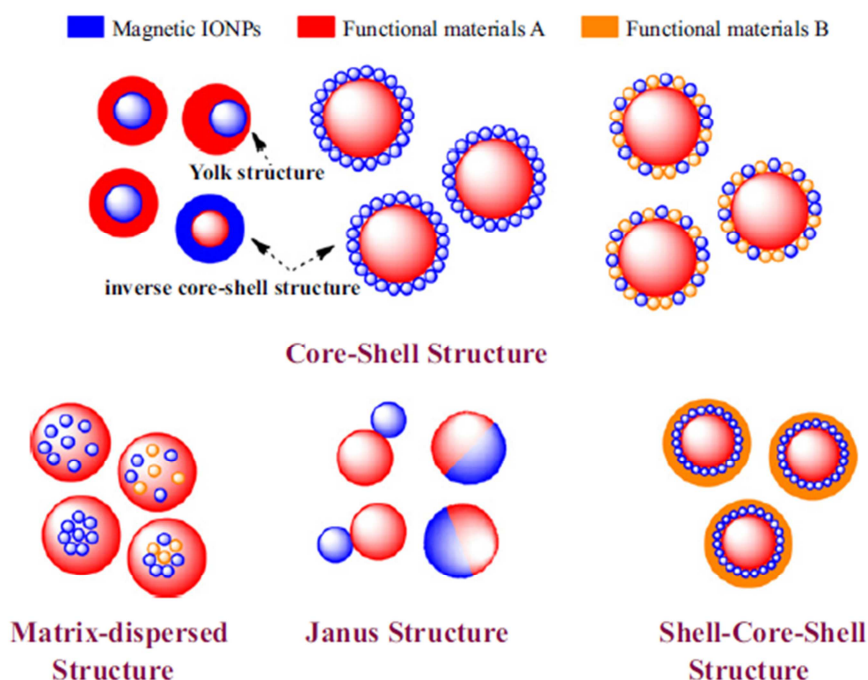


Figure 1.24 Different morphologies of nanostructured materials. Blue color is for iron oxide, while red and orange are other non-magnetic materials like silica or, for example, gold.¹⁰³

The last interesting characteristic of silica-coated nanoparticles is that small molecules, like fluorescent dyes, can remain embedded in the silica shell if the synthesis is performed in the presence of these molecules. At the end one obtains fluorescent magnetic nanoparticles that can, for example, be tracked using a fluorescent microscope.¹⁰⁸

This strategy will be used in this thesis in chapter 3, but, as it will be shown, the particles will be used for SERS measurements.

Common synthesis for magneto-plasmonic materials

There's a wide literature on the synthesis of magneto-plasmonic materials, due to the multifunctionality that makes them an attractive tools in several fields. Earlier in this introduction some of their applications in cancer research were discussed. This subchapter will focus on some synthesis strategies of magneto-plasmonic materials, in particular those made of gold and iron oxide, with attention to the different morphologies which can be obtained.

Core-Satellite structures

One of the most common hybrids Au-FeO_x structures are of the core satellite type. This structure possesses a single core surrounded by multiple, usually smaller, nanoparticles of a different material called satellites. Core and satellites are linked each other through covalent bonds or other supramolecular interactions. The core must be bare or predisposed to functionalization with the opportune ligands for satellites linking.

Due to numerous satellite nanoparticles, this structure possesses high surface area and is particularly suitable for uses in catalysis or for high chemical/biochemical loading. These structures are also the starting point for the synthesis of core-shell particles.

The most common structure is FeO_x@Au core-satellite because of the facile synthesis of the iron oxide core (50-300 nm, solvothermal route is preferred) and subsequent chloroaurate chemical reduction to form AuNP (2-20 nm).

A synthetic strategy, often used in literature, consists in using amino-functionalized silica coated magnetic nanoparticles (APTES is used as precursor for silica shell). Citrate stabilized gold nanoparticles, with their negative charges, are electrostatically attracted by -NH₃⁺ groups leading to formation of FeO_x@SiO₂@Au core-shell-satellite structures (Figure 1.25a).¹⁰⁹⁻¹¹¹

Another strategy involves the use of positive charged polymers instead of a silica coating (Figure 1.25b).

Also small molecules can serve as linker between the iron oxide core and satellite gold nanoparticles. For example, the carboxylic group of the amino acid lysine can be coupled to FeO_x core. The residual free exposed amino groups serve as attachment site for *in situ* formed gold nanoparticles in the presence of HAuCl₄ and NaBH₄ (Figure 1.25c).

Better stability of core-shell-satellite structures has been observed when, instead of electrostatic coupling between shell and AuNPs, a stronger covalent bond is present. In this case aminoacid cysteine was used to couple with the core, followed by gold reduction with ascorbic acid.¹¹¹

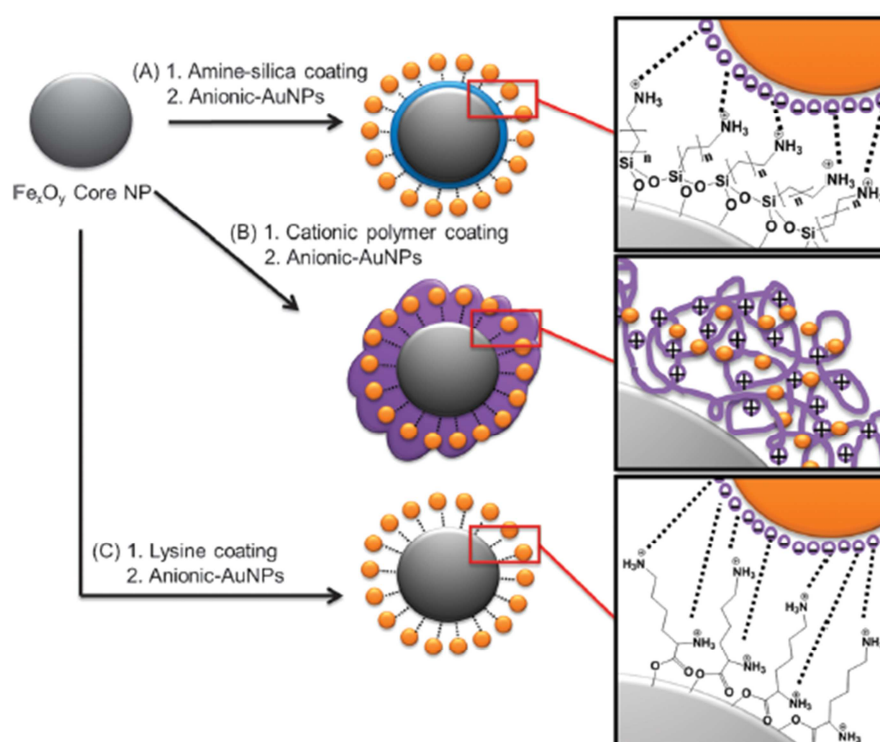


Figure 1.25 Three different ways to produce core-shell-satellite structures via electrostatic interactions: (A) amino-functionalized silica; (B) polymer coating; (C) lysine coating.

In this thesis, core-shell-satellite nanoparticles are synthesized using thiol functionalized silica (MPTMS). This strategy provides strong binding between the gold nanoparticles and the shell via Au-S bond. Previous studies demonstrated that with MPTMS the shell surface coverage by gold nanoparticles is as high as with the amino functionalized precursor (Figure 1.26).¹¹²

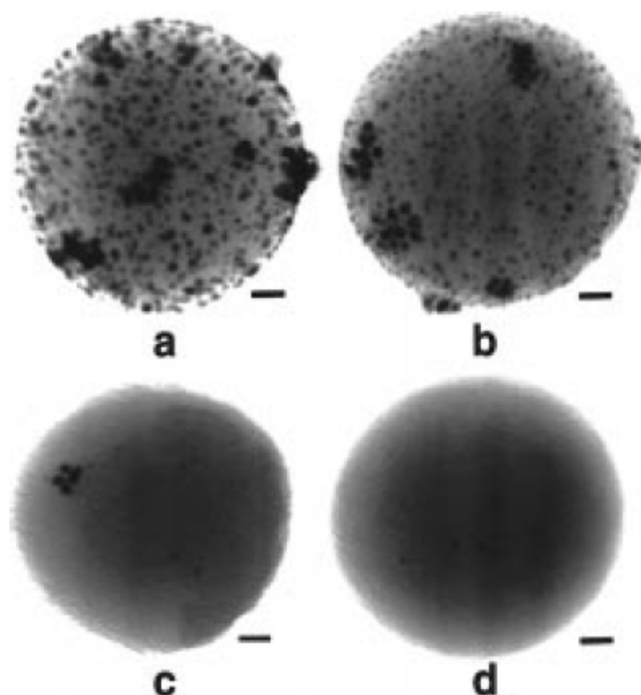


Figure 1.26 TEM images of silica nanoparticles after reaction with gold nanoparticles. The silica nanoparticles were functionalized with (a) 100% AEAPTMS (*N*-(2-aminoethyl)-3-aminopropyltrimethoxysilane), (b) 100% MPTMS, (c) 100% DPPETES (2-(Diphenylphosphino)ethyltriethoxysilane), and (d) unfunctionalized. All scale bars are 10 nm.¹¹²

Core-shell structures

Core-shell structures are different from core-shell-satellite because, in this case, the metallic core is completely covered by the shell. Core is, therefore, less exposed and the surface area to volume ratio become smaller with respect to core-shell-satellite.

Structures like Au@FeO_x core-shell particles are seldom investigated due to inactivated properties of Au core inside the iron oxide shell.

More frequent and useful are FeO_x@Au core-shell nanoparticles because chemical and optical properties of gold are still active after the synthesis.

Two principal routes are available for the synthesis: the use of prefabricated core-satellite nanoparticles with subsequent gold reduction and direct reduction on iron core. In the first one, gold satellite nanoparticles on iron oxide cores serve as nucleation sites for the reduction of the Au shell with Au³⁺ and a reducing agent. Different reducing agents can be used and varying the proportions between gold seeds and HAuCl₄ the shell thickness can be varied. The other route involves the direct formation of gold shell on the iron oxide core. For this, the iron oxide core has to be modified with some functional groups that serve as template for Au nucleation.

A common route is to synthesize magnetite nanoparticles by reduction of $\text{Fe}(\text{acac})_3$ in presence of oleylamine and oleic acid stabilizers and then perform a typical gold reduction. Just formed magnetite nanoparticles acts as nucleation centers for gold and oleylamine provides the functional groups for adsorbing Au^{3+} ions.¹¹¹

Apart these two, several other methods are available for the synthesis of $\text{FeO}_x@Au$ core-shell nanoparticles. Some of them are listed in table 1.8.

Size and shape of Fe_xO_y core	Reduction conditions	Presence of Au seeds	Thickness of Au shell/nm	Monodispersity of Au shell	Remarks
50 nm sphere/cube	$\text{HCHO} + \text{K}_2\text{CO}_3 + \text{HAuCl}_4$	Yes	Controllable 11–45	High	—
200 nm (length) rice	$\text{HCHO} + \text{K}_2\text{CO}_3 + \text{HAuCl}_4$	Yes	Controllable 13.1–27.5	High	—
258 nm sphere	$\text{NH}_2\text{OH} + \text{HAuCl}_4$	Yes	7	High	Sonication in ice bath needed
15 nm on silica nanosphere	$\text{HCHO} + \text{K}_2\text{CO}_3 + \text{HAuCl}_4$	Yes	30	High	—
18 nm sphere	$\text{Na}_2\text{S}_2\text{O}_3 + \text{ascorbic acid} + \text{HAuCl}_4$	No	5	Low	Rough Au shell formed
5 nm sphere	1,2-Hexadecanediol + OAm + $\text{Au}(\text{CH}_3\text{COO})_3$	No	0.5–2.0	High	—
25 nm sphere	$\text{NH}_2\text{OH} + \text{HAuCl}_4$ at pH 9–10	No	Controllable 1–5	High	—
4.9 nm sphere	Sodium citrate + HAuCl_4	No	7.5	Low	—
9–11 nm sphere	1,2-Hexadecanediol + OAm + $\text{Au}(\text{CH}_3\text{COO})_3$	No	Inner: 1 outer: 8–10	Low	—
10.5 nm sphere	OAm + HAuCl_4	No	1.3	Low	Non-uniform coating observed

Table 1.8 List of different reaction conditions for synthesis of $\text{FeO}_x@Au$ core-shell nanohybrids.¹¹¹

Aggregates

FeO_x -Au aggregates are structures in which iron oxide and gold nanoparticles are randomly organized in space. With respect to the other magneto-plasmonic typologies, aggregates are simpler to synthesize although some polydispersion can be observed.

A method to obtain aggregates with some control on the dimensions is that of including AuNPs and FeO_x NPs within polymers. An interesting example is found in the work by the group of Liz-Marzàn where they were able to co-encapsulate gold nanostars (AuNS) and small iron oxide nanoparticles using poly(styrene)-block-poly(acrylic acid) (PS-*b*-PAA).¹¹³ First, they separately synthesize iron oxide nanoparticles and gold nanostar using a chemical route. Then, when water is added to a THF mixture of FeO_x NPs, AuNS and polymer, the aggregates form (Figure 1.27).

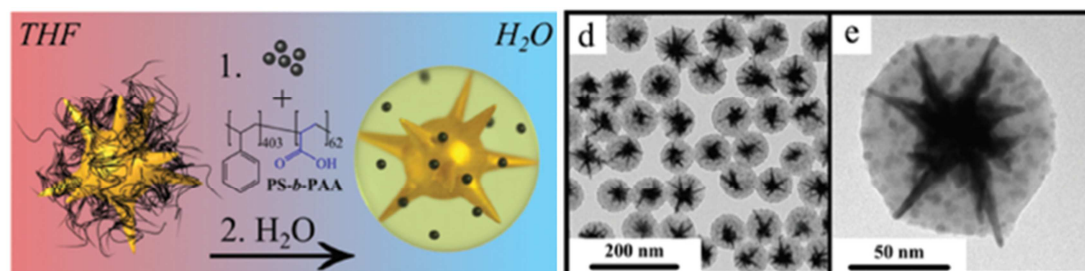


Figure 1.27 Scheme of encapsulation process for FeO_x -Au aggregates forming (left) and TEM images at different magnification of aggregates (right).¹¹³

The synthesis of magneto-plasmonic aggregates made of gold and iron oxide spherical nanoparticles is the object of this thesis. Instead of using polymer or chemicals to form aggregates, the driving force involved in our synthesis was the different electrostatic charges of FeO_x NPs and AuNPs.³¹ This methods allow to obtain nanostructures without extraneous molecules and, therefore, simple to functionalize.

Other magneto-plasmonic structures

Multi-layer plasmonic nanostructures are a sort of core-shell structures, but with more than two layers of materials.

As stated above, silica is a common coating for iron oxide nanoparticles. A frequent multilayer nanostructures consists on an iron oxide core surrounded by a silica shell on which, in turn, gold deposition is performed forming the third layer ($\text{FeO}_x@SiO_2@Au$).

Another morphology is $\text{FeO}_x@Au@SiO_2$ in which satellite gold nanoparticles are linked to the iron oxide core and then the whole system is covered with silica. In this case, silica stabilizes the core-satellite structure. Dyes can be embedded in the silica matrix to obtain SERS effect and/or fluorescent nanoparticles.

Reaction scheme for these two multi-layer structures is shown in figure 1.28.

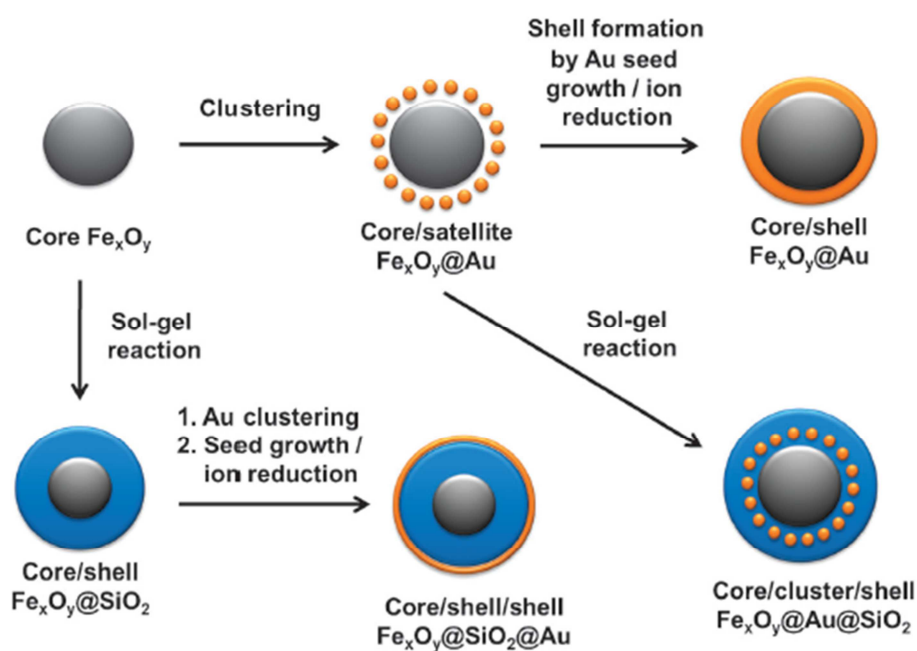


Figure 1.28 Scheme for the synthesis of magneto-plasmonic multi-layer nanostructures.¹¹¹

Another less used but interesting morphology is the so called dumbbell nanoparticles. This system is composed of one iron oxide nanoparticle and one gold nanoparticle, bonded together. Two strategies are commonly adopted: the first consists in deposit one iron oxide nanoparticle on one previously formed gold nanoparticle, in the second the two nanoparticles are formed at the same time.

Evolutions of dumbbell nanoparticles are nanoflowers. Here one gold nanoparticle is surrounded by more iron oxide nanoparticles (from 1 to 4). Figure 1.29 shows few reactions for synthesis of dumbbell nanoparticles and conformation of nanoflowers.

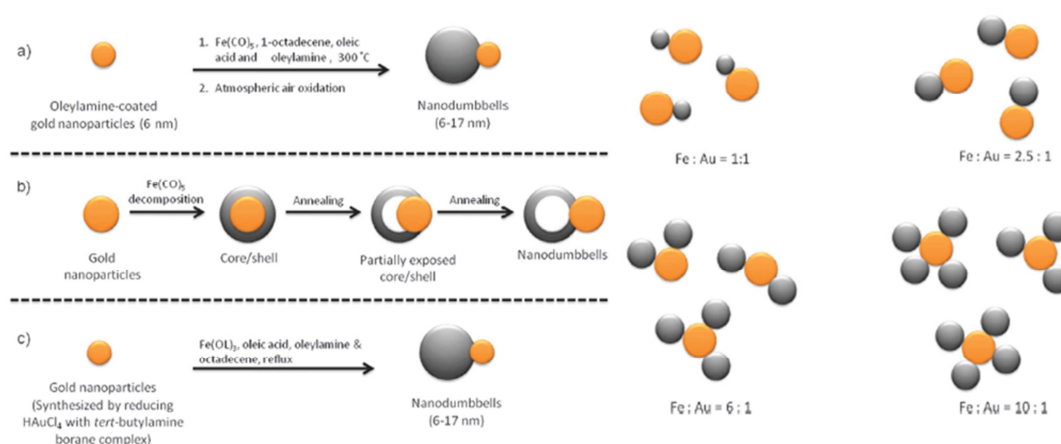


Figure 1.29 Synthesis of dumbbell nanoparticles (left) and nanoflowers (right).¹¹¹

The synthesis of these magneto-plasmonic materials is not simple because reaction times and proportions between reagents need to be carefully controlled.¹¹¹

In figure 1.30, TEM images of different kinds of magneto-plasmonic materials are reported to have a better view of what they are.

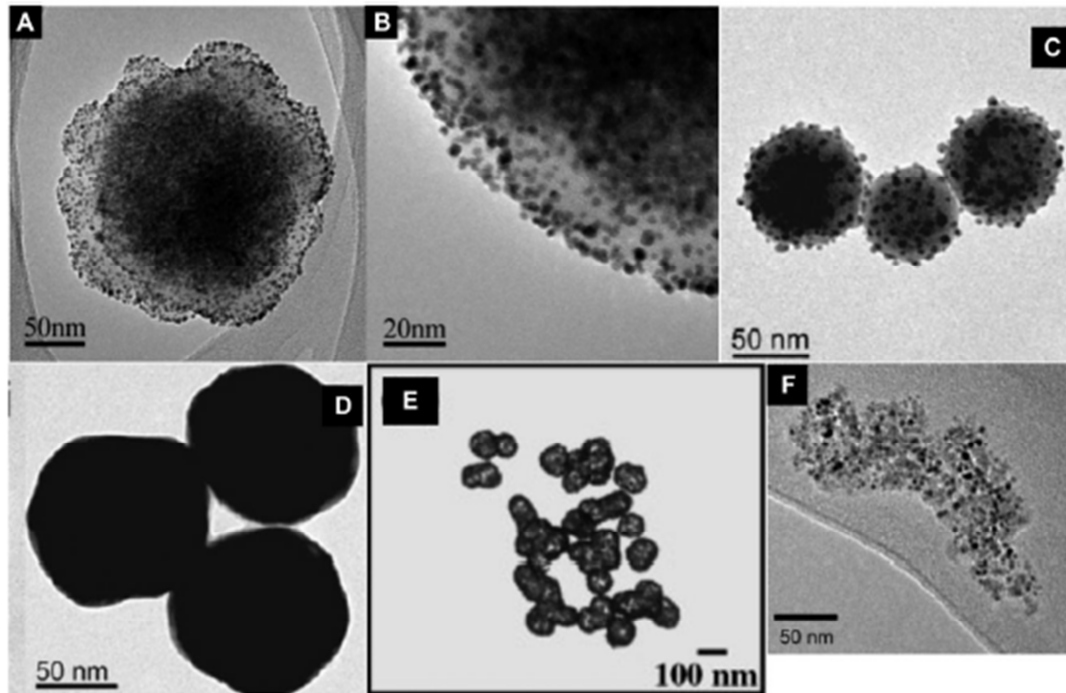


Figure 1.30 Representative TEM images of: core-shell-satellite $\text{Fe}_3\text{O}_4@polyaniline@Au$ nanoparticles using polymer as shell (A and B); $\text{FeO}_x@SiO_2@Au$ core-shell-satellite nanoparticles (C); $\text{FeO}_x@SiO_2@Au$ core-shell-shell nanoparticles (D and E); polymeric aggregates of FeO_xNPs and $Au\text{NPs}$ (F).¹¹¹

Magneto-plasmonic nanosystems like dumbbell nanoparticles or nanoflowers are interesting because denote the technical and synthetic advances in the control of nanostructured materials.

However, in the design of magneto-plasmonic nanosystems for biomedical applications an efficient but simpler system is sometimes preferred with respect to a sophisticated but less efficient one.

Dumbbell, nanoflowers, nanoroses and multilayer magneto-plasmonic structures are representative classes of nanotechnological development approaches. However, at present, literature on nanotechnology cancer research seems to be more oriented on core-shell or core-shell-satellite structures.

Important goals of nanotechnology in cancer research are active tumor targeting nanostructures to obtain easy diagnosis, drug delivery and nanoparticle mediated thermal therapies. These aims can be achieved with magneto-plasmonic systems with core-shell and core-shell-satellite configurations because:

1. Their synthesis is relatively easier and well established than other magneto-plasmonic systems.
2. Magneto-optical properties can be well controlled with simple variations of the reaction scheme.
3. Less complicated reactions and reproducibility make them more suitable for large-scale productions.

One last consideration concerns the use of toxic or potentially toxic chemicals during the synthesis. Core-shell and core-shell satellite usually requires less synthetic passages than others more complicated structures and this, often, means that the number of used chemicals is restricted. However this is not sufficient to ensure complete non-toxicity when these structures reach their final biomedical use.

For this reason, new synthetic routes, which respect also green chemistry rules, are now an important goal.

One of the approaches that follow a green chemistry approach is the Laser Ablation Synthesis in Solution (LASiS), since one can produce stable colloidal solutions without using surfactants or other stabilizing molecules.

The importance of being green: Laser Ablation Synthesis in Solution

The growing interest for biomedical applications of gold and iron oxide nanoparticles, lead scientists to think to new synthetic strategies to avoid the use of toxic or potentially toxic agents usually considered for chemical syntheses.

As widely discussed above, these nanoparticles come in contact with biological entities ranging from cells to organs and for this reason, every chemicals that could show toxic effect should be avoided. Several washings steps during synthesis are not sufficient to guarantee the absence of unwanted molecules in the final product because, apart from the procedure itself, due to the nanoparticles high surface to

volume ratio and reactivity, molecules could be adsorbed (chemically or physically) onto their surface and released in a second moment.

Apart from laser ablation, other green synthetic methodologies for the synthesis of gold and iron oxide nanoparticles use plants, fungi and other microorganisms.

Gold nanoparticles have been successfully biosynthesized using plant extracts from *Aloe Vera*¹¹⁴, Camphora leaves¹¹⁵ and *Trigonella foenum-graecum*¹¹⁶. Fungus like *Verticillium*¹¹⁷ or bacteria like *Pseudomonas Aeruginosa*¹¹⁸ and *Rhodopseudomonas capsulate*¹¹⁹ have also been used for the synthesis of AuNPs.

For the plant-mediated synthesis, enzymes like reductases, naphthoquinones, anthraquinones, polyphenols and carbohydrates are able to reduce gold ions.¹²⁰

In the case of bacteria-mediated synthesis, reductases, peptides or other proteins and metabolites are responsible for the reduction of gold.¹²¹

The same substances are implicated in the formation of iron oxide nanoparticles using fungi like *Fusarium oxysporum* and *Verticillium*¹²² or bacteria like *Magnetospirillum magnetotacticum* and *M. gryphiswaldense*¹²¹.

However, the use of plants, bacteria or fungi for the production of nanoparticles requires infrastructures and multidisciplinary technical skills which are seldom gathered in a single research group.

Laser Ablation synthesis in solution can avoid also the problem of a multidisciplinary research team because one doesn't need particular skills to work with a laser source to perform laser ablation.

Laser Ablation assisted Synthesis in Solution (LASiS)

The ablation is a process of material removal from the surface of an object through vaporization and erosion processes.

LASiS allows to obtain nanoparticles of different metals in different solvents (often water) in a relatively simple way.

The experimental set-up consists of a pulsed laser and lenses to focus the beam in the proximity of a metal target immersed in a solution inside a vessel (figure 1.31).

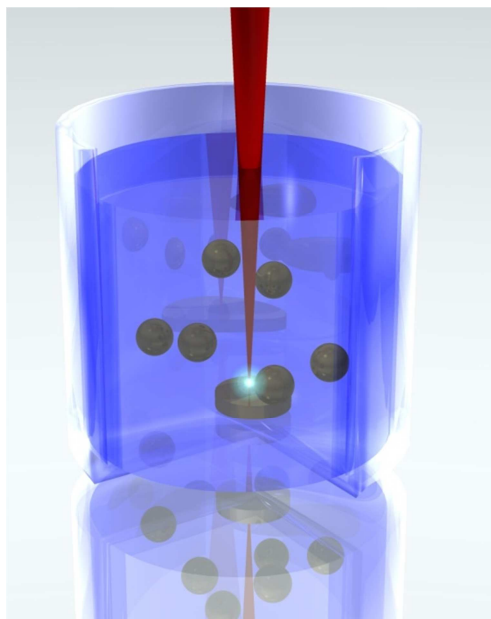


Figure 1.31 LASiS for nanoparticles synthesis consists on a pulsed laser focused in the proximity of a metal target immersed in a solvent.

LASiS is a typical top-down method since the starting material is in its bulk form.

In LASiS method, nanoparticles are formed by the condensation of a plasma plume originated from the laser ablation of a metal target immersed in liquid. Usually the metal target is positioned out of the laser focus to prevent local boiling of solvent.

Mechanism of laser ablation is still object of study due to its complexity and the short time in which it occurs.

Figure 1.32 shows the six fundamental passages involved in the mechanism of ablation by a single laser pulse. The whole process occurs in less than one millisecond.

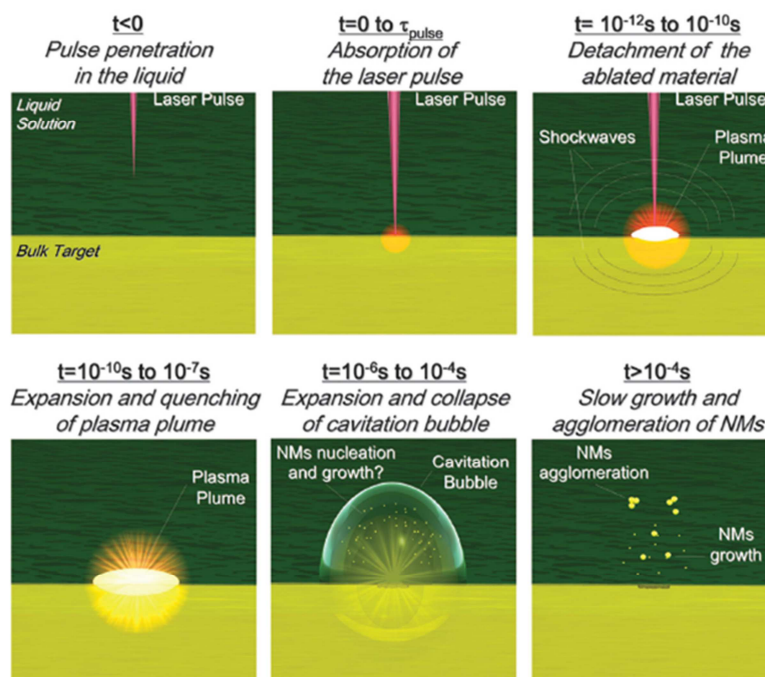


Figure 1.32 Timeline of laser ablation process in the case of ns laser pulses.¹²³

First, laser penetrates into the liquid. At this stage of the process it is important to consider that solvent can absorb laser light with the result that less energy reaches the target. In the case of ablation using a 1064 nm laser and water as solvent the absorption is negligible. To reduce the solvent absorption it is good practice to have not more than 1-2 cm of liquid above the target.

When the laser pulse reaches the metal target, multiphoton absorption and direct photoionization occurs, leading to the detachment of the ablated material. Three thermal processes are involved in the detachment of material: vaporization, normal boiling and explosive boiling. In ordinary LASiS, with laser pulses shorter than 10^{-7} s, the prevalent mechanism is explosive boiling in which the material is superheated above its critical temperature and expelled in the form of a plasma plume containing highly ionized species due to high temperature and photoionization. The plasma plume is accompanied by emission of light and shockwaves.

From 10^{-10} s to 10^{-7} s the plasma plume expands and simultaneously cools down. When the hot material inside the plasma plume starts to cool, nucleation and growth of metal nanoparticles take place. The coalescence of the firsts small nuclei lead to the final nanoparticles.

After 10^{-7} s the plasma plume is extinguished and the energy released gives rise to a cavitation bubble, which expands and collapses emitting a second shockwave. In the

last moments of laser ablation, after the collapse of the cavitation bubble ($t > 10^{-4}$ s), nanoparticles undergo chemical surface modifications. In particular surface oxidation can occur at this stage when water is the solvent.

LASiS usually produces almost spherical particles because, during nucleation and growth processes the system minimize its surface energy.¹²³

Three are the laser parameters involved in the entire process: pulse wavelength, energy and duration.

Regarding the wavelength, the use of laser light that could be absorbed by the nanoparticles should be avoided because the absorption decreases the amount of energy reaching the target. Since gold and iron oxide nanoparticles absorb UV and visible light, the use of lasers in the near infrared minimize the absorptions. Furthermore, if nanoparticles absorb laser light they can undergo further modifications. In particular, depending on the photon energy, photofragmentation or nanoparticles melting occur. The first lead to smaller nanoparticles, the second lead to bigger ones. For AuNPs this happens in particular using a 532 nm laser light, because this wavelength is near to the maximum plasmonic resonance at 520 nm (for nanoparticles with ~20 nm diameter).¹²⁴

Increasing of pulse energy influences the amount of ablated materials but also the morphology/dimension of obtained nanoparticles. Productivity increases almost linearly with pulse energy. With high energy pulses, multiple mechanism of material detachment occurs simultaneously (like fragmentation, explosion, boiling and vaporization) and nanoparticles with a non-homogeneous size distribution are obtained. Usually, with low fluences, smaller nanoparticles are obtained while high fluences causes the formation of bigger and irregular nanoparticles.

The pulse duration has his effects in particular on nanoparticles size distribution. With ns laser pulses, like in this thesis project, the pulse and the plasma plume coexists for a certain time and part of the laser energy is transferred to the plasma plume increasing its temperature, pressure and lifetime. As a consequence melted drops of the target ejected in the plume have higher chance to vaporize, leading to more homogeneous plasma plume. After cooling, nanoparticles with sharper size distribution are obtained with respect to fs and ps laser pulses.¹²³

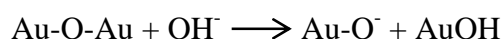
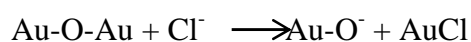
Gold and iron oxide nanoparticles obtained with LASiS

During plasma plume expansion several species can participate to chemical reactions. This reactivity is promoted by the presence of both solvent and metal excited species in the plume boundary as well as the extreme temperature and pressure reached inside the plume (10^3 K and 10^{10} - 10^9 Pa in an ordinary LASiS).

Gold nanoparticles synthesized with LASiS using water as solvent are well known to be stable for long times without the use of any stabilizing agent due to their high negative surface charge. This is due to a partial oxidation of the surface, of the order of less than 10%, caused by the ablation process itself.

In fact, XPS and FTIR experiments have evidenced the presence of Au(I), Au(III) and Au-O-Au species on the surface of LASiS synthesized gold nanoparticles.^{123,125}

The interaction between Au-O-Au bridges and negative ions in water like hydroxyl and chloride are supposed to be responsible of the formations of Au-O⁻ species according to following reactions:



The presence of chloride or hydroxyl ions in solution can therefore increase negative charges on AuNPs surface thus preventing their aggregation.

Clearly, in the case of charge-stabilized nanoparticles, the ionic strength of the solution plays a key role in the colloid stability and one needs to find the right balance between salt concentration and NPs stability.

Previous works in the laboratory in which this thesis was developed, found that this balance is realized when AuNPs are synthesized in a NaCl 10^{-5} M water solution because in this conditions one obtains a high percentage of spherical particles with dimension ranging from 15 nm to 20 nm (Figure 1.33).¹²⁵

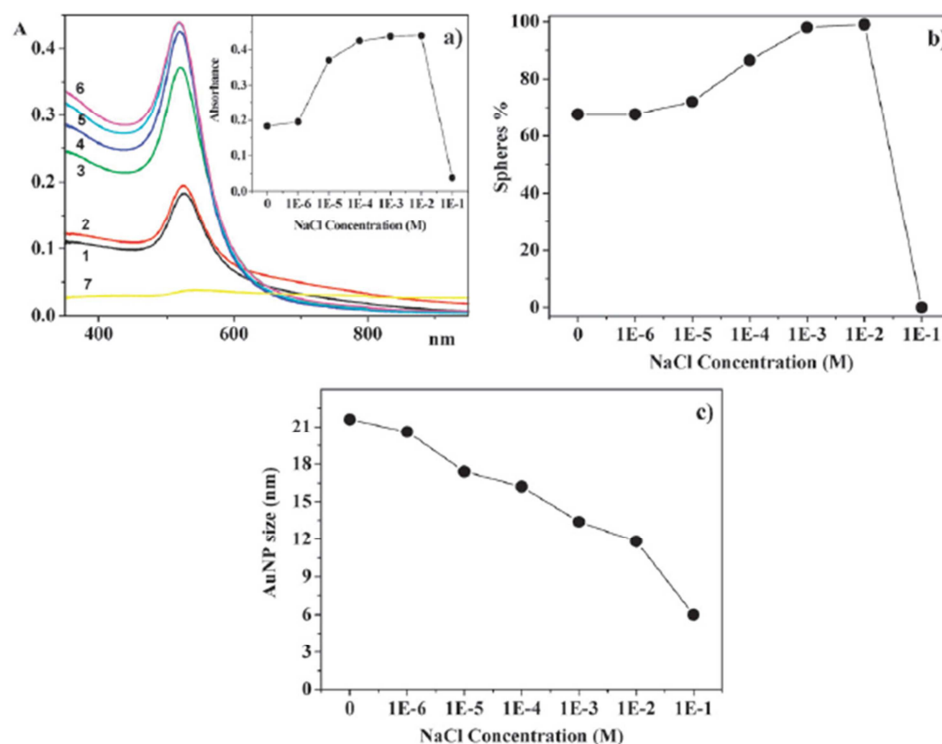


Figure 1.33 LASiS of AuNPs at different concentrations of NaCl. A) UV-Visible spectra of gold nanoparticles at different NaCl concentrations: 0M (1) 10^{-6} M (2) 10^{-5} M (3) 10^{-4} M (4) 10^{-3} M (5) 10^{-2} M (6) and 10^{-1} M(7). Inset graph reports absorbance values for all solutions. B) Percentages of spherical nanoparticles obtained as a function of NaCl concentration. C) Mean diameter of obtained AuNP as a function of NaCl concentration.¹²⁵

Clearly, increasing NaCl concentration, the electric double layer collapse and particles aggregate and precipitate.

With LASiS, AuNPs with diameter between 15 nm and 25 nm are obtained when the synthesis is performed in water while in organic solvents dimensions varies between 5 nm and 10 nm. They are mainly spherical with low percentages of spheroids and with a polycrystalline structure.¹²³⁻¹²⁶

Iron oxide nanoparticles are synthesized by ablating a pure Fe metal target in water. Also in this case reactions with water occurs.

Fe reacts with oxygen giving a mixture of oxides like magnetite (Fe_3O_4), maghemite ($\gamma\text{-Fe}_2\text{O}_3$), hematite ($\alpha\text{-Fe}_2\text{O}_3$) and wüstite (FeO). Fe reacts with water giving also amorphous hydroxides or mixed oxide-hydroxide phases.

Iron oxide nanoparticles produced with LASiS in water consists of multiphase polycrystalline spherical NPs embedded in an amorphous hydroxide phase with dimension of ca. 25 nm.

FeO_x NPs are mainly composed of magnetite (75%), hematite (22%), wustite (ca. 2%) and Fe (0) (ca. 1%) and shows superparamagnetic behaviour.

Once the amorphous phase is removed with an acid treatment, iron oxide nanoparticles possess charge stabilization, which varies with the pH of the solution (see subchapter “Iron oxide nanoparticles – Chemical properties”).^{123,127,128}

Laser ablated FeO_xNPs, like AuNPs, can remain stable for months as a stock solution.

Gold and iron oxide nanoparticles can be produced also in other solvents, but in this case, other phases can form. As an example, figure 1.34 shows TEM images and phases of AuNPs and FeO_xNPs synthesized with LASiS using various solvents.

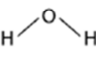
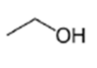
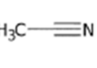
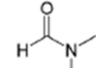

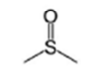
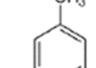
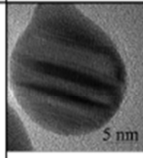
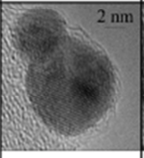
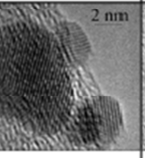
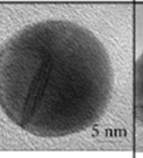
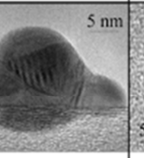
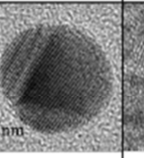
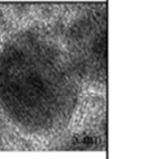
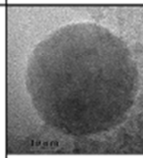
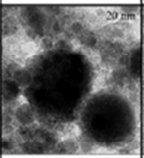
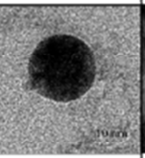
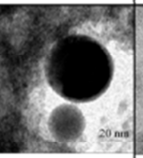
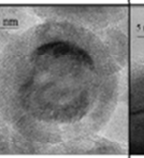
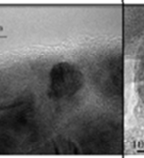
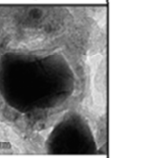
Target ↓ Solvent ↑	Water 	Ethanol 	Acetonitrile 	Dimethyl-formamide 	Tetra-hydrofuran 	Dimethyl-sulfoxide 	Toluene 
Au	 <i>Metal Au</i>	 <i>Metal Au</i>	 <i>Metal Au</i>	 <i>Metal Au</i>	 <i>Metal Au</i>	 <i>Metal Au</i>	 <i>Metal Au/ Graphite</i>
Fe	 <i>Fe₃O₄, Fe₂O₃, Fe(OOH)₂</i>	 <i>Fe₃O₄, FeC₃</i>	 <i>Fe₃O₄, Carbon</i>	 <i>Fe₃O₄, Carbon</i>	 <i>Metal Fe/ Fe₃O₄</i>	 <i>Metal Fe/ Carbon</i>	 <i>Fe-Carbide/ Graphite</i>

Figure 1.34 LASiS of Au and Fe target in different solvents lead to nanoparticles with different composition.¹²³

To conclude this brief outlook on laser ablation synthesis in solution, some pros and cons of this technique are reported. The main pros are:

1. LASiS allows to obtain nanoparticles of different materials in different solvents simply changing the metal target. The set-up remains the same and usually only minimal variations of parameters are required. Due to its versatility, there are few companies providing customized nanoparticles produced by LASiS.¹²⁹

2. LASiS method does not necessarily require the use of chemicals and wastes, if any, are minimal. For this reason is a sustainable method which also respects green chemistry principles.
3. Since the set-up is minimal and no expensive chemical are used, it can be considered a low-cost method. Manual operations are also significantly reduced with respect to chemical methods. These features facilitate also the reproducibility of the synthesis.
4. One-step functionalization is possible either *in situ* (during the ablation) or *ex situ* (after the synthesis).
5. The absence of chemicals during the synthesis and the absence of any stabilizer on nanoparticles surface make LASiS the most suitable method for the production of nanoparticles for biomedical applications.

However, LASiS has also its cons:

1. Although gram scale production has been reported¹³⁰, such productivity is, at the moment, not comparable with that of wet chemistry synthesis.
2. The control of size distribution is lower than other synthetic methods and only spherical nanoparticles can be obtained.
3. Since LASiS is a relatively young technique, a general procedure for nanoparticle production is still absent and every lab has its own procedures.

Aim of this thesis

The aim of this project is the synthesis, characterization and application in nanomedicine of magneto-plasmonic nanostructures.

The work is divided in two parts.

In the first one (chapter 2) magneto-plasmonic nanostructures are obtained aggregating gold and iron oxide nanoparticles in a nanocluster (AuFeO_xNC). The peculiarity of these aggregates is that no chemicals are used to bond nanoparticles to each other and aggregation is controlled by operating on the opposite surface charges of AuNPs and FeO_xNPs. By controlling the amount of AuNPs and FeO_xNPs, nanoclusters with both good SERRS and superparamagnetic properties are obtained.

To show the applicability of these nanostructures, AuFeO_xNC are incubated with murine macrophages which, after being mixed with other macrophages, can be

magnetically guided in solution by sorting them in less than 10 minutes. SERRS analysis at single cell level demonstrates that nanoclusters are active also in biological environment and allows the identification of cells.

In chapter 3, the synthesis of a different and engineered nanosystem is reported. In this case a magneto-plasmonic nanosystem with a core-shell-satellite (CSS) type architecture is obtained. This nanosystem is opportunely designed to minimize aspecific interactions with cells and it is functionalized with an antibody (D2B) specific for an antigen (PSMA) which is expressed by prostatic cancer cells. CSS nanostructures show also good SERRS properties thanks to gold satellite nanoparticles while magnetic characteristics are given by a core of iron oxide nanoparticles.

Their efficiency, in targeting and selection, is shown for PC3-PIP cells, positive for PSMA, and compared with PC3 cells, negative for PSMA. The quantitative results show, at picomolar concentrations, a sensitivity of 98% and a specificity approaching 100% with an overall accuracy of 98%.

CSS nanostructures are then used in plasmonic photothermal treatment of cancer cells showing viability close to 0% for PC3-PIP cells only after few minutes of irradiations, while viability of equally treated PC3 cells remains unaltered.

With these features, CSS nanostructures can be defined a complete theranostic agent. Moreover, both AuFeO_x NC and CSS nanostructures are synthesized starting from laser ablated nanoparticles and, therefore, are more suitable for biomedical use thanks to the enhanced biocompatibility of laser ablated nanoparticles.

References

- (1) Feynman, R. P. There's plenty of room at the bottom, *Engineering and science* **1960**, 23, 22-36.
- (2) Taniguchi, N. In *In On the basic concept of nanotechnology*; Proc. Intl. Conf. Prod. Eng. Tokyo, Part II, Japan Society of Precision Engineering; 1974; , pp 18-23.
- (3) Eric, D. K. Engines of Creation. *The Coming Era of Nanotechnology* **1986**
- (4) Binnig, G.; Fuchs, H.; Gerber, C.; Rohrer, H.; Stoll, E.; Tosatti, E. Energy-dependent state-density corrugation of a graphite surface as seen by scanning tunneling microscopy, *EPL (Europhysics Letters)* **1986**, 1, 31.
- (5) Binnig, G.; Rohrer, H. In *Scanning tunneling microscopy*; Scanning tunneling microscopy; Springer: 1986; pp 40-54.
- (6) Eigler, D. M.; Schweizer, E. K. Positioning single atoms with a scanning tunnelling microscope, *Nature* **1990**, 344, 524-526.
- (7) Dresselhaus, M. S.; Dresselhaus, G.; Eklund, P. C. In *Science of fullerenes and carbon nanotubes: their properties and applications*; Academic press: **1996**.
- (8) Freestone, I.; Meeks, N.; Sax, M.; Higgitt, C. The Lycurgus cup—a roman nanotechnology *Gold Bull* **2007**, 40, 270-277.
- (9) Colomban, P. In *In The use of metal nanoparticles to produce yellow, red and iridescent colour, from bronze age to present times in lustre pottery and glass: solid state chemistry, spectroscopy and nanostructure*; Journal of Nano Research; Trans Tech Publ: 2009; Vol. 8, pp 109-132.
- (10) Anthony, F. In *Francisci Antonii... Panacea aurea: sive tractatus duo de ipsius auro potabili; ex Bibliopolio Frobeniano*.
- (11) Faraday, M. The Bakerian lecture: experimental relations of gold (and other metals) to light, *Philos T R Soc Lond* **1857**, 147, 145-181.
- (12) Hulla, J. E.; Sahu, S. C.; Hayes, A. W. Nanotechnology: History and future, *Hum. Exp. Toxicol.* **2015**, 34, 1318-1321.
- (13) Mie, G. Beiträge zur Optik trüber Medien, speziell kolloidaler Metallösungen, *Ann phys* **1908**, 330, 377-445.
- (14) Daniel, M.; Astruc, D. Gold nanoparticles: assembly, supramolecular chemistry, quantum-size-related properties, and applications toward biology, catalysis, and nanotechnology, *Chem. Rev.* **2004**, 104, 293-346.

- (15) Stark, W.; Stoessel, P.; Wohlleben, W.; Hafner, A. Industrial applications of nanoparticles, *Chem. Soc. Rev.* **2015**, *44*, 5793-5805.
- (16) Pankhurst, Q. A.; Connolly, J.; Jones, S.; Dobson, J. Applications of magnetic nanoparticles in biomedicine, *J. Phys. D* **2003**, *36*, R167-R181.
- (17) Salata, O. Applications of nanoparticles in biology and medicine, *J. Nanobiotechnology* **2004**, *2*, 3.
- (18) Freitas, R. A. What is nanomedicine?, *Nanomed Nanotechnol* **2005**, *1*, 2-9.
- (19) US government THE NATIONAL NANOTECHNOLOGY INITIATIVE Supplement to the President's 2016 Budget. http://www.nano.gov/sites/default/files/pub_resource/nni_fy16_budget_supplement.pdf.
- (20) Jain, K. Nanobiotechnology: applications, markets and companies, *Basel: Jain (Ed) PharmaBiotech Publications* **2007**.
- (21) Han, G.; Ghosh, P.; Rotello, V. M. Functionalized gold nanoparticles for drug delivery, *Nanomedicine* **2007**, *2*, 113-123.
- (22) Wang, F.; Wang, Y.; Dou, S.; Xiong, M.; Sun, T.; Wang, J. Doxorubicin-tethered responsive gold nanoparticles facilitate intracellular drug delivery for overcoming multidrug resistance in cancer cells, *Acs Nano* **2011**, *5*, 3679-3692.
- (23) Ghosh, P.; Han, G.; De, M.; Kim, C. K.; Rotello, V. M. Gold nanoparticles in delivery applications, *Adv. Drug Deliv. Rev.* **2008**, *60*, 1307-1315.
- (24) Gorjikhah, F.; Davaran, S.; Salehi, R.; Bakhtiari, M.; Hasanzadeh, A.; Panahi, Y.; Emamverdy, M.; Akbarzadeh, A. Improving "lab-on-a-chip" techniques using biomedical nanotechnology: a review, *Artificial cells, nanomedicine, and biotechnology* **2016**, 1-6.
- (25) Etheridge, M. L.; Campbell, S. A.; Erdman, A. G.; Haynes, C. L.; Wolf, S. M.; McCullough, J. The big picture on nanomedicine: the state of investigational and approved nanomedicine products, *Nanomed Nanotechnol* **2013**, *9*, 1-14.
- (26) American Cancer Society <https://cancerstatisticscenter.cancer.org/> (accessed 07/04, 2016).
- (27) Singhal, S.; Nie, S.; Wang, M. D. Nanotechnology applications in surgical oncology, *Annu. Rev. Med.* **2010**, *61*, 359-373.
- (28) Misra, R.; Acharya, S.; Sahoo, S. K. Cancer nanotechnology: application of nanotechnology in cancer therapy, *Drug Discov. Today* **2010**, *15*, 842-850.
- (29) Allen, T. M.; Cullis, P. R. Liposomal drug delivery systems: from concept to clinical applications, *Adv. Drug Deliv. Rev.* **2013**, *65*, 36-48.

- (30) Armelles, G.; Cebollada, A.; García-Martín, A.; González, M. U. Magnetoplasmonics: combining magnetic and plasmonic functionalities, *Adv Opt Mater* **2013**, *1*, 10-35.
- (31) Bertorelle, F.; Ceccarello, M.; Pinto, M.; Fracasso, G.; Badocco, D.; Amendola, V.; Pastore, P.; Colombatti, M.; Meneghetti, M. Efficient AuFeO_x Nanoclusters of Laser-Ablated Nanoparticles in Water for Cells Guiding and Surface-Enhanced Resonance Raman Scattering Imaging, *J Phys Chem C* **2014**, *118*, 14534-14541.
- (32) Brigger, I.; Dubernet, C.; Couvreur, P. Nanoparticles in cancer therapy and diagnosis, *Adv. Drug Deliv. Rev.* **2002**, *54*, 631-651.
- (33) Deng, C.; Jiang, Y.; Cheng, R.; Meng, F.; Zhong, Z. Biodegradable polymeric micelles for targeted and controlled anticancer drug delivery: promises, progress and prospects, *Nano Today* **2012**, *7*, 467-480.
- (34) Gong, J.; Chen, M.; Zheng, Y.; Wang, S.; Wang, Y. Polymeric micelles drug delivery system in oncology, *J. Control Release* **2012**, *159*, 312-323.
- (35) Kesharwani, P.; Jain, K.; Jain, N. K. Dendrimer as nanocarrier for drug delivery, *Prog Poly Sci* **2014**, *39*, 268-307.
- (36) Barizuddin, S.; Bok, S.; Gangopadhyay, S. Plasmonic Sensors for Disease Detection-A Review, *J Nanomed Nanotechnol* **2016**, *7*, 2.
- (37) Prato, M.; Kostarelos, K.; Bianco, A. Functionalized carbon nanotubes in drug design and discovery, *Acc. Chem. Res.* **2007**, *41*, 60-68.
- (38) Smith, A. M.; Dave, S.; Nie, S.; True, L.; Gao, X. Multicolor quantum dots for molecular diagnostics of cancer, *Expert Rev Mol Diagn* **2006**, *6*, 231-244.
- (39) Kim, J. S.; Kuk, E.; Yu, K. N.; Kim, J.; Park, S. J.; Lee, H. J.; Kim, S. H.; Park, Y. K.; Park, Y. H.; Hwang, C. Antimicrobial effects of silver nanoparticles, *Nanomed Nanotechnol*, **2007**, *3*, 95-101.
- (40) Shukla, R.; Bansal, V.; Chaudhary, M.; Basu, A.; Bhonde, R. R.; Sastry, M. Biocompatibility of gold nanoparticles and their endocytotic fate inside the cellular compartment: a microscopic overview, *Langmuir* **2005**, *21*, 10644-10654.
- (41) Khlebtsov, N.; Dykman, L. Biodistribution and toxicity of engineered gold nanoparticles: a review of in vitro and in vivo studies, *Chem. Soc. Rev.* **2011**, *40*, 1647-1671.
- (42) McNay, G.; Eustace, D.; Smith, W. E.; Faulds, K.; Graham, D. Surface-enhanced Raman scattering (SERS) and surface-enhanced resonance Raman

- scattering (SERRS): a review of applications, *Appl. Spectrosc.* **2011**, *65*, 825-837.
- (43) Murphy, C. J.; Gole, A. M.; Stone, J. W.; Sisco, P. N.; Alkilany, A. M.; Goldsmith, E. C.; Baxter, S. C. Gold nanoparticles in biology: beyond toxicity to cellular imaging, *Acc. Chem. Res.* **2008**, *41*, 1721-1730.
- (44) Boisselier, E.; Astruc, D. Gold nanoparticles in nanomedicine: preparations, imaging, diagnostics, therapies and toxicity, *Chem. Soc. Rev.* **2009**, *38*, 1759-1782.
- (45) Mura, S.; Nicolas, J.; Couvreur, P. Stimuli-responsive nanocarriers for drug delivery, *Nat mater* **2013**, *12*, 991-1003.
- (46) Sershen, S.; Westcott, S.; Halas, N.; West, J. Temperature-sensitive polymer–nanoshell composites for photothermally modulated drug delivery, *J. Biomed. Mater. Res.* **2000**, *51*, 293-298.
- (47) Laurent, S.; Forge, D.; Port, M.; Roch, A.; Robic, C.; Vander Elst, L.; Muller, R. N. Magnetic iron oxide nanoparticles: synthesis, stabilization, vectorization, physicochemical characterizations, and biological applications, *Chem. Rev.* **2008**, *108*, 2064-2110.
- (48) Li, X.; Wei, J.; Aifantis, K. E.; Fan, Y.; Feng, Q.; Cui, F.; Watari, F. Current investigations into magnetic nanoparticles for biomedical applications, *J Biomed Mater Res A* **2016**, .
- (49) Grootendorst, D. J.; Jose, J.; Fratila, R. M.; Visscher, M.; Velders, A. H.; Ten Haken, B.; Van Leeuwen, T. G.; Steenbergen, W.; Manohar, S.; Ruers, T. J. Evaluation of superparamagnetic iron oxide nanoparticles (Endorem®) as a photoacoustic contrast agent for intra-operative nodal staging *Contrast media mol i* **2013**, *8*, 83-91.
- (50) Zborowski, M.; Chalmers, J. J. Rare cell separation and analysis by magnetic sorting, *Anal. Chem.* **2011**, *83*, 8050-8056.
- (51) Paterlini-Brechot, P.; Benali, N. L. Circulating tumor cells (CTC) detection: clinical impact and future directions, *Cancer Lett.* **2007**, *253*, 180-204.
- (52) Liberti, P. A.; Rao, C. G.; Terstappen, L. W. Optimization of ferrofluids and protocols for the enrichment of breast tumor cells in blood, *J Magn Magn Mater* **2001**, *225*, 301-307.
- (53) McCloskey, K. E.; Chalmers, J. J.; Zborowski, M. Magnetic cell separation: characterization of magnetophoretic mobility, *Anal. Chem.* **2003**, *75*, 6868-6874.

- (54) Hilger, I.; Hiergeist, R.; Hergt, R.; Winnefeld, K.; Schubert, H.; Kaiser, W. A. Thermal ablation of tumors using magnetic nanoparticles: an in vivo feasibility study, *Invest. Radiol.* **2002**, *37*, 580-586.
- (55) González-Díaz, J. B.; García-Martín, A.; García-Martín, J. M.; Cebollada, A.; Armelles, G.; Sepúlveda, B.; Alaverdyan, Y.; Käll, M. Plasmonic Au/Co/Au Nanosandwiches with Enhanced Magneto-optical Activity, *Small* **2008**, *4*, 202-205.
- (56) Armelles, G.; Cebollada, A.; García-Martín, A.; Montero-Moreno, J.; Waleczek, M.; Nielsch, K. Magneto-optical Properties of Core-Shell Magneto-plasmonic Au-Co_xFe_{3-x}O₄ Nanowires, *Langmuir* **2012**, *28*, 9127-9130.
- (57) Urries, I.; Muñoz, C.; Gomez, L.; Marquina, C.; Sebastian, V.; Arruebo, M.; Santamaria, J. Magneto-plasmonic nanoparticles as theranostic platforms for magnetic resonance imaging, drug delivery and NIR hyperthermia applications, *Nanoscale* **2014**, *6*, 9230-9240.
- (58) Amendola, V.; Scaramuzza, S.; Litti, L.; Meneghetti, M.; Zuccolotto, G.; Rosato, A.; Nicolato, E.; Marzola, P.; Fracasso, G.; Anselmi, C. Magneto-Plasmonic Au-Fe Alloy Nanoparticles Designed for Multimodal SERS-MRI-CT Imaging, *Small* **2014**, *10*, 2476-2486.
- (59) Bao, J.; Chen, W.; Liu, T.; Zhu, Y.; Jin, P.; Wang, L.; Liu, J.; Wei, Y.; Li, Y. Bifunctional Au-Fe₃O₄ nanoparticles for protein separation, *Acs Nano* **2007**, *1*, 293-298.
- (60) Bao, F.; Yao, J.; Gu, R. Synthesis of magnetic Fe₂O₃/Au core/shell nanoparticles for bioseparation and immunoassay based on surface-enhanced Raman spectroscopy, *Langmuir* **2009**, *25*, 10782-10787.
- (61) Espinosa, A.; Bugnet, M.; Radtke, G.; Neveu, S.; Botton, G. A.; Wilhelm, C.; Abou-Hassan, A. Can magneto-plasmonic nanohybrids efficiently combine photothermia with magnetic hyperthermia?, *Nanoscale* **2015**, *7*, 18872-18877.
- (62) Kim, J.; Park, S.; Lee, J. E.; Jin, S. M.; Lee, J. H.; Lee, I. S.; Yang, I.; Kim, J.; Kim, S. K.; Cho, M. Designed fabrication of multifunctional magnetic gold nanoshells and their application to magnetic resonance imaging and photothermal therapy *Angew Chem Int Edit* **2006**, *45*, 7754-7758.
- (63) Jin, Y. Multifunctional Compact Hybrid Au Nanoshells: A New Generation of Nanoplasmonic Probes for Biosensing, Imaging, and Controlled Release, *Acc. Chem. Res.* **2013**, *47* (1), 138-148.
- (64) Mieszawska, A. J.; Mulder, W. J.; Fayad, Z. A.; Cormode, D. P. Multifunctional gold nanoparticles for diagnosis and therapy of disease, *Mol pharm* **2013**, *10*, 831-847.

- (65) McCarthy, J. R.; Weissleder, R. Multifunctional magnetic nanoparticles for targeted imaging and therapy, *Adv. Drug Deliv. Rev.* **2008**, *60*, 1241-1251.
- (66) Sung, Y. J.; Suk, H.; Sung, H. Y.; Li, T.; Poo, H.; Kim, M. Novel antibody/gold nanoparticle/magnetic nanoparticle nanocomposites for immunomagnetic separation and rapid colorimetric detection of *Staphylococcus aureus* in milk, *Biosens Bioelectron* **2013**, *43*, 432-439.
- (67) Sotiriou, G. A.; Starsich, F.; Dasargyri, A.; Wurnig, M. C.; Krumeich, F.; Boss, A.; Leroux, J.; Pratsinis, S. E. Photothermal killing of cancer cells by the controlled plasmonic coupling of silica-coated Au/Fe₂O₃ nanoaggregates, *Adv Funct Mater* **2014**, *24*, 2818-2827.
- (68) Fan, Z.; Shelton, M.; Singh, A. K.; Senapati, D.; Khan, S. A.; Ray, P. C. Multifunctional plasmonic shell–magnetic core nanoparticles for targeted diagnostics, isolation, and photothermal destruction of tumor cells, *ACS nano* **2012**, *6*, 1065-1073.
- (69) Dai, X.; Fan, Z.; Lu, Y.; Ray, P. C. Multifunctional nanoplatfoms for targeted multidrug-resistant-bacteria theranostic applications, *ACS appl mater int*, **2013**, *5*, 11348-11354.
- (70) Kuroda, S.; Tam, J.; Roth, J. A.; Sokolov, K.; Ramesh, R. EGFR-targeted plasmonic magnetic nanoparticles suppress lung tumor growth by abrogating G2/M cell-cycle arrest and inducing DNA damage, *Int. J. Nanomedicine* **2014**, *9*, 3825-3839.
- (71) Demeritte, T.; Viraka Nellore, B. P.; Kanchanapally, R.; Sinha, S. S.; Pramanik, A.; Chavva, S. R.; Ray, P. C. Hybrid Graphene Oxide Based Plasmonic-Magnetic Multifunctional Nanoplatform for Selective Separation and Label-Free Identification of Alzheimer’s Disease Biomarkers, *ACS appl mater int*, **2015**, *7*, 13693-13700.
- (72) Gabriel, J. A. In *The biology of cancer*; John Wiley & Sons: **2007**.
- (73) Knowles, M. In *Introduction to the cellular and molecular biology of cancer*; Oxford university press: **2005**.
- (74) Wikipedia Antibody. <https://en.wikipedia.org/wiki/Antibody> (accessed 07/15, 2016).
- (75) Abbas, A. K.; Lichtman, A. H. In *Immunologia: funzioni e alterazioni del sistema immunitario*; Piccin: **1994**.
- (76) Cauchi, C. Saracino b, Lopez m, bonadonna G, Carcinoma della prostata, *Lopez m, Oncologia Medica Pratica.Società editrice Universo, Roma, iii edizione* **2010**, , 1985-2015.

- (77) Ferlay, J.; Steliarova-Foucher, E.; Lortet-Tieulent, J.; Rosso, S.; Coebergh, J.; Comber, H.; Forman, D.; Bray, F. Cancer incidence and mortality patterns in Europe: estimates for 40 countries in 2012, *Eur. J. Cancer* **2013**, *49*, 1374-1403.
- (78) Sanchez, F.; Sobolev, K. Nanotechnology in concrete—a review, *Constr. Build. Mater.* **2010**, *24*, 2060-2071.
- (79) Kelsall, R. W.; Hamley, I. W.; Geoghegan, M. In *Nanoscale science and technology*; Wiley Online Library: 2005; .
- (80) Perrault, S. D.; Chan, W. C. Synthesis and surface modification of highly monodispersed, spherical gold nanoparticles of 50– 200 nm, *J. Am. Chem. Soc.* **2009**, *131*, 17042-17043.
- (81) Martin, M. N.; Basham, J. I.; Chando, P.; Eah, S. Charged gold nanoparticles in non-polar solvents: 10-min synthesis and 2D self-assembly, *Langmuir* **2010**, *26*, 7410-7417.
- (82) Navarro, J. R.; Lerouge, F.; Cepraga, C.; Micouin, G.; Favier, A.; Chateau, D.; Charreyre, M.; Lanoë, P.; Monnereau, C.; Chaput, F. Nanocarriers with ultrahigh chromophore loading for fluorescence bio-imaging and photodynamic therapy, *Biomaterials* **2013**, *34*, 8344-8351.
- (83) Zhou, Y.; Wang, C.; Zhu, Y.; Chen, Z. A novel ultraviolet irradiation technique for shape-controlled synthesis of gold nanoparticles at room temperature, *Chem mater* **1999**, *11*, 2310-2312.
- (84) Niidome, Y.; Hori, A.; Sato, T.; Yamada, S. Enormous Size Growth of Thiol-passivated Gold Nanoparticles Induced by Near-IR Laser Light, *Chem. Lett.* **2000**, , 310-311.
- (85) Shen, M.; Du, Y.; Hua, N.; Yang, P. Microwave irradiation synthesis and self-assembly of alkylamine-stabilized gold nanoparticles, *Powder Technol* **2006**, *162*, 64-72.
- (86) Okitsu, K.; Yue, A.; Tanabe, S.; Matsumoto, H.; Yobiko, Y.; Yoo, Y. Sonolytic Control of Rate of Gold (III) Reduction and Size of Formed Gold Nanoparticles: Relation between Reduction Rates and Sizes of Formed Nanoparticles. *Bull. Chem. Soc. Jpn.* **2002**, *75*, 2289-2296.
- (87) Pol, V.; Gedanken, A.; Calderon-Moreno, J. Deposition of gold nanoparticles on silica spheres: a sonochemical approach, *Chem mater* **2003**, *15*, 1111-1118.
- (88) Hutter, E.; Fendler, J. H. Exploitation of localized surface plasmon resonance, *Adv Mater* **2004**, *16*, 1685-1706.

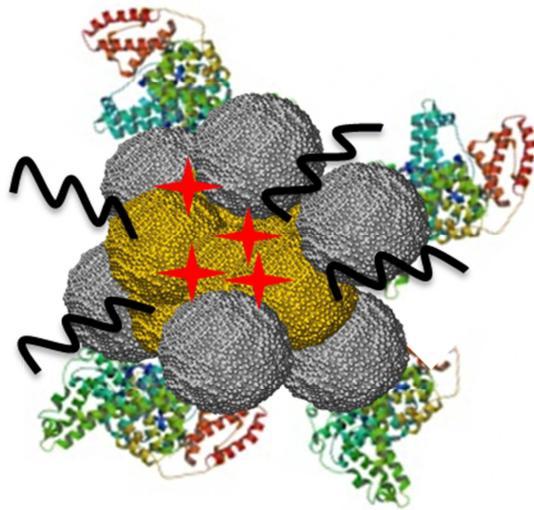
- (89) Ghosh, S. K.; Pal, T. Interparticle coupling effect on the surface plasmon resonance of gold nanoparticles: from theory to applications, *Chem. Rev.* **2007**, *107*, 4797-4862.
- (90) Amendola, V.; Meneghetti, M. Size Evaluation of Gold Nanoparticles by UV-vis Spectroscopy, *J Phys Chem C* **2009**, *113*, 4277-4285.
- (91) Stiles, P. L.; Dieringer, J. A.; Shah, N. C.; Van Duyne, R. P. Surface-enhanced Raman spectroscopy, *Annu.Rev.Anal.Chem.* **2008**, *1*, 601-626.
- (92) Kneipp, K.; Moskovits, M.; Kneipp, H. Surface-enhanced Raman scattering, *Phys Today* **2007**, *60*, 40.
- (93) Campion, A.; Kambhampati, P. Surface-enhanced Raman scattering, *Chem. Soc. Rev.* **1998**, *27*, 241-250.
- (94) Thomas, K. G.; Kamat, P. V. Chromophore-functionalized gold nanoparticles, *Acc. Chem. Res.* **2003**, *36*, 888-898.
- (95) Moskovits, M. Surface-enhanced Raman spectroscopy: a brief retrospective, *J. Raman Spectrosc.* **2005**, *36*, 485-496.
- (96) Haynes, C. L.; McFarland, A. D.; Duyne, R. P. V. Surface-enhanced Raman spectroscopy, *Anal. Chem.* **2005**, *77*, 338 A-346 A.
- (97) Amendola, V.; Meneghetti, M. Exploring How to Increase the Brightness of Surface-Enhanced Raman Spectroscopy Nanolabels: The Effect of the Raman-Active Molecules and of the Label Size, *Adv Funct Mater* **2012**, *22*, 353-360.
- (98) Brongersma, M. L.; Halas, N. J.; Nordlander, P. Plasmon-induced hot carrier science and technology, *Nat nanotechnol* **2015**, *10*, 25-34.
- (99) Huang, X.; El-Sayed, M. A. Plasmonic photo-thermal therapy (PPTT), *Alexandria Journal of Medicine* **2011**, *47*, 1-9.
- (100) Huang, X.; Jain, P. K.; El-Sayed, I. H.; El-Sayed, M. A. Plasmonic photothermal therapy (PPTT) using gold nanoparticles, *Laser med sci*, **2008**, *23*, 217-228.
- (101) Kennedy, L. C.; Bickford, L. R.; Lewinski, N. A.; Coughlin, A. J.; Hu, Y.; Day, E. S.; West, J. L.; Drezek, R. A. A New Era for Cancer Treatment: Gold-Nanoparticle-Mediated Thermal Therapies, *Small* **2011**, *7*, 169-183.
- (102) Neumann, O.; Neumann, A. D.; Silva, E.; Ayala-Orozco, C.; Tian, S.; Nordlander, P.; Halas, N. J. Nanoparticle-Mediated, Light-Induced Phase Separations, *Nano lett*, **2015**, *15*, 7880-7885.

- (103) Wu, W.; Wu, Z.; Yu, T.; Jiang, C.; Kim, W. Recent progress on magnetic iron oxide nanoparticles: synthesis, surface functional strategies and biomedical applications, *Sci Technol Adv Mat*, **2016**, *16*, 023501 .
- (104) Teja, A. S.; Koh, P. Synthesis, properties, and applications of magnetic iron oxide nanoparticles, *Prog Cryst Growth Ch*, **2009**, *55*, 22-45.
- (105) Mahmoudi, M.; Sant, S.; Wang, B.; Laurent, S.; Sen, T. Superparamagnetic iron oxide nanoparticles (SPIONs): development, surface modification and applications in chemotherapy, *Adv. Drug Deliv. Rev.* **2011**, *63*, 24-46.
- (106) Wu, W.; He, Q.; Jiang, C. Magnetic iron oxide nanoparticles: synthesis and surface functionalization strategies, *Nanoscale Res Lett*, **2008**, *3*, 397.
- (107) Stöber, W.; Fink, A.; Bohn, E. Controlled growth of monodisperse silica spheres in the micron size range, *J. Colloid Interface Sci.* **1968**, *26*, 62-69.
- (108) Montalti, M.; Prodi, L.; Rampazzo, E.; Zaccheroni, N. Dye-doped silica nanoparticles as luminescent organized systems for nanomedicine, *Chem. Soc. Rev.* **2014**, *43*, 4243-4268.
- (109) Wang, H.; Brandl, D. W.; Le, F.; Nordlander, P.; Halas, N. J. Nanorice: a hybrid plasmonic nanostructure, *Nano lett* **2006**, *6*, 827-832.
- (110) Bardhan, R.; Chen, W.; Perez-Torres, C.; Bartels, M.; Huschka, R. M.; Zhao, L. L.; Morosan, E.; Pautler, R. G.; Joshi, A.; Halas, N. J. Nanoshells with targeted simultaneous enhancement of magnetic and optical imaging and photothermal therapeutic response, *Adv Funct Mater* **2009**, *19*, 3901-3909.
- (111) Leung, K. C.; Xuan, S.; Zhu, X.; Wang, D.; Chak, C.; Lee, S.; Ho, W. K.; Chung, B. C. Gold and iron oxide hybrid nanocomposite materials, *Chem. Soc. Rev.* **2012**, *41*, 1911-1928.
- (112) Westcott, S. L.; Oldenburg, S. J.; Lee, T. R.; Halas, N. J. Formation and adsorption of clusters of gold nanoparticles onto functionalized silica nanoparticle surfaces, *Langmuir* **1998**, *14*, 5396-5401.
- (113) La Porta, A.; Sánchez-Iglesias, A.; Altantzis, T.; Bals, S.; Grzelczak, M.; Liz-Marzán, L. M. Multifunctional self-assembled composite colloids and their application to SERS detection, *Nanoscale* **2015**, *7*, 10377-10381.
- (114) Chandran, S. P.; Chaudhary, M.; Pasricha, R.; Ahmad, A.; Sastry, M. Synthesis of gold nanotriangles and silver nanoparticles using Alovera plant extract, *Biotechnol. Prog.* **2006**, *22*, 577-583.
- (115) Huang, J.; Li, Q.; Sun, D.; Lu, Y.; Su, Y.; Yang, X.; Wang, H.; Wang, Y.; Shao, W.; He, N. Biosynthesis of silver and gold nanoparticles by novel sundried Cinnamomum camphora leaf, *Nanotechnology* **2007**, *18*, 105104.

- (116) Aromal, S. A.; Philip, D. Green synthesis of gold nanoparticles using *Trigonella foenum-graecum* and its size-dependent catalytic activity, *Spectrochimica Acta A*, **2012**, *97*, 1-5.
- (117) Mukherjee, P.; Ahmad, A.; Mandal, D.; Senapati, S.; Sainkar, S. R.; Khan, M. I.; Ramani, R.; Parischa, R.; Ajayakumar, P.; Alam, M. Bioreduction of AuCl₄⁻ ions by the fungus, *Verticillium* sp. and surface trapping of the gold nanoparticles formed, *Angew Chem Int Edit* **2001**, *40*, 3585-3588.
- (118) Husseiny, M.; El-Aziz, M. A.; Badr, Y.; Mahmoud, M. Biosynthesis of gold nanoparticles using *Pseudomonas aeruginosa*, *Spectrochimica Acta A*, **2007**, *67*, 1003-1006.
- (119) He, S.; Guo, Z.; Zhang, Y.; Zhang, S.; Wang, J.; Gu, N. Biosynthesis of gold nanoparticles using the bacteria *Rhodopseudomonas capsulate*, *Mater Lett* **2007**, *61*, 3984-3987.
- (120) Kumar, V.; Yadav, S. K. Plant-mediated synthesis of silver and gold nanoparticles and their applications, *J Chem Technol Biot*, **2009**, *84*, 151-157.
- (121) Narayanan, K. B.; Sakthivel, N. Biological synthesis of metal nanoparticles by microbes, *Adv. Colloid Interface Sci.* **2010**, *156*, 1-13.
- (122) Bharde, A.; Rautaray, D.; Bansal, V.; Ahmad, A.; Sarkar, I.; Yusuf, S. M.; Sanyal, M.; Sastry, M. Extracellular biosynthesis of magnetite using fungi, *Small* **2006**, *2*, 135-141.
- (123) Amendola, V.; Meneghetti, M. What controls the composition and the structure of nanomaterials generated by laser ablation in liquid solution?, *Phys Chem Chem Phys*, **2013**, *15*, 3027-3046.
- (124) Amendola, V.; Meneghetti, M. Controlled size manipulation of free gold nanoparticles by laser irradiation and their facile bioconjugation, *J Mater Chem*, **2007**, *17*, 4705-4710.
- (125) Amendola, V.; Meneghetti, M. Laser ablation synthesis in solution and size manipulation of noble metal nanoparticles, *Phys Chem Chem Phys*, **2009**, *11*, 3805-3821.
- (126) Amendola, V.; Polizzi, S.; Meneghetti, M. Laser ablation synthesis of gold nanoparticles in organic solvents, *J Phys Chem B*, **2006**, *110*, 7232-7237.
- (127) Amendola, V.; Riello, P.; Polizzi, S.; Fiameni, S.; Innocenti, C.; Sangregorio, C.; Meneghetti, M. Magnetic iron oxide nanoparticles with tunable size and free surface obtained via a “green” approach based on laser irradiation in water, *J Mater Chem*, **2011**, *21*, 18665-18673.

- (128) Amendola, V.; Meneghetti, M.; Granozzi, G.; Agnoli, S.; Polizzi, S.; Riello, P.; Boscaini, A.; Anselmi, C.; Fracasso, G.; Colombatti, M. Top-down synthesis of multifunctional iron oxide nanoparticles for macrophage labelling and manipulation, *J Mater Chem*, **2011**, *21*, 3803-3813.
- (129) Particular GmbH Particular, customized material.
<http://particular.eu/start.html> (accessed 09/07, 2016).
- (130) Streubel, R.; Barcikowski, S.; Gökce, B. Continuous multigram nanoparticle synthesis by high-power, high-repetition-rate ultrafast laser ablation in liquids, *Opt. Lett.* **2016**, *41*, 1486-1489.

Chapter 2



Gold and iron oxide nanoparticles aggregates for cell guiding and sorting

In this chapter the synthesis of magneto-plasmonic aggregates and their application in cell guiding and sorting is presented. These aggregates show both plasmonic and magnetic properties and are obtained combining in a single nanostructure gold and iron oxide nanoparticles.

AuNPs and FeO_xNPs are combined in a single nanocluster (AuFeO_xNC) without using any condensing material but only thanks to their native surface charges.

Both gold and iron oxide nanoparticles are first separately synthesized by laser ablation synthesis in solution. The process itself, as explained in the introduction, produces charged nanoparticles. These surface charges are also responsible for the stabilization of the colloidal solution.

After synthesis, aggregation of gold nanoparticles is obtained with centrifugation method. This is an important step because aggregation leads to the formation of hot spots, useful for SERS. Moreover, the absence of molecules on NPs surface enhances the possibility of having reporter molecules in hot spots and therefore larger SERS signals are obtained. Aggregation between AuNPs and FeO_xNPs is controlled by mixing the two solutions at appropriate pH. In fact, it should be recalled that pH have influence on the surface charges of nanoparticles.

In this step, varying the proportions between gold and iron oxide nanoparticles, one can enhance preferentially plasmonic or magnetic properties of AuFeO_xNC and this is useful for different applications for which the nanostructures can be designed.

The nanoclusters described in this chapter have been optimized for SERRS imaging of macrophage cells and macrophage guiding with a magnetic field.

Macrophage cells will be used to show that superparamagnetic properties of AuFeO_xNC are useful for their sorting when they are mixed with other cells. On the other side, plasmonic properties are useful for macrophage identification with SERRS effect.

Macrophage cells are of great interest in nanomedicine^{1, 2} because they can migrate into tumor lesions. The possibility of guiding them with a magnetic field and to detect their presence with SERRS spectroscopy allows to exploit them as a “Trojan

horse”. In this way, AuFeO_xNC can be delivered at tumor site, to improve tumor detection, and to apply hyperthermia therapy.

Synthesis of AuFeO_x nanoclusters

Synthesis of gold and iron oxide nanoparticles via Laser Ablation

Gold and iron oxide nanoparticles are separately synthesized with laser ablation synthesis in solution. LASiS is obtained by simply focusing laser pulses (6 ns, 50 Hz, 1064 nm) of a Nd:YAG (Quantel Brilliant 50) on a pure (99,999%) gold or iron plate under water at room temperature and pressure.

Pulses with a fluence of 1.2 J cm⁻² are used to obtain gold nanoparticles in a dilute NaCl (10⁻⁵ M) solution in double distilled (dd) water. Sodium chloride stabilizes the colloidal solution (see also subchapter “The importance of being pure: Laser Ablation Synthesis in solution” in introduction), but it is also one of the components most present in biological environments.

For iron oxide nanoparticles, fluences of 1.5 J cm⁻² were used and the synthesis is performed in pure dd water.

As discussed previously on the introduction, iron oxide nanoparticles obtained with LASiS possess a small fraction of amorphous hydroxides. The amorphous fraction is removed in a post-synthesis phase using a procedure developed in the hosting laboratory.³ HCl was added to a 0.024 M final concentration and then the solution was heated at 60° C for 60 minutes under constant stirring and then stored. The acidic pH of the solution was neutralized in a second moment during the assembling with AuNPs (see below), using NaOH. Total iron concentration was determined using o-phenanthroline method.⁴ Briefly, iron oxide nanoparticles (0.5 mL) are dissolved with 2.5 μL of concentrated H₂SO₄ at 90°C for 1h. Then pH is adjusted at about 4.5 with NaOH 0.03 M and 1 mL of acetic acid/sodium acetate buffer (pH 4.5) is added. 50 μL of 0.1 g mL⁻¹ hydroxylamine hydrochloride are added to reduce Fe(III) to Fe(II). After 10 minutes, 250 μL of a 1 mg mL⁻¹ of o-phenanthroline solution and acetic acid/sodium acetate buffer solution are added to a final volume of 5 mL. Absorbance at 510 nm gives the amount of Fe (II) using (NH₄)₂Fe(SO₄)₂•6H₂O (Mohr’s Salt) for the calibration curve. An approximate concentration of iron oxide nanoparticles is calculated using magnetite bulk density

(hematite has a very similar density), and FeO_xNP mean diameter obtained by TEM images.

AuNPs size and concentration in the colloidal solution are determined by fitting their UV-Vis spectra with a software developed in the hosting research group.⁵

Au molar concentration can be calculated using AuNPs average diameter obtained from the fitting and the density of the bulk material.

Assembling of the nanostructures and their labeling with a SERS reporter

AuNPs and FeO_xNPs nanoclusters were obtained with different Au and Fe concentrations. Those useful for experiments with cells, reported here, are those with 1:3.5 molar concentrations of Au and Fe.

The assembling was performed using a gold nanoparticle solution with an AuNPs concentration of $2.9 \cdot 10^{-9}$ M and Au concentration of $7.4 \cdot 10^{-2}$ mg mL⁻¹, and a FeO_xNPs solution with a Fe concentration of $6.25 \cdot 10^{-2}$ mg mL⁻¹ corresponding to a FeO_xNPs concentration of $2.5 \cdot 10^{-9}$ M. Molar concentration of Fe has been determined with *o*-phenanthroline method and confirmed with ICP-MS measurements while nanoparticles concentration has been calculated considering FeO_xNPs with a particle size distribution like the one in figure 2.1 D, obtained from TEM analysis of nanoparticles.

Before proceeding with the assembling of nanoparticles, AuNPs were aggregated with centrifugation method in order to form the hot spots between particles. AuNPs were mixed with a solution of NaOH (0.01 M) in the proportions of 1:1.5 (v/v) respectively and then centrifuged at 12100 *g* for 20 minutes. Supernatant were removed and particles were suspended in dd water. To complete the aggregation, another centrifugation cycle was performed at 12100 *g* for 20 minutes and then, after supernatant removal, nanoparticles aggregates were suspended in dd H₂O.

SERRS labeling of aggregated AuNPs was performed using thiol-functionalized Texas Red (TR-SH) as SERRS reporter.⁶ 800 μL of a 36 μM solution of the dye were added to gold nanoparticles aggregates. After 1h, AuNPs were centrifuged and supernatant was removed and replaced with dd H₂O.

AuFeO_xNC were assembled adding dropwise FeO_xNPs at pH=2 to functionalized AuNPs aggregates at pH=12 until neutral pH was restored.

Chapter 2

In this solution, NaCl is present but it is present also in the solution that will be used for incubation with macrophages. After 1h, particles were centrifuged, supernatant was removed and AuFeO_xNC were suspended in dd H₂O.

AuFeO_xNC were stabilized adding bovine serum albumin (BSA) at a concentration of 2.7 mg mL⁻¹. Beside stabilizing gold and iron nanoclusters, BSA is also a component for the incubation with macrophages.

AuFeO_xNC were left at rest for one night and then centrifuged (12100 g, 20 min) and dispersed in bidistilled water.

Functionalization with methoxy polyethylene glycol thiol 5000 Da (mPEG-SH), which is used to give stealth properties to nanoparticles, was performed adding a 1.1 mg mL⁻¹ solution of the polymer to AuFeO_xNC solution.

After 3h the solution was centrifuges, supernatant was removed and AuFeO_xNC were dispersed in dd H₂O.

Macrophage labeling and sorting

Experiments with macrophages were performed incubating RAW 264.7 macrophage cells for 24h with a solution of AuFeO_xNC at a final concentration of Fe, in the wells, of 0.18 mg ml⁻¹. We verified that this incubation time and concentration allow us to perform a complete sorting in less than 10 minutes.

After incubation time, cells were washed multiple times with phosphate buffer saline (PBS) solution to remove nanoclusters in excess and then collected in a vial with PBS.

The magnetic cell sorting was performed in 10 minutes placing the vial in contact with a commercial magnetic particle concentrator (DynaL MPC-L, Invitrogen).

Sorted cells were separated from unsorted ones and then both were deposited in two different polylysinate slides for 1h. For cell fixation, a 4% paraformaldehyde solution was added and, after 30 minutes, all slides were washed with PBS and dried.

Instrumentation

UV-vis spectra of the preparation were registered in a 2 mm quartz cuvette using a Varian Cary 5000 UV-vis-NIR spectrophotometer. For micro-Raman measurement we used a Renishaw inVia micro-Raman instrument with a 20× objective and the 633 nm line of a He-Ne laser with an output power of 1.54 mW. SERS spectra in solution are recorded in a 2 mm quartz cuvette using a 5x objective and a He-Ne

laser with a power, on the cuvette, of 1.5 mW. DLS and Z spectroscopy were performed with a Malvern Nano ZS instrument equipped with a 633 nm He–Ne Laser. For transmission electron microscopy (TEM) we recorded the images at 100 kV with a FEI TECNAI G2 microscope. The samples for TEM analysis were prepared by evaporating AuFeO_xNC suspension mixed with a solution of PVA, to avoid aggregation during evaporation of the solution, on a copper grid covered with a holey amorphous carbon film. Metal concentrations of the final preparation were also determined by ICP-MS measurements performed with an Agilent Technologies 7700x ICP-MS. Calibration solutions were prepared by gravimetric serial dilution from multielement standard solutions at suitable concentrations. Microwave acidic digestion was operated according to EPA 305 B protocol for nanoparticles^{7,8} with a CEM EXPLORER SP-D PLUS. Flow cytometry was performed using a BD FACSCanto flow cytometer.

Results

Synthesis of gold and iron oxide nanoparticles

The colloidal solutions of gold and iron oxide nanoparticles are stable thanks to surface charges arising from the ablation process itself.^{3,9-11}

FeO_xNPs produced by LASiS are mainly composed of magnetite, with minor fraction of hematite, wustite and amorphous materials.^{3, 10} They show good superparamagnetic behavior (Figure 2.1 B) and a mean diameter of 25±11 nm (Figure 2.1 C) with a typical distribution showed in figure 2.1 D. Z-potential measurements show values of about +40 mV in acidic solutions, which determines good stability of these nanoparticles.

Typical UV-Vis spectra of laser ablated AuNPs is reported in figure 2.1 F and show a surface plasmon resonance located at 520 nm. Fitting of this spectrum with the Mie-Gans theory provides mean diameter, concentration and sphericity of synthesized AuNPs.⁵ In the case of the spectra in figure 2.1 F, one obtains an AuNP concentration of 5.2·10⁻⁹ M with 70% sphericity and a mean diameter of about 20 nm, which is in good agreement with TEM images of AuNPs (figure 2.1E). Z-potential measurement performed on laser ablated gold nanoparticles show values of more than -30 mV, which guarantees their stability in solution.

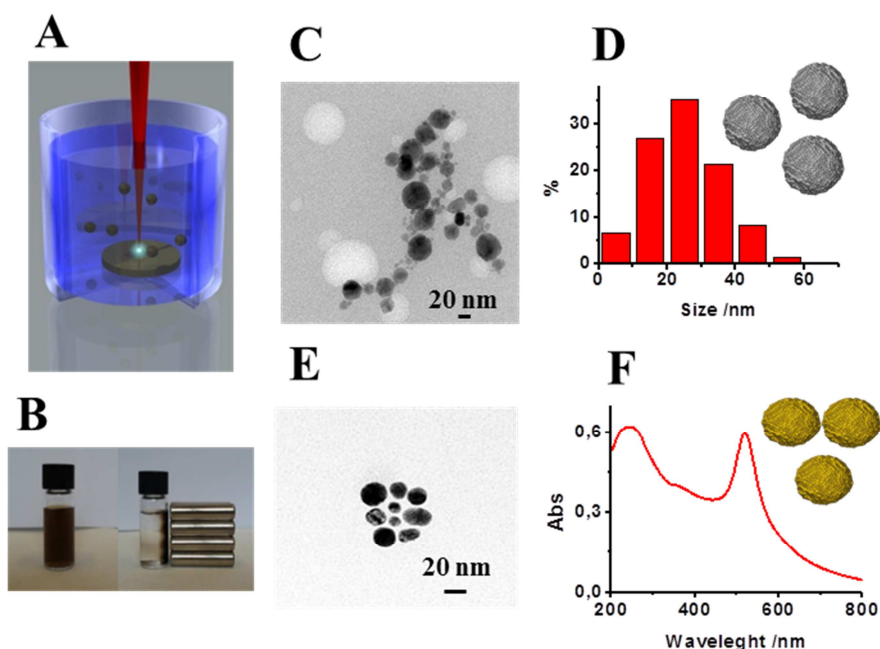


Figure 2.1 (A) Cartoon representing Laser Ablation Synthesis in Solution. (B) Magnetic response of FeO_xNPs with a permanent magnet. (C) TEM image of FeO_xNPs synthesized with LASiS (D) size distribution of FeO_xNPs from TEM analysis. (E) TEM image of AuNP synthesized with LASiS. (F) Absorption spectrum of AuNP with LSPR located at 520 nm.

Synthesis and characterization of AuFeO_x nanoclusters

Aggregation of AuNPs by a controlled centrifugation creates the so called hot spots, namely, structures in which the electromagnetic field is enhanced. Molecules within hot spots show SERS activity.

Although LASiS generated AuNPs repel each other thanks to high negative surface charges, the high g values generated by the centrifuge are able to overcome electrostatic repulsive forces until Van der Waals attractive forces prevails, according to DLVO theory.¹²

Besides gold nanoparticles aggregation, SERS performance of the nanostructures is improved using a SERS reporter which is in resonance with the laser excitation (we used in particular the laser line with wavelength at 633 nm), so these aggregates are optimized for SERRS.

The SERRS reporter used in this work, Texas Red, is functionalized with a thiol group (TR-SH, figure 2.2 c and d), which quickly binds to the surface of gold nanoparticles. AuNPs aggregates functionalized with TR-SH give high SERRS signals (figure 2.2 e). In figure 2.2 a, TEM image of a gold nanoparticles aggregate is

reported. The aggregates consist of 10-20 AuNPs with an overall size of about 60-100 nm. The UV-Vis-NIR spectra (figure 1b) show the typical two characteristic plasmonic peaks of aggregated gold nanostructures with one plasmon at about 520 nm, and a broader one at 650-750 nm.

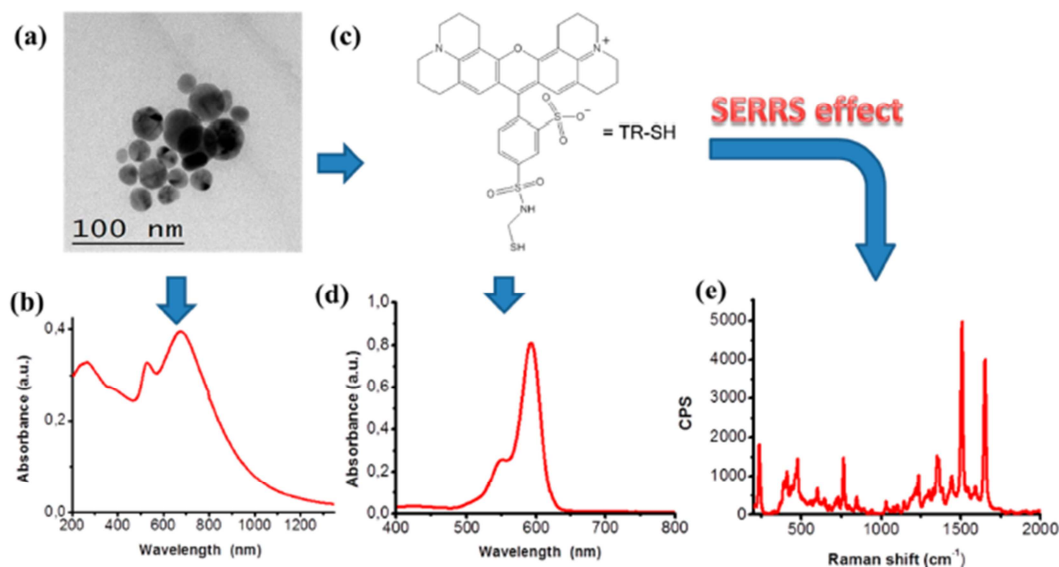


Figure 2.2 AuNPs aggregates functionalized with TR-SH: (a) TEM image of gold nanoparticle aggregates and (b) their UV-Visible-NIR spectrum. (c) Thiolated Texas Red used for functionalization of AuNPs and (d) its UV-Visible spectrum of a 36 μM solution. (e) SERRS spectra of labeled AuNPs aggregates.¹³

Gold and iron oxide nanoparticles show Z-potential of opposite sign and the electrostatic interactions between the two types of particles drives the formation of AuFeO_xNC . Nanoclusters can be obtained simply by mixing the two solutions.

Varying molar proportions between the two nanoparticles, one can enhance either magnetic or plasmonic properties. We found that to obtain both good SERRS signals and magnetic properties, Au:Fe molar ratio must be between 1:1 and 1:3.5.

In this work we consider aggregates with Au:Fe molar ratio of 1:3.5.

Before mixing the two solution, NaOH at a pH=12 is added to gold nanoparticles aggregates. The amount of NaOH added is necessary to neutralize the acidic pH of iron oxide nanoparticles solution. One hour after mixing, the synthesized AuFeO_xNC were washed and concentrated by centrifugation.

Z-potential measurement performed on AuFeO_xNC show values of about -5 mV, which is in agreement with the neutralization of AuNPs and FeO_xNPs charges. With such small Z-potential, nanoclusters rapidly flocculate, but the phenomenon is reversible with a weak sonication.

Dynamic light scattering (DLS) measurements performed on AuFeO_xNC show aggregates with average size of 150-200 nm.

Due to the low Z-potential, these nanostructures need to be stabilized. For this purpose we used bovine serum albumin (BSA), because coating of the NPs surface with an inert protein like BSA, also used in following incubation with cells, helps to reduce the aggregation process significantly.^{14, 15}

After BSA addition, the solution is stored overnight. The next day, AuFeO_xNC are centrifuged to remove protein in excess and suspended in PBS solution. In the last step one also add mPEG-SH, which saturates all available free sites, if present, on gold nanoparticles. The preparation is stable for months.

The whole procedure for the synthesis of AuFeO_xNC is sketched in figure 2.3.

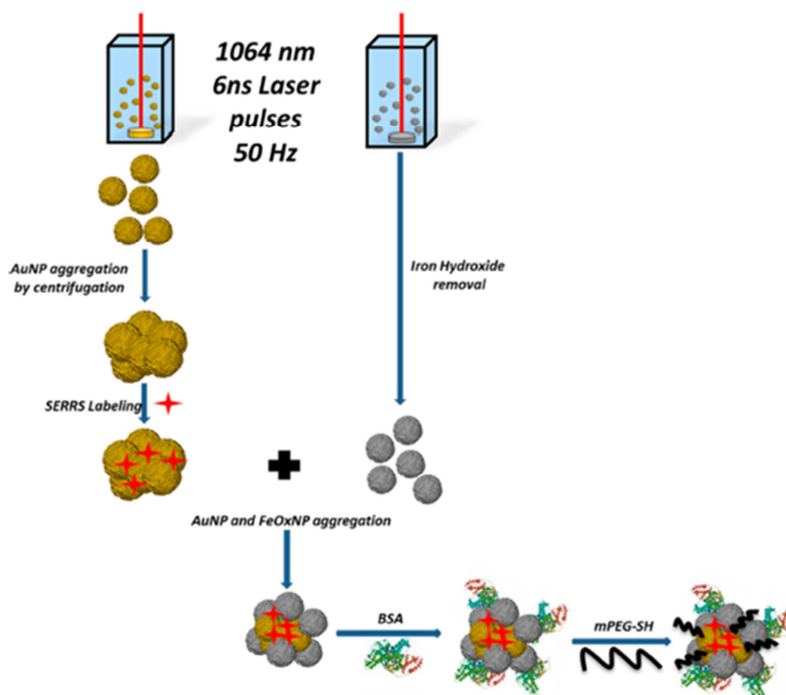


Figure 2.3 Steps for the synthesis of magneto-plasmonic AuFeO_xNC functionalized with Texas Red as SERRS label, BSA and mPEG-SH.¹³

The UV-Visible-NIR spectrum of AuFeO_xNC is reported in figure 2.4 a. Here one can observe the surface plasmon resonance peaks at 500-700 nm, typical of gold nanoparticles aggregates as seen before. Contribution of FeO_xNPs is observed between 450 nm and 300 nm, where these these NPs absorbs (see inset graph in figure 2.4 a) and contribution from BSA and mPEG-SH can be found only below 300 nm.

In figure 2.4 b, typical SERRS signals of Texas Red are shown. Comparing intensities of the peaks with those on figure 2.2 e, one can see that intense signals are present also in AuFeO_x NC, confirming that hot spots of AuNPs are conserved also when assembled with iron oxide nanoparticles.

One representative TEM image of AuFeO_xNC is shown in figure 2.4 c where one can see how gold nanoparticles (the darker ones) and iron oxide nanoparticles are arranged within a nanocluster.

Z-potential measurement performed on BSA and mPEG-SH functionalized AuFeO_xNC showed values of -5mV, like for uncoated nanoclusters. This highlights the importance of BSA and mPEG-SH coating for the stabilization of AuFeO_xNC.

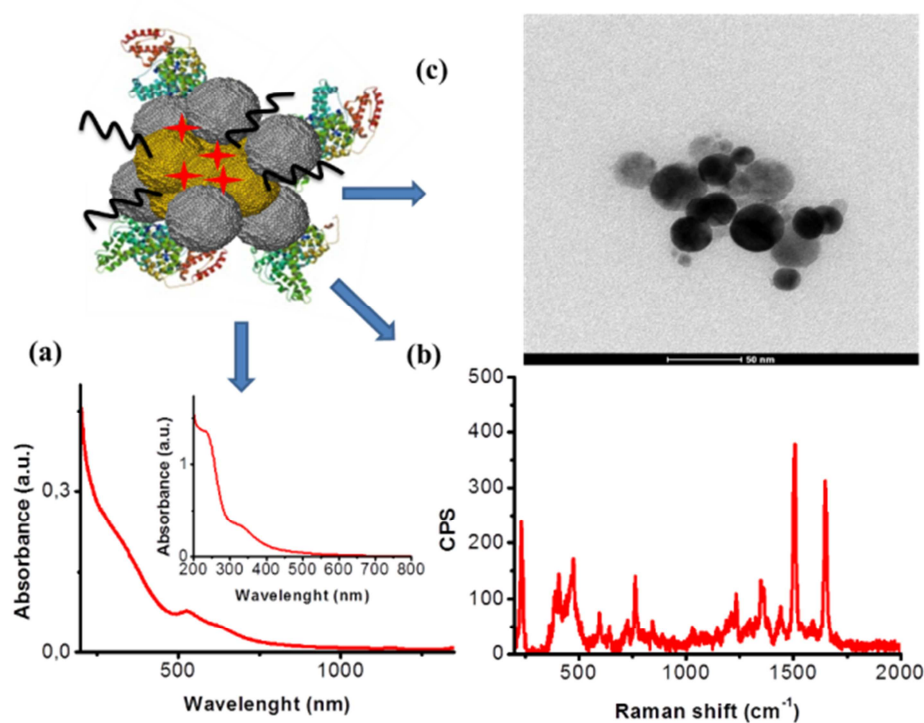


Figure 2.4 (a) UV-Vis-NIR spectra of synthesized AuFeO_xNC functionalized with TR-SH, BSA and mPEG-SH. Inset graph show absorption of FeO_xNPs in acidic solution and explain small wavelength absorption of AuFeO_xNC. (b) SERRS spectra of AuFeO_xNC+TR-SH+BSA+mPEG-SH showing typical Texas Red peaks. (c) TEM image of AuFeO_xNC.¹³

To investigate the magnetic properties of AuFeO_xNCs the solution was placed in the proximity of a NdFeB permanent magnet (figure 2.5 a), monitoring the variation of the absorption spectrum of the solution in time.

For this purpose, a quartz cuvette with 10 mm optical path is filled with AuFeO_xNC solution and placed in proximity of NdFeB magnets. The cuvette with magnets is

placed inside a UV-Visible spectrometer and the first spectrum was recorder at the initial state ($t = 0$). As the time increase the absorbance decreases due to particles migration toward the magnets. At time $t = t_{1/2}$ the absorbance is half of its initial value, meaning that half of AuFeO_xNC have been attracted to magnets (figure 2.5 b). Monitoring the absorbance at 450 nm, spectra were collected every 5 minutes for 200 minutes (figure 2.5 c). Absorbance at 450 nm was chosen because both gold and iron oxide nanoparticles absorbs at this wavelength. In less than 100 minutes, almost all AuFeO_xNC are attracted to magnets, as can be observed in figure 2.5 c.

Comparing the three spectra taken at times $t = 0$, $t = t_{1/2}$ and $t = 200$ min (figure 2.5 d), one can conclude that the assembling of gold and iron oxide nanoparticles occurred for all the nanoparticles.

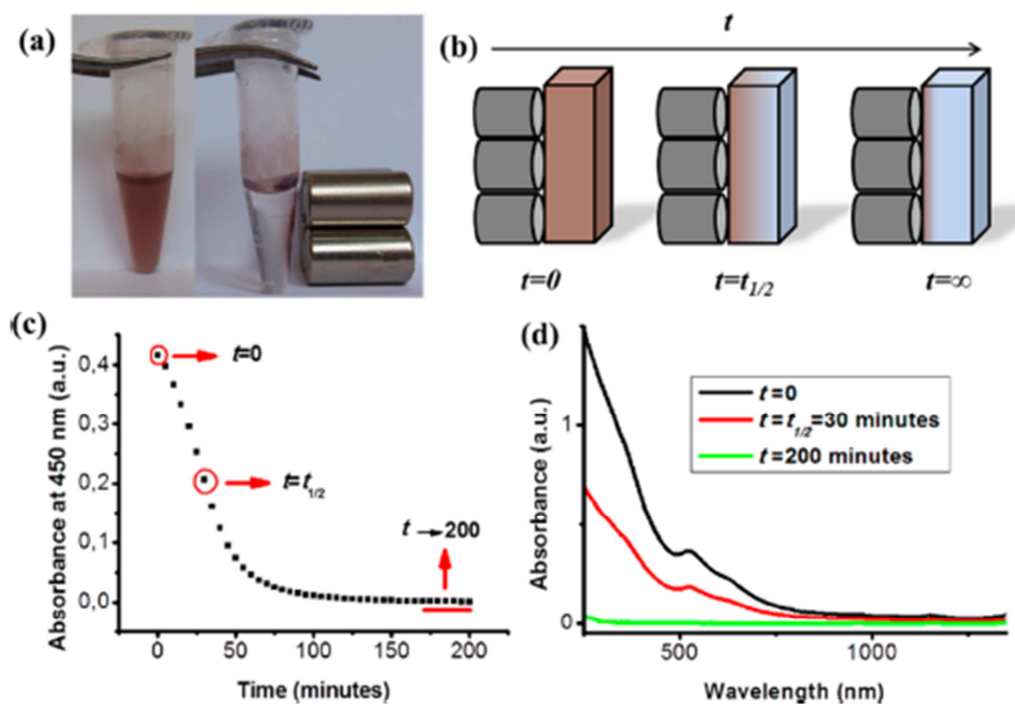


Figure 2.5 (a) Picture showing the response of AuFeO_xNC when a magnetic field gradient is applied. (b) A 10 mm quartz cuvette in contact with magnets is filled with AuFeO_xNC . As the time increase, the absorbance decreases due to particles migration. (c) Graph showing absorbance at 450 nm versus time. Spectra are collected every 5 minutes for 200 minutes. (d) Graph reporting spectra of functionalized AuFeO_xNC in three representative moments of their migration: the beginning of the experiment ($t = 0$, black spectra), when absorbance is half of the initial one ($t = t_{1/2}$, red spectra) and when all particles have been attracted ($t = 200$ minutes, green spectra).¹³

In fact, in these spectra, one can see absorptions of gold and iron oxide nanoparticles decreasing in the same proportions, as time increases. This shows that in all the attracted nanoparticles there were both magnetic and plasmonic nanoparticles.

The magnetophoresis of iron oxide nanoparticles in liquid is strongly dependent on nanoparticle sizes. In particular, bigger nanoparticles migrate toward magnets faster than smaller ones.¹⁶ The same considerations can be made for AuFeO_xNC where faster kinetics, with lower $t_{1/2}$, were observed with larger aggregates containing more iron oxide nanoparticles.

In vitro application

Since AuFeO_x NC showed good magnetic and SERRS properties, we considered the possibility to load murine macrophage cells type RAW 264.7 with the nanoclusters. As recalled above, macrophages loaded with a magneto-plasmonic system like AuFeO_xNC can be used for theranostic application.

We first incubated macrophages with AuFeO_xNC (figure 2.6 a).

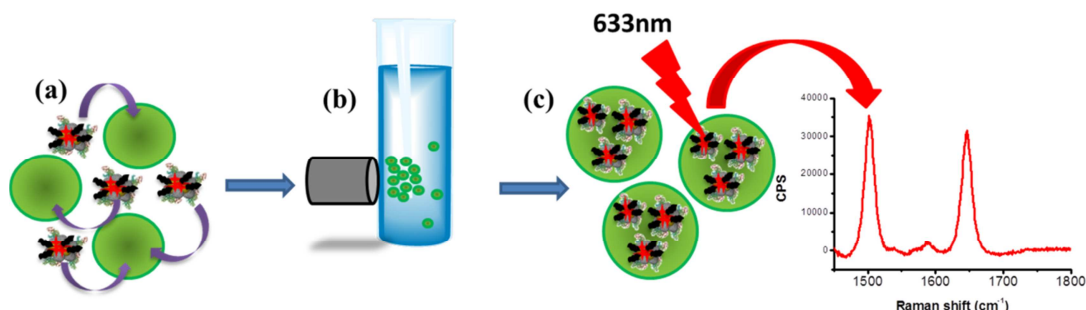


Figure 2.6 Scheme with experimental passages for macrophage labeling and sorting. First macrophages are incubated with AuFeO_xNC (a) and then sorted (b). When focusing a 633 nm laser on a single cell, Raman spectra of TR-SH is obtained, confirming the internalization of AuFeO_xNC (c).¹³

In order to obtain a population of cells with a satisfactory particles loading, cells were sorted for 10 minutes using a commercial magnetic particle concentrator (figure 2.6 b) and deposited on a glass slide.

SERRS analysis were performed on single cells (figure 2.6 c) using 633 nm laser line with an output power of 1.54 mW and 20× magnification. Spectra on more than 100 cells were acquired looking for the most intense signal of Texas Red at 1505 cm⁻¹.

Histogram in figure 2.7 shows signal intensities distribution at 1505 cm^{-1} vs number of cells.

The presence of TR-SH Raman signals in all sorted cells confirms the uptake of AuFeO_xNC and that nanoclusters show stable SERRS signal also after their inclusion within cells.

To show that quantitative cell guiding using a magnetic field is possible, we performed an experiment in which AuFeO_xNC loaded macrophages were sorted after being mixed with non-treated macrophages.

After 24 hours incubation with nanoclusters, cells were washed multiple times with PBS and treated with carboxyfluoresceinsuccinimidyl ester (CFSE), a fluorescent vital dye.

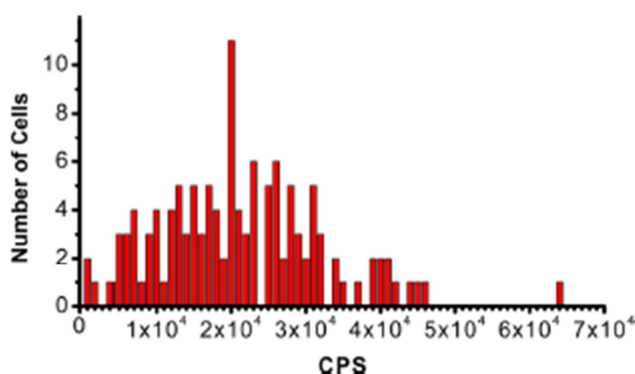


Figure 2.7 Histogram showing signal intensities distribution vs number of cells. The TR-SH signal was detected in all cells confirming the presence of functionalized AuFeO_xNC inside the cells.¹³

Then, NC loaded and stained cells were mixed in equal proportions with other macrophage cells which had not undergone any treatment.

Flow cytometry analysis is used to determine the percentage of the two populations of cells in the mixed solution. Figure 2.8a show flow cytometry with relative percentages of treated and untreated cells before the magnetic sorting.

The solution containing the mixed cells is then placed in the proximity of a commercial NdFeB particle concentrator for 10 minutes in order to separate NC loaded and stained cells.

Flow cytometry shows that 95.6% of cells incubated with AuFeO_xNC were magnetically sorted (Figure 2.8b), while unsorted cells were found to be those untreated (Figure 2.8c).

We verified also that the small amount of unsorted cells is due to mechanical mixing occurring during magnetic separation.

This experiment highlights the efficiency of AuFeO_xNC in magnetic cell guiding in a solution where other cells were presents.

It should be noted that usually such magnetic efficiency is obtainable with commercial magnetic beads with sizes in the order of micrometers. In this case, AuFeO_xNC aggregates have sizes between 150-200 nm, notably smaller with respect to commercial ones.

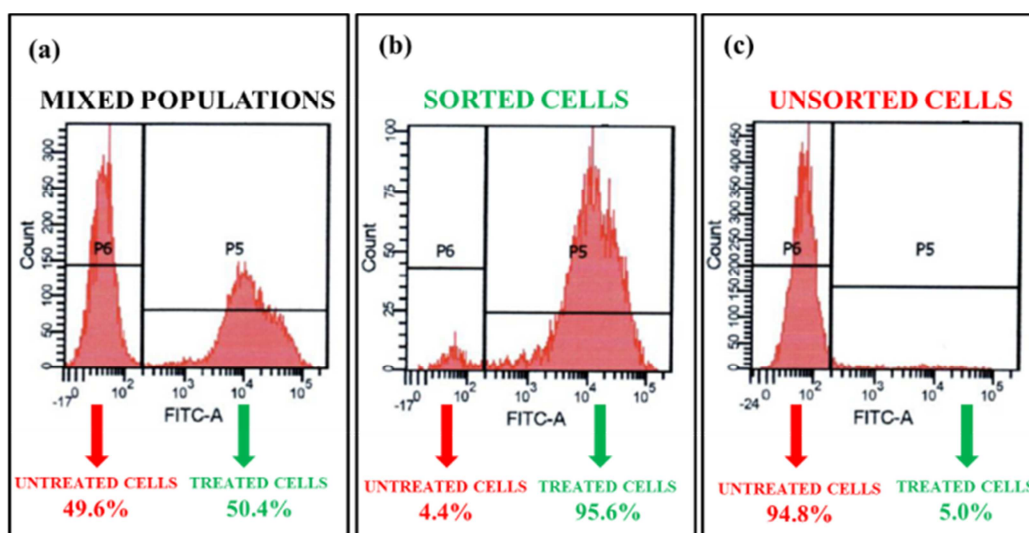


Figure 2.8. Performance evaluation of magnetic cell sorting by flow cytometry. (a) RAW 264.7 macrophages incubated with AuFeO_xNC and marked with fluorescent label CFSE mixed in equal proportion with untreated macrophages. (b) Flow cytometry showing that 95.6% of magnetically sorted cells were those incubated with AuFeO_xNC. (c) Flow cytometry of unsorted cells shows that macrophages treated with AuFeO_xNC are practically absent.¹³

Furthermore, AuFeO_xNC showed good labeling properties thanks to high SERRS signals. SERRS measurements showed that typical TR-SH signals were present on sorted cells.¹³

Conclusion

Magneto/plasmonic nanostructures are of particular interest in nanomedicine because allows cell manipulation and identification using only one system. However, their synthesis is often complex and require more passages with several purification steps due to chemicals required for synthesis.

Chapter 2

In the present case, AuFeO_xNC are synthesized from laser ablated gold and iron oxide nanoparticles and assembled exploiting the different surface charges of the two nanoparticles.

The absence of chemicals to stabilize just synthesized nanoparticles or to assemble the nanoclusters makes AuFeO_xNC simple to produce and suitable for use in nanomedicine.

Magnetic and plasmonic properties can be tuned depending on the needs simply changing molar proportions between nanoparticles. TEM images and DLS measurements show nanoclusters with dimensions between 150 nm and 200 nm.

We observed that SERRS and magnetic properties of the nanoclusters were maintained also after the assembling and use for cell manipulation. Micro-Raman measurement performed at single cell level showed high SERRS signals, confirming the possibility to perform imaging on sorted cells. FACS experiment showed that up to 95% of cells incubated with AuFeO_xNC can be sorted in solution in less than 10 minutes.

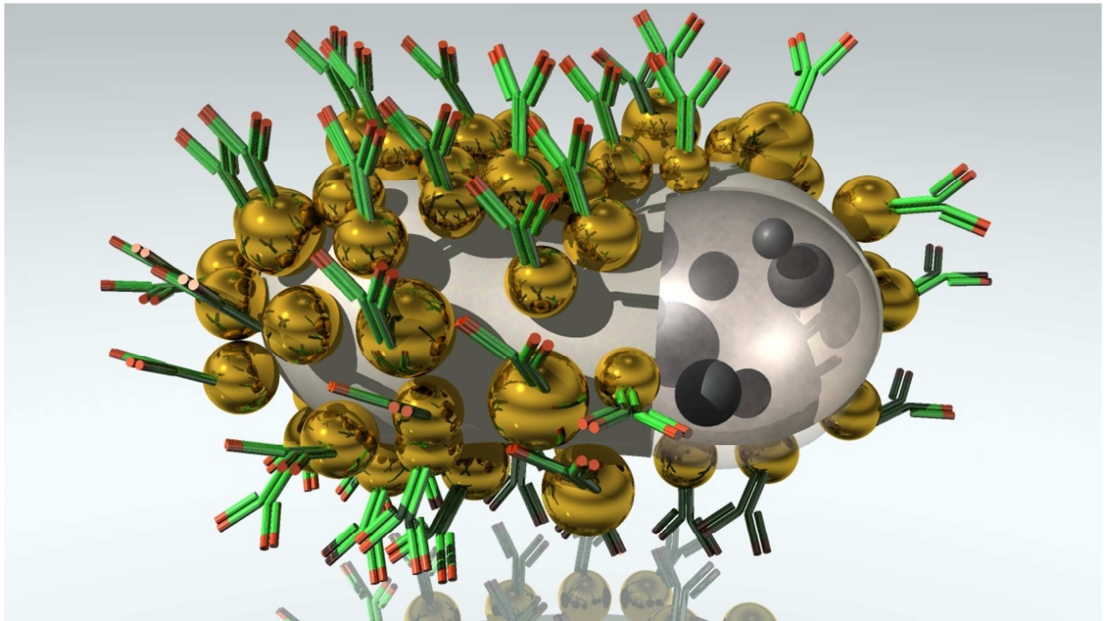
The work presented in this chapter has been published in 2014.¹³

References

- (1) Murdoch, C.; Giannoudis, A.; Lewis, C. E. Mechanisms regulating the recruitment of macrophages into hypoxic areas of tumors and other ischemic tissues, *Blood* **2004**, *104*, 2224-2234.
- (2) Lin, E. Y.; Nguyen, A. V.; Russell, R. G.; Pollard, J. W. Colony-stimulating factor 1 promotes progression of mammary tumors to malignancy, *J. Exp. Med.* **2001**, *193*, 727-740.
- (3) Amendola, V.; Riello, P.; Polizzi, S.; Fiameni, S.; Innocenti, C.; Sangregorio, C.; Meneghetti, M. Magnetic iron oxide nanoparticles with tunable size and free surface obtained via a “green” approach based on laser irradiation in water, *J Mater Chem* **2011**, *21*, 18665-18673.
- (4) Vogel, A. I. In *Vogel's textbook of quantitative chemical analysis*; Longman Scientific & Technical: UK, 1989.
- (5) Amendola, V.; Meneghetti, M. Size Evaluation of Gold Nanoparticles by UV–vis Spectroscopy, *J Phys Chem C* **2009**, *113*, 4277-4285.
- (6) Meneghetti, M.; Scarsi, A.; Litti, L.; Marcolongo, G.; Amendola, V.; Gobbo, M.; Di Chio, M.; Boscaini, A.; Fracasso, G.; Colombatti, M. Plasmonic Nanostructures for SERRS Multiplexed Identification of Tumor-Associated Antigens, *Small* **2012**, *8*, 3733-3738.
- (7) U.S. Environmental Protection Agency In *Test Methods for Evaluating Solid Waste, Physical/Chemical Methods, U.S. EPA SW-846*; U.S. Government Printing Office: Washington DC, 1996.
- (8) Lorentzen, E. M.; Kingston, H. “ Comparison of microwave-assisted and conventional leaching using EPA method 3050B, *Anal. Chem.* **1996**, *68*, 4316-4320.
- (9) Amendola, V.; Meneghetti, M. Laser ablation synthesis in solution and size manipulation of noble metal nanoparticles, *Phys Chem Chem Phys* **2009**, *11*, 3805-3821.
- (10) Amendola, V.; Meneghetti, M.; Granozzi, G.; Agnoli, S.; Polizzi, S.; Riello, P.; Boscaini, A.; Anselmi, C.; Fracasso, G.; Colombatti, M. Top-down synthesis of multifunctional iron oxide nanoparticles for macrophage labelling and manipulation, *J Mater Chem* **2011**, *21*, 3803-3813.
- (11) Amendola, V.; Meneghetti, M. Controlled size manipulation of free gold nanoparticles by laser irradiation and their facile bioconjugation, *J Mater Chem* **2007**, *17*, 4705-4710.

- (12) Zhou, J.; Ralston, J.; Sedev, R.; Beattie, D. A. Functionalized gold nanoparticles: synthesis, structure and colloid stability *J. Colloid Interface Sci.* **2009**, *331*, 251-262.
- (13) Bertorelle, F.; Ceccarello, M.; Pinto, M.; Fracasso, G.; Badocco, D.; Amendola, V.; Pastore, P.; Colombatti, M.; Meneghetti, M. Efficient AuFeO_x Nanoclusters of Laser-Ablated Nanoparticles in Water for Cells Guiding and Surface-Enhanced Resonance Raman Scattering Imaging, *J Phys Chem C* **2014**, *118*, 14534-14541.
- (14) Ravindran, A.; Singh, A.; Raichur, A. M.; Chandrasekaran, N.; Mukherjee, A. Studies on interaction of colloidal Ag nanoparticles with Bovine Serum Albumin (BSA), *Colloids and Surfaces B: Biointerfaces* **2010**, *76*, 32-37.
- (15) Xu, Y.; Linares, K.; Meehan, K.; Love, B.; Love, N. pH Dependent Change in the Optical Properties of Surface Modified Gold Nanoparticles Using Bovine Serum Albumin, *NSTI-Nanotech 2004*, *www.nsti.org*, ISBN 0-9728422-7-6 **2004**, *1*.
- (16) McCloskey, K. E.; Chalmers, J. J.; Zborowski, M. Magnetic cell separation: characterization of magnetophoretic mobility, *Anal. Chem.* **2003**, *75*, 6868-6874.

Chapter 3



FeO_xNP@dye-doped Silica@AuNP Core-Shell-Satellite nanostructures

In chapter 2 the synthesis and *in vitro* application of AuFeO_x nanoclusters was shown. Thanks to a good internalization in macrophage cells, an efficient magnetic guiding and cell identification was possible.

However AuFeO_xNC suffers of some limitations for their use with cells. In particular, the absence of targeting ligands (like antibodies) does not allow the selection of cells and their identification.

With macrophages a targeting ligand is not necessary because their biological function is to engulf particles, debris, foreign substances, cancer cells etc. that could be present in blood and for this reason AuFeO_xNC in solution are easily phagocytosed. However, aim of this thesis is the synthesis of nanostructures for magnetic sorting of specific cancer cells and their photothermal treatment. To achieve this goal with a nanostructure, the use of targeting ligands is necessary.

The use of antibodies in nanostructures for active targeting techniques has been widely discussed in the introduction of this thesis.

After the experiment with macrophages we tried immunomagnetic sorting of prostatic cancer cells using antibody functionalized AuFeO_xNC. Unfortunately, although antibodies were present on nanoclusters surface, the system was highly non-specific and both prostatic cancer cells and control cells were equally targeted. Non-specific interactions between nanoparticles and cells can depend on different parameters which are still object of study.¹

These observations lead us to think that AuFeO_xNC were not suitable to perform immunomagnetic sorting of cancer cells, even if they were very efficient in macrophage guiding and imaging. Therefore, a different nanosystem, with different characteristics was engineered, always with magneto-plasmonic properties.

Like in the previous chapter, here we present the synthesis of magneto-plasmonic nanostructures with a green approach following the green chemistry prescriptions and based on the laser ablation of bulk materials in water at room temperature and pressure. The synthesis proceeds with the assembling of the nanoparticles to produce FeO_xNP@dye-doped Silica@AuNP-Ab a core-shell-satellite (CSS) structure with a core of magnetic nanoparticles, a shell of silica and gold nanoparticles as satellite.

Then, the CSS are functionalized with D2B antibodies (CSS-Ab) for the targeting of the PSMA prostate specific membrane antigen which is overexpressed on prostatic cancer cells.

Unlikely AuFeO_xNC , in this case the coupling of magnetic and plasmonic nanoparticles has been faced by covering the magnetic nanoparticles with a silica shell exposing thiols on its surface and to which gold nanoparticles are quickly linked. This method also allows to better control the morphology of the as synthesized nanostructures.

In the silica shell a SERS reporter is included and its interaction with the gold nanoparticles makes the nanostructure also a very efficient SERS active probe.

A targeting activity of the nanostructures opens better perspectives both for imaging and therapeutic purposes. In these cases one needs also a further effort for a quantitative determination of the targeting activity in particular as a function of the concentration of the nanostructures, which is not usually available in literature.

Here we show quantitative evaluation of the targeting activity of antibody functionalized CSS nanostructures with PSMA positive and negative cells, exploiting their magnetic and SERS activities. Results show a very good targeting activity of the nanostructures with an overall targeting accuracy of 98% at picomolar concentrations.

Furthermore, we will show how CSS-Ab can be efficiently used for photothermal treatment of prostatic cancer cells. Different experimental approaches have been designed to prove their efficiency. Photothermal treatment is exploited using the plasmonic properties towards the NIR of gold nanoparticles present as satellites on the structure.

The last section of this chapter reports the efforts in tuning the plasmonic peaks to longer wavelengths, namely toward 900-1000 nm because this spectral region is more appropriate to perform plasmonic photothermal therapy.

Synthesis of Core-Shell-Satellite nanostructures

Synthesis of gold and iron oxide nanoparticles

Gold and iron oxide nanoparticles were synthesized according to the protocols already reported in chapter 2. The procedure was only modified for the amorphous phase removal in the synthesized iron oxide nanoparticles. In this case another cleaning procedure was performed by adding disodium EDTA at a final concentration of 9.4 mM.^{2, 3} After the addition, nanoparticles were maintained at 60°C for 1h under constant stirring and then washed several times with dd water after centrifugation cycles at 3700 rcf. This protocol variation was used because we experimentally observed that a more homogeneous silica shell is formed, in the following synthetic step, when FeO_xNPs are cleaned with EDTA and not with HCl. However, differences in FeO_xNPs morphology and size following the two protocols were not observed.

Assembling of antibody functionalized core-shell-satellite (CSS-Ab) nanostructures

The second step of the synthesis produces the Core-Shell nanostructures (CS), with a core of FeO_x and a shell of silica. The silica shell was synthesized using 3-mercaptopropyl trimethoxysilane (MPTMS, Sigma-Aldrich), as precursor, in a modified Stöber synthesis.⁴ 5 mL of FeO_xNPs (4.3 nM) were centrifuged, suspended in ethanol and mixed with 5 mg of MPTMS, 200 μL of dd H₂O, 125 μL of NH₄OH 30% and 5 mg of crystal violet (Sigma-Aldrich) as SERS reporter. In this case one can call the dye a SERRS (surface enhanced resonance Raman scattering) reporter since the spectra are recorded exciting at 633 nm, in resonance both with the localized plasmon resonance and the dye. The mixture was kept under vigorous stirring for 6 h at room temperature to obtain the CS nanostructures. The CS nanostructures were magnetically separated and washed four times with dd water and dispersed in 1 mL of phosphate buffered saline (PBS) solution in the last step.

The third step of the synthesis produces the core-shell-satellite (CSS) structures with AuNPs as satellites.

The strong linking of AuNPs to the silica shell is made possible by the presence of the thiol groups on the silica shell. The CSS synthesis was obtained by simply mixing the colloidal solution of AuNPs with CS nanostructures in PBS, and magnetically collecting the CSS nanostructures.

The presence of PBS or, more generally, a solution with high ionic strength is crucial in this step of the synthesis. In fact, both CS nanostructures and AuNPs are negatively charged at neutral pH. Z-potential measurements show values ranging from -35 mV to -40 mV for CS nanostructures and a value of -40 mV for AuNPs.

A negative surface charge of the silica coating of CS is present because, in addition to -SH functional groups, there are Si-OH terminal groups that are partially deprotonated at a pH=7 in water.⁵ The use of physiological PBS buffer helps to screen the negative charges for the large concentration of Na⁺ cations so the two different particles can bind to each other.⁶

In practice, the CS solution was mixed with 15 mL of AuNPs solution (6.4 nM), placed in a sonication bath for 30 minutes and then in proximity of a permanent magnet in order to separate core-shell-satellite nanostructures (CSS) with gold nanoparticles linked to the CS nanostructures, from nanoparticles with only AuNPs. Finally, CSS were washed, using three centrifugation cycles, and dispersed in 1 mL of PBS. In order to avoid the reactivity of remaining thiol groups on the CS surface, 0.1 mg of methoxy-polyethyleneglycol-maleimide (mPEG-MAL, Laysan Bio, 5000 Da) were added to the solution to block all the remaining free thiol groups. The CSS nanostructures were washed again with PBS, by three centrifugation cycles, and finally dispersed in 1 mL of PBS. The SERRS signals of the nanostructures were found to be strong and stable in time.

The fourth step of the synthesis corresponds to the functionalization of the CSS nanostructures with the D2B monoclonal antibody, specific for the PSMA antigen, to obtain CSS-Ab.

D2B was first functionalized with thiol groups (D2B-SH) by reacting the ammine groups of the lysine side chains with 2-iminothiolane (2-IT) accordingly to a previous published protocol.⁷ Briefly, functionalization was performed in PBS solution with 10% v/v NaHCO₃ 1 M and using a D2B to 2-IT molar ratio of 1:10. Reaction was kept at room temperature under vigorous stirring for 2h and then overnight at 4°C. Then, the functionalized antibody was purified from reaction

products using 5000 Da concentrators (Sartorius) and rinsed with PBS. The success of the functionalization was determined with a spectrophotometric measurement of the thiol groups using 4,4'-dithiodipyridine.⁸ Performing the test on the functionalized D2B antibody, and using pristine D2B as control, we measured an increment, on average, of about 1 thiol per antibody.

Functionalization of CSS with the antibody was performed adding 0.800 mg of functionalized D2B-SH to 1 mL of the CSS solution. Solution was stirred for 6 h at room temperature and then stored overnight at 4°C. CSS-Ab solution was then centrifuged and rinsed with PBS to remove unreacted antibody, and finally dispersed in 1 mL of PBS.

The estimation of the amount of antibody conjugated to the aggregates, was obtained by comparing the absorbance at 280 nm of the initial D2B-SH solution with the supernatant solution after the cleaning centrifugations and it shows that about 300 antibodies are present on average for each CSS-Ab structure, namely about one antibody per AuNP (see below for the characterization of the nanostructures).

To complete the synthesis and add stealth properties to the CSS-Ab nanostructures, 0.01 mg of methoxy-polyethylene-glycol-thiol (mPEG-SH, Laysan Bio, 5000 Da) were added to the solution of CSS-Ab. mPEG-SH was added also to saturate all available linking sites on gold nanoparticles.

After 15 minutes of reaction, in a sonication bath, CSS-Ab nanostructures were magnetically collected and dispersed in 1 mL of PBS.

The whole synthesis procedure is sketched in figure 3.1.

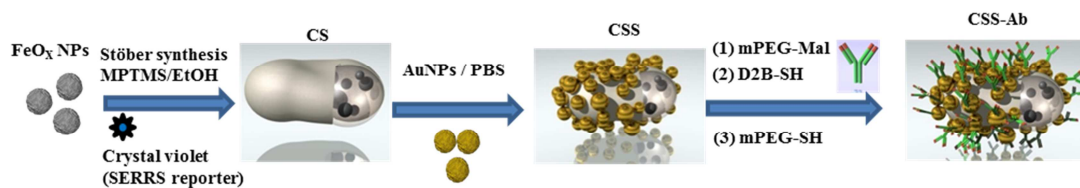


Figure 3.1 Steps of the synthesis of FeO_xNPs@dye-doped Silica@AuNPs-Ab core-shell-satellite (CSS) nanostructures and their conjugation with D2B antibody (CSS-Ab).

The presence of the Ab on the CSS-Ab was confirmed by flow cytometric measurements with a BD FACSCanto flow cytometer. CSS-Ab were incubated with a fluoresceine-labeled goat anti-mouse antibody (GAM-FITC, see figure 3.5 in the characterization section), and after some washing steps, the aggregates were

analyzed by flow cytometry. For reference, flow cytometry analysis was also performed only on CSS nanostructures not incubated with GAM-FITC.

The D2B activity on CSS-Ab for PSMA present on cells was obtained with a flow cytometry analysis using PC3-PIP. Cells were incubated with CSS nanostructures and then, after two washing steps, with GAM-FITC to stain NPs linked to cell surface. A positive control, prepared only with D2B antibody, before the GAM-FITC staining, and a negative one using only GAM-FITC without CSS-Ab or D2B, were also analyzed. The same measurements were performed on PC3 cells that do not express the PSMA antigen (see Figure 3.6 in the characterization section).

Au and Fe concentrations in final preparations were determined with an ICP-MS Thermo Elemental, X7 Series equipped with the PlasmaLab software. Using nanoparticle mean diameters, obtained by TEM images for FeO_xNPs and fitting of the localized surface plasmon spectra for AuNP, and the bulk densities, of the two materials, one estimates a AuNPs concentration of 23 nM and FeO_xNPs of 6 nM, namely a ratio of 3.8.

The concentration ratio of the two types of atoms was also confirmed by EDX measurements performed with a JSM Jeol 6490 SEM-EDX microscope at 20 kV. CSS-Ab structure concentration in final preparation is estimated to be 89 pM. This concentration was obtained by dividing the total number of FeO_xNPs in solution by the average number of FeO_xNPs present in a single core-shell particle evaluated by examining about 30 TEM images like that in Figure 3.2A.

Experimental procedures concerning the use of CSS-Ab for immunomagnetic sorting and photothermal treatment of cancer cells are described in the experimental part.

Characterization of antibody functionalized core-shell-satellite (CSS-Ab) nanostructures

Instruments and techniques for the characterization of CSS-Ab nanostructures

Instruments and techniques are those already reported for the synthesis and characterization of AuFeO_xNC (see pag. 92).

Characterization

The characterization of AuNPs and FeO_xNPs made by laser ablation synthesis in solution is reported in subchapter “Results” of chapter two.

Figure 3.2A shows a representative TEM image of the CS nanostructures where the FeO_xNP are seen as darker particles inside the structure.

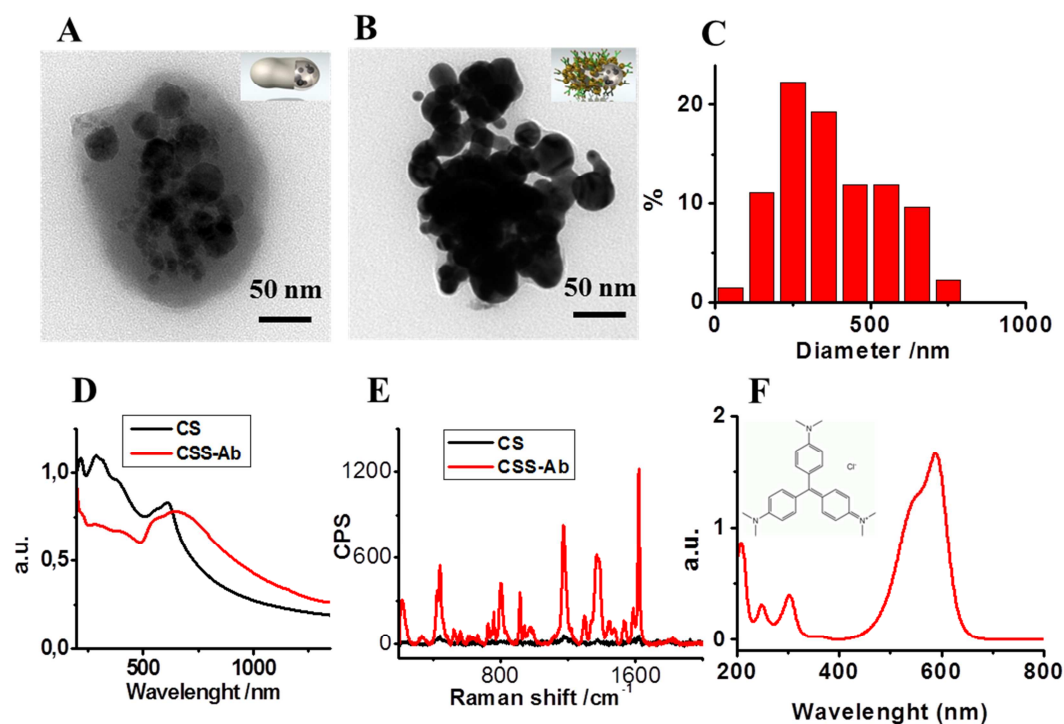


Figure 3.2 TEM images of (A) FeO_xNPs@dye-doped Silica core-shell (CS) nanostructures and (B) FeO_xNPs@dye-doped Silica@AuNPs core-shell-satellite (CSS) nanostructures. (C) Size distribution of CSS nanostructures from TEM images. (D) UV-Visible-NIR absorption spectra of FeO_x NPs@dye-doped Silica (CS) (black line) and FeO_x NPs@dye-doped Silica@AuNPs (CSS) nanostructures in water. (E) Raman spectrum of CS nanostructures (black) and SERRS spectrum of crystal violet obtained with CSS structure in water ($\lambda_{\text{Laser}} = 633 \text{ nm}$). (F) UV-Visible spectra of an aqueous solution of Crystal Violet and its molecular structure.

AuNPs are linked to the CS nanostructures to obtain the final core-shell-satellite (CSS) nanostructures.

After AuNPs binding to CS, the overall Z-potential sets at about -30 mV. This value was maintained also after conjugation with antibodies, mPEG-MAL and mPEG-SH (see below). This is a good value for stability of nanostructures in solution and allows reducing unspecific interactions with cells.

The magnetic sorting was used to separate aggregates with magnetic properties from pure AuNP aggregates. One finds that the separated aggregates show the localized plasmon resonances extending in the near infrared, which is characteristic of

aggregated gold nanoparticles. Figure 3.2B shows a TEM image of a characteristic CSS aggregate and Figure 3.2C their size distribution. Other CSS TEM figures are available in figure 3.3. CSS mean diameter results to be 368 ± 159 nm, which was confirmed by a Z-average value of 437 nm obtained with a DLS analysis.

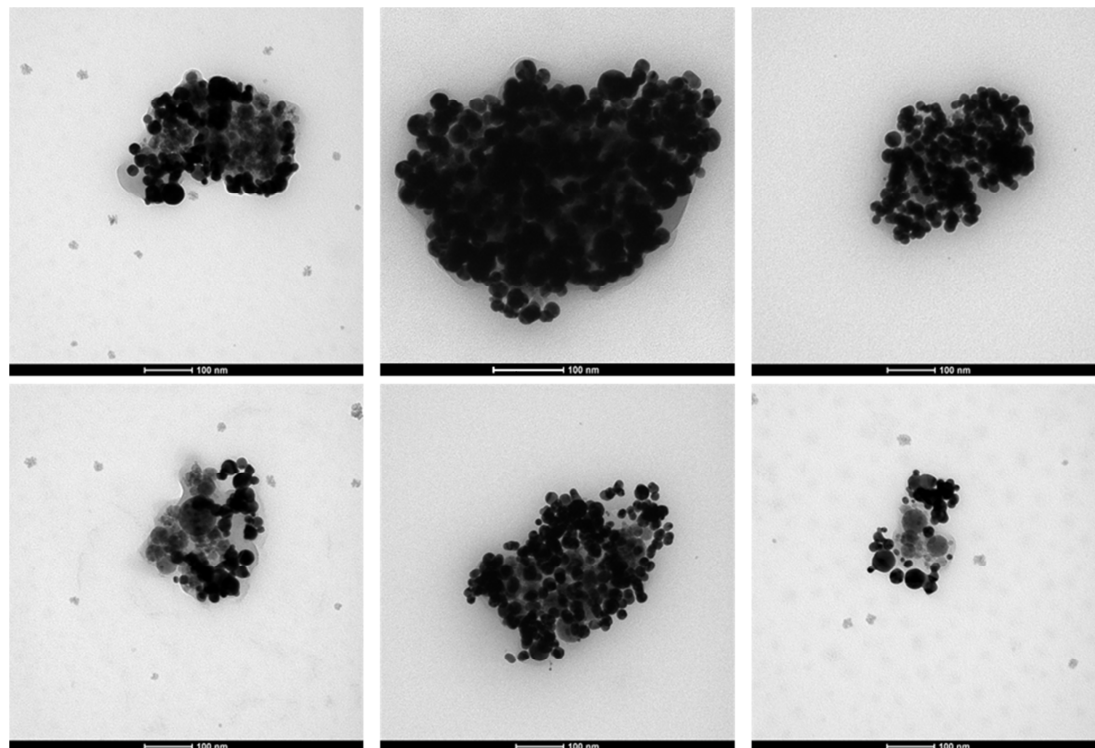


Figure 3.3 Additional TEM micrographs of CSS-Ab nanostructures.

All residual thiols on the silica shell were saturated with methoxy-polyethyleneglycol-maleimide that prevents any residual unwanted reaction of the thiol groups. This is important also for the control of the interaction with cells.

CSS composition is obtained with an EDX measurement and shows, by weight, 84% Au and 16% Fe (see Figure 3.4).

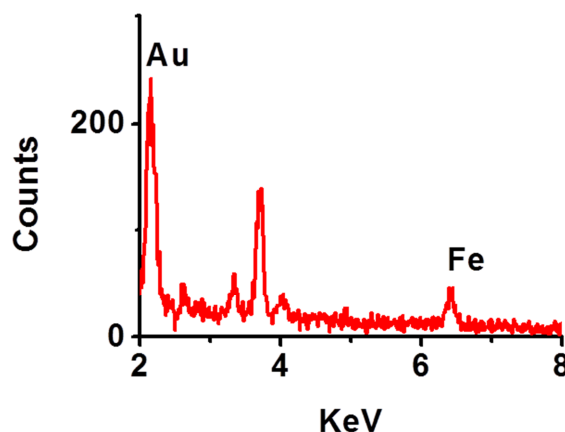


Figure 3.4 EDX measurement performed on a sample of FeO_xNP@dye-doped Silica@AuNPs core-shell-satellite (CSS) nanostructures.

Considering that, on average, are present AuNPs of 20 nm and FeO_xNPs of 25 nm, one obtains a ratio of AuNPs/FeO_xNPs of 3.5. This value is in good agreement with the ratio of 3.8 obtained from the concentrations of Au and Fe obtained from ICP-MS analysis. The absorption spectrum of CSS nanostructures in water is reported in Figure 3.2D (red line) and shows a broad band from 500 nm to 750-800 nm. Compared with the absorption spectrum of the CS nanostructures without satellite AuNPs (Figure 3.2D, black line), in which also the crystal violet absorption peak is clearly visible at about 600 nm, one finds that the AuNPs contribution is observed as a broad absorption from 500 nm to 750-800 nm, which is characteristic of aggregated AuNPs, as observed above.^{7,9} Since the dye absorption band at 600 nm (Figure 3.2F) is in resonance with the laser light used for the SERS measurements at 633 nm (see below), CSS nanostructures are also optimized for SERRS (surface enhanced resonance Raman scattering) in which both the plasmon enhancement and the molecular resonance enhancement are present. In Figure 3.2E (red line) SERRS spectra of crystal violet in CSS nanostructures is reported. Although the dye molecules are not directly linked to the AuNPs, large signals are observed, comparable to those observed linking directly the molecules on the surface of aggregated AuNPs. Since SERS signals strongly depend on the distance between molecules and the AuNPs surface, the observed intensity of the signals shows that dye molecules are present on the surface of the CS nanostructures and that a strong interaction with the AuNPs is present. For comparison, one can see very small

Raman signals arising from CS nanostructures, in which AuNPs are not present (Figure 3.2E, black line).

The D2B antibody (specific for prostate specific membrane antigen, PSMA)¹⁰ coupling to CSS (CSS-Ab) was performed using the thiol functionalized antibody (D2B-SH), obtained according to the procedure described in the “Assembling of antibody functionalized core-shell-satellite (CSS-Ab) nanostructures” section.

The presence of antibodies on CSS-Ab was verified with flow cytometry analysis by incubating the CSS-Ab nanostructures with FITC labeled goat antimouse anti-antibody (GOAT-FITC). Results from flow cytometry analysis show the presence of D2B antibody on the CSS-Ab nanostructures while no FITC signal was detected in reference samples (Figure 3.5).

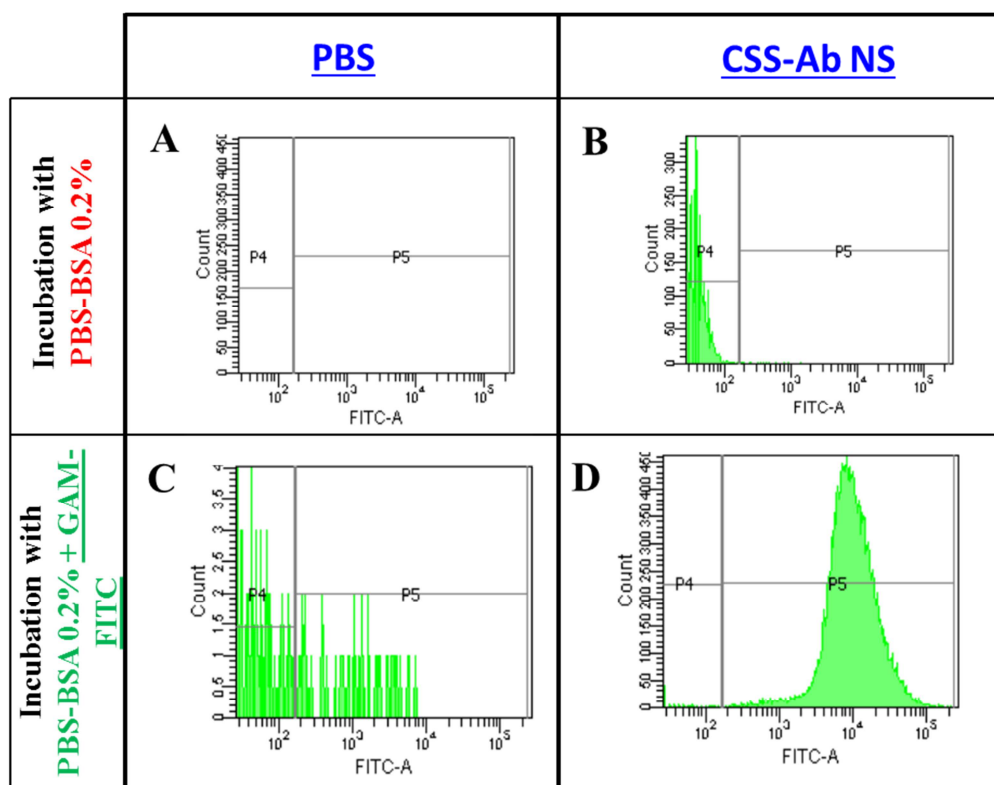


Figure 3.5 Flow cytometry analysis of (A) solution of 0.2% BSA in PBS, (B) CSS nanostructures in a solution of 0.2% BSA in PBS (C) GAM-FITC in 0.2% BSA in PBS and (D) CSS-Ab incubated with GAM-FITC. Fluorescence signals are recorded only for sample (D) demonstrating the presence of D2B antibodies on CSS-Ab.

The activity of the antibodies was assessed by incubating the CSS-Ab nanostructures with PC3-PIP cells, which overexpress prostate specific membrane antigen (PSMA+), or with PC3 cells, which do not express this antigen (PSMA-). After incubation and

several washing, the presence of CSS-Ab nanostructures on cells surface was assessed by using GAM-FITC reagent. Flow cytometry results are reported in figure 3.6 and show that the CSS-Ab nanostructures efficiently target only PC3-PIP (PSMA+) cells (Figure 3.6C and 3.6F). Their target specificity is found comparable to that of pure D2B antibody in solution (Figure 3.6B and 3.6E). Control measurements show that GAM-FITC does not bind to the two cell types (Figure 3.6A and 3.6D). The total number of antibodies present on a CSS-Ab was obtained by using the absorption decrease at 280 nm of the supernatant of the reaction synthesis (see figure 3.7). One can deduce that ca. 300 active antibodies are present per CSS-Ab nanostructure, namely about one antibody, on average, per AuNP. However, only a small number of them will be active, of the order of some %, ¹¹ since these large proteins can have different orientations on the surface of a nanoparticle, namely side-on and end-on orientation, and they can also form layers so that only a small number can interact with antigens on cells.

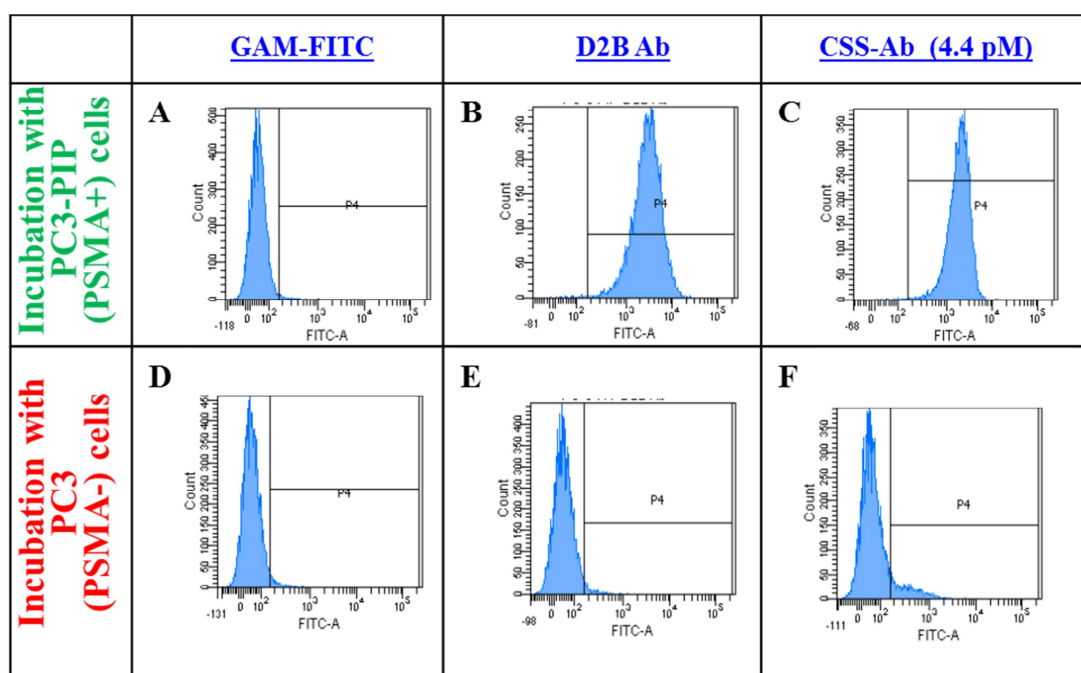


Figure 3.6 Flow cytometry analysis of PC3 PIP (PSMA+) in the upper part and of PC3 in the lower part. Cells are incubated only with GAM-FITC ((A) and (D)), pure D2B and then with GAM-FITC ((B) and (E)) and CSS-Ab at a concentration of 4.4 pM and then with GAM-FITC ((C) and (F)). The data show that CSS-Ab has an activity of D2B antibody similar to pure D2B and that the activity is specific for PSMA present on PC3PIP cells.

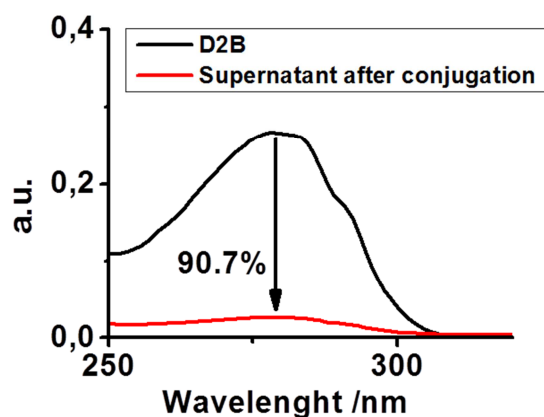


Figure 3.7 Absorption spectra of D2B solution before conjugation (black line) and in the supernatant (red line) after conjugation and centrifugation.

Immunomagnetic sorting of cancer cell

Methods

Cell cultures

PC3 cells are prostate human cells purchased from the American Type Culture Collection (ATCC, Rockville, USA) and cultured in RPMI 160 Medium (Biochrom GmbH, Berlin, Germany) supplemented with 2 mM L-glutamine, 10% heat-inactivated fetal bovine serum (FBS, Lonza Swiss) and antibiotics (0.1 mg ml⁻¹ streptomycin and 100 units ml⁻¹ penicillin G, Sigma-Aldrich, St Louis, MO, USA). PC3-PIP cells, permanently transfected with human PSMA antigen, were kindly provided by Dr. W. Heston (Department of Cancer Biology, Lerner Research Institute, Cleveland) and are widely described in the literature.¹² Cells were grown in culture flasks and maintained in an incubator at 37 °C and 5% of CO₂ under a humidified atmosphere.

Cell incubation, immunomagnetic sorting and single-cell SERRS analysis

For immunomagnetic sorting experiments, 250000 PC3-PIP (PSMA+) cells were incubated with increasing concentrations (1.1, 2.2, 4.4, 8.9 and 17.8 pM) of CSS-Ab nanostructures in a volume of 200 µL for 1 h at 4°C in the presence of 5% Bovine Serum Albumin (BSA) to block non-specific protein interactions. Then, the solution

was placed in the proximity of a commercial magnetic particle concentrator (DynaL MPC-L, Invitrogen) and, after 10 minutes, magnetically sorted cells were collected, and, separately, those which were not magnetically collected. Then, cells were washed with PBS solution, counted and seeded on a glass slide. After cell adhesion, cells were fixed by a 2% paraformaldehyde solution for 30 minutes at room temperature, and then glass slides were washed, rinsed in water and dried.

SERRS measurement of each single cell were performed with a Renishaw inVia micro-Raman instrument using a 20x objective and, for 1s for each cell, 1.5 mW of a He-Ne laser line at 633 nm. The localization of cells and the automatic measurements of the spectra of all single cells was possible with a home-made software. Optical images of CSS-Ab on cells have been acquired with the microscope of the Raman spectrophotometer while FE-SEM images were performed with a Zeiss instrument at 3.00 kV and 10.00 kV.

Results

The performance of CSS-Ab in targeting and sorting of cancer cells was obtained with incubation with PC3-PIP cells, which overexpress PSMA (PSMA+) and with PC3 cells, which do not overexpress PSMA, (PSMA-) (figure 3.8). Increasing concentrations of CSS-Ab were used to verify how they affect the sorting efficiency. After an incubation of one hour, cells were magnetically sorted by placing the solution in the proximity of a magnet for 10 minutes and then both sorted and unsorted cells were collected and counted. Several hundred thousand cells were used for obtaining good statistical results.

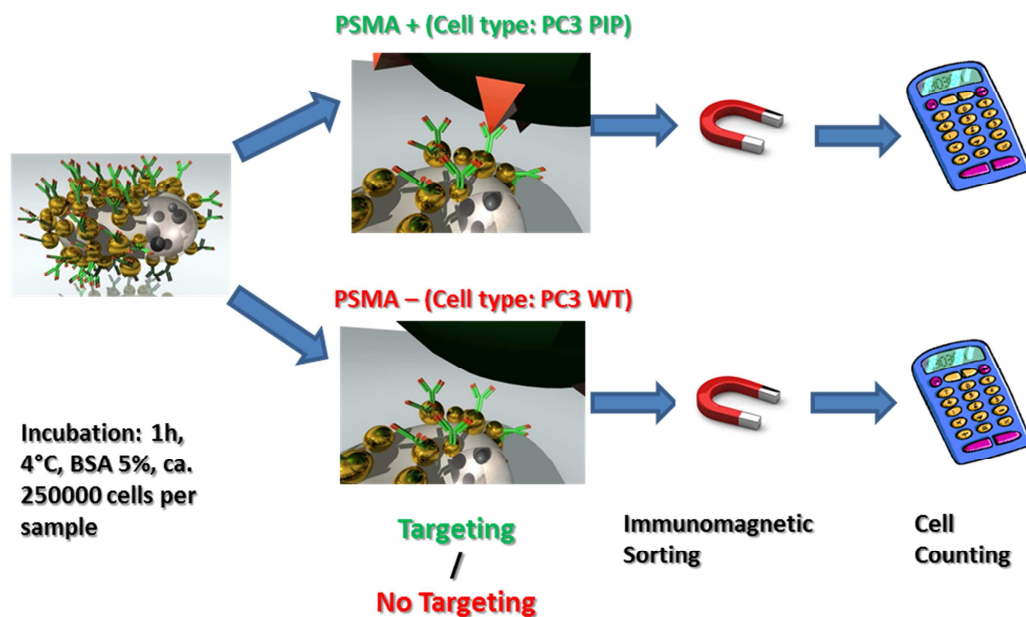


Figure 3.8 Scheme for immunomagnetic sorting performance evaluation of CSS-Ab nanostructures. CSS-Ab are separately incubated with cells expressing or not expressing PSMA antigen. After 1h incubation the solution is placed in a magnetic particle concentrator for 10 minutes and then cells are counted.

Graph in figure 3.9A shows percentages of magnetically sorted PSMA⁺ and PSMA⁻ cells as a function of CSS-Ab concentration. For low concentrations of CSS-Ab, of the order of 1 pM, 60-70% of PSMA⁺ cells were sorted. Increasing concentrations to 4.4, 8.9 pM, show a sorting saturation at about 90%. For PSMA⁻ cells the unspecific sorting was found to be low, below 5%, for low concentrations of nanoparticles, and it increases to 30% for 17.8 pM, the highest explored concentration.

The collected cells were fixed on a glass slide and their images, obtained with a 100x objective, allows to see the presence of the CSS nanostructures only on the surface of the PC3-PIP cells due to their strong scattering (see dark spots in figure 3.10). Here the dark spots show a variable local concentration of nanoparticles and this can be related to the local presence and clustering of the antigens on the cell surface.

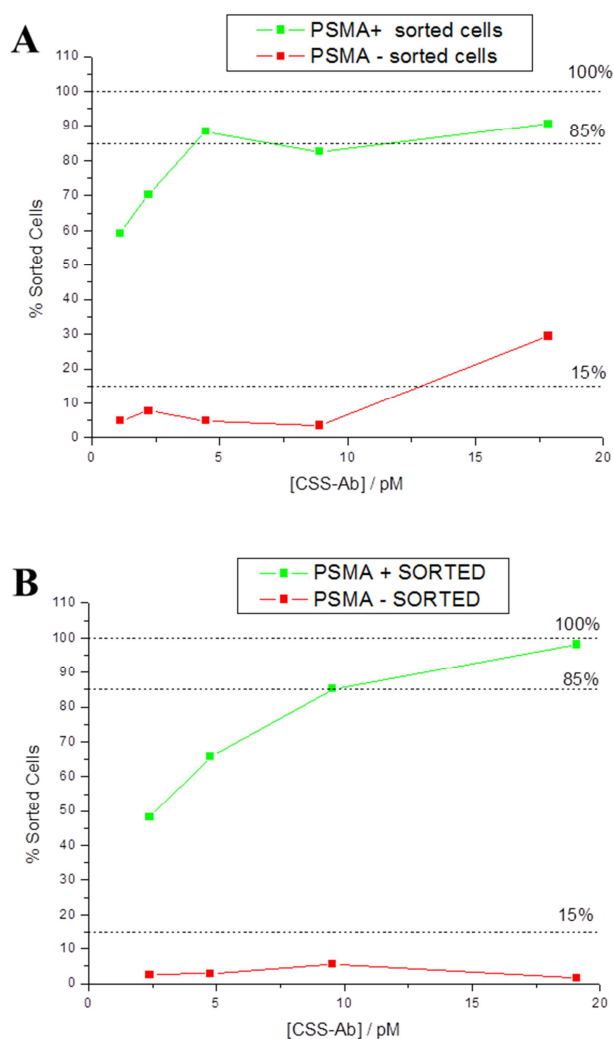


Figure 3.9 (A) Percentages of immunomagnetically sorted PSMA+ (PC3-PIP) and PSMA- (cells) as a function of CSS-Ab concentration during incubation. (B) Immunomagnetic sorting of cells with a different CSS-Ab batch shows reproducible trends in the same concentration range.

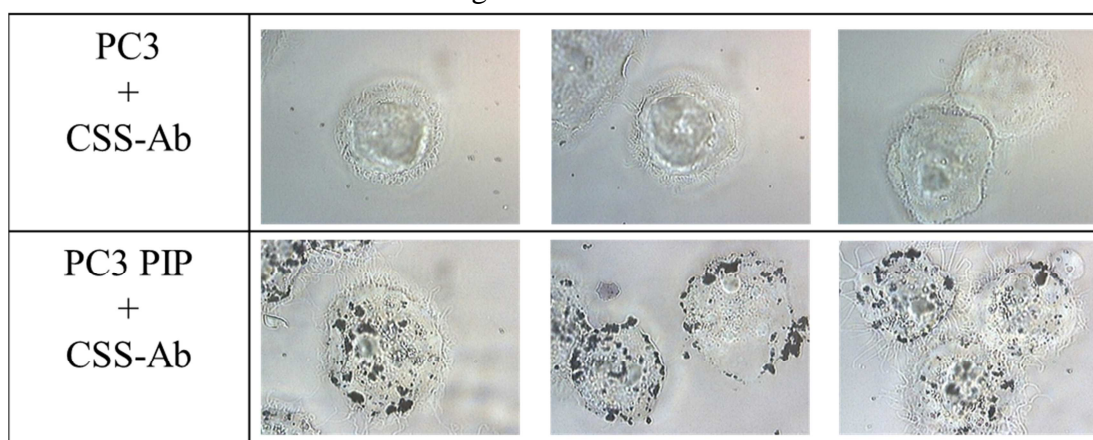


Figure 3.10 100 X Magnification images of PC3 cells (top) and PC3 PIP cells (bottom) incubated with CSS-Ab nanostructures. CSS-Ab nanostructures are visible as dark spots on PC3-PIP cells only.

The presence of CSS-Ab on the surface of PSMA+ (PC3-PIP cells) has been assessed also acquiring FE-SEM images of the cells (figure 3.11A and B) and confirmed with EDX analysis which show the presence of gold in the analyzed spot (figure 3.11 C).

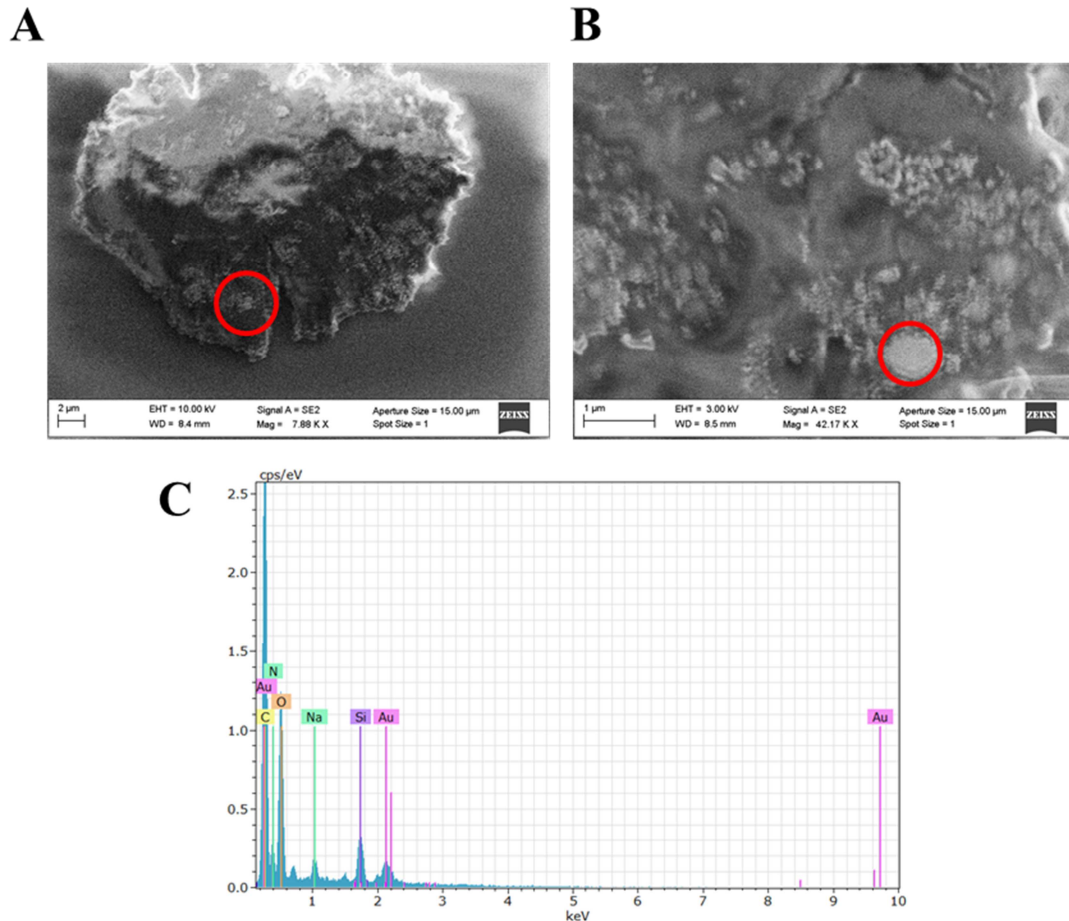


Figure 3.11 FE-SEM images of a PSMA+ (PC3-PIP) cell immunomagnetically sorted using CSS-Ab nanostructures (A) and its magnification (B) in correspondence of the red circle in (A). The red circle in (B) corresponds to CSS-Ab nanostructures as confirmed by EDX analysis on the spot (C) where clear Au signals are found.

The reproducibility and the efficiency of the CSS-Ab in immunosorting of cells were verified by repeating the experiments using a second batch of nanostructures. Flow cytometer analyses (figure 3.12) show the same affinity to PSMA antigen of the first batch.

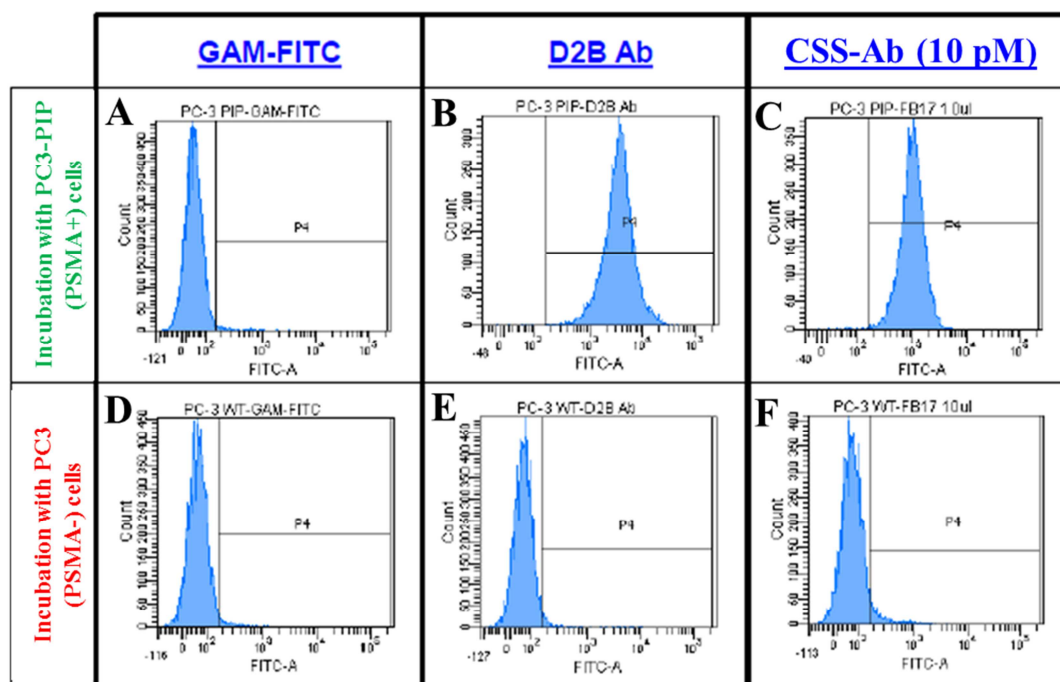


Figure 3.12 Flow cytometry analysis of PC3 PIP (PSMA+) in the upper part and of PC3 in the lower part. Cells are incubated only with GAM-FITC ((A) and (D)), pure D2B and then with GAM-FITC ((B) and (E)) and CSS-Ab at a concentration of 10 pM and then with GAM-FITC ((C) and (F)). Similarly to the first batch of CSS-Ab (which flow cytometry analysis is shown in figure 3.6) the data show that the second batch of CSS-Ab has an activity of D2B antibody similar to pure D2B and that the activity is specific for PSMA present on PC3PIP cells.

Results of immunomagnetic sorting with the new CSS-Ab are shown in figure 3.9 B. Comparing the two graphs in figure 3.9 A and 3.9 B one finds that the same trend is observed, with a low percentages of PSMA+ sorted cells for low concentrations of CSS-Ab nanostructures and the maximum (almost 100% of PSMA+ cells sorted) when the concentration is the largest explored 19.1 pM. The only difference is found in the percentage of PSMA- sorted cells which, in this last case, is found to be very low (<6%) for all concentrations. This suggests the presence of false positives for the PSMA- cell sorting with the first CSS-Ab nanostructures, probably due to accidental errors in the separation procedure.

The immunomagnetic sorting efficiency and specificity is comparable with that of commercial products. As an example, in figure 3.13 flow cytometry of Dynabeads® FlowComp™ Mouse CD4 Kit is reported from the vendor website.¹³ This kit is used, for example, for immunomagnetic separation of T cells type expressing the CD4

antigen. Flow cytometry show that 97.2% of T (CD4+) cells can be sorted using this commercial kit. However no information about non-specific cell sorting is given.

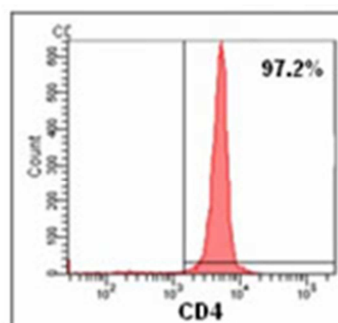


Figure 3.13 Flow cytometry of T (CD4+) cells using commercial antibody-functionalized beads show efficiency comparable with that of CSS-Ab nanostructures.¹³

The time required for sorting with the commercial beads is similar to that used with CSS-Ab (about ten minutes), although they are about ten times bigger than CSS-Ab. For beads with size comparable to CSS-Ab the vendor recommends separations with longer times.¹³ This shows that the immunomagnetic sorting with the CSS-Ab is very efficient.

Furthermore, the CSS-Ab, have other characteristics which make them a more powerful tool. In particular, thanks to their SERRS activity, CSS-Ab nanostructures can be used to perform imaging on single cells.

SERRS analysis on single cells

The SERRS property of the CSS-Ab nanostructures makes possible multiplexed analyses, namely the recording, in a single spectrum, of different SERRS signals that can be made to correspond to different antigens. This allows analyzing many antigens with only one immunomagnetic sorting. In this case different CSS-Ab nanostructures have to be functionalized with different antibodies and different dyes. The feasibility of applying CSS-Ab nanostructures in imaging sorted cells was verified by recording their SERRS spectra after the sorting procedure.

We deposited sorted PSMA+ (PC3-PIP) and PSMA- (PC3) cells on a glass slide and recorded the SERRS spectra of single cells looking, in particular, to the most intense band of crystal violet at 1618 cm^{-1} . Several hundred cells have been analyzed for each sample.

The signal of crystal violet is expected only for PSMA+ cells because they should have CSS-Ab particles on their structure (see figure 3.14).

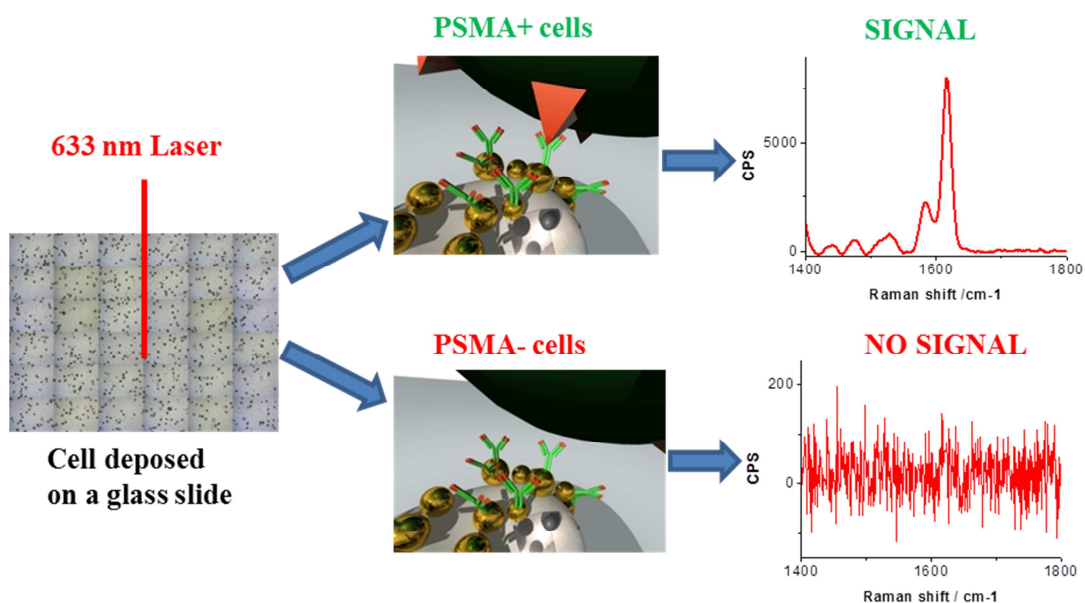


Figure 3.14 SERRS analysis of single cells: first PSMA+ and PSMA- sorted cells are deposited on a glass slide and the most intense signal of the .SERRS reporter is registered for each cell. The signals are observed where the CSS-Ab are present.

Results are shown in figure 3.15 A and B for the two batches of CSS-Ab together with the results recorded after the immunomagnetic sorting.

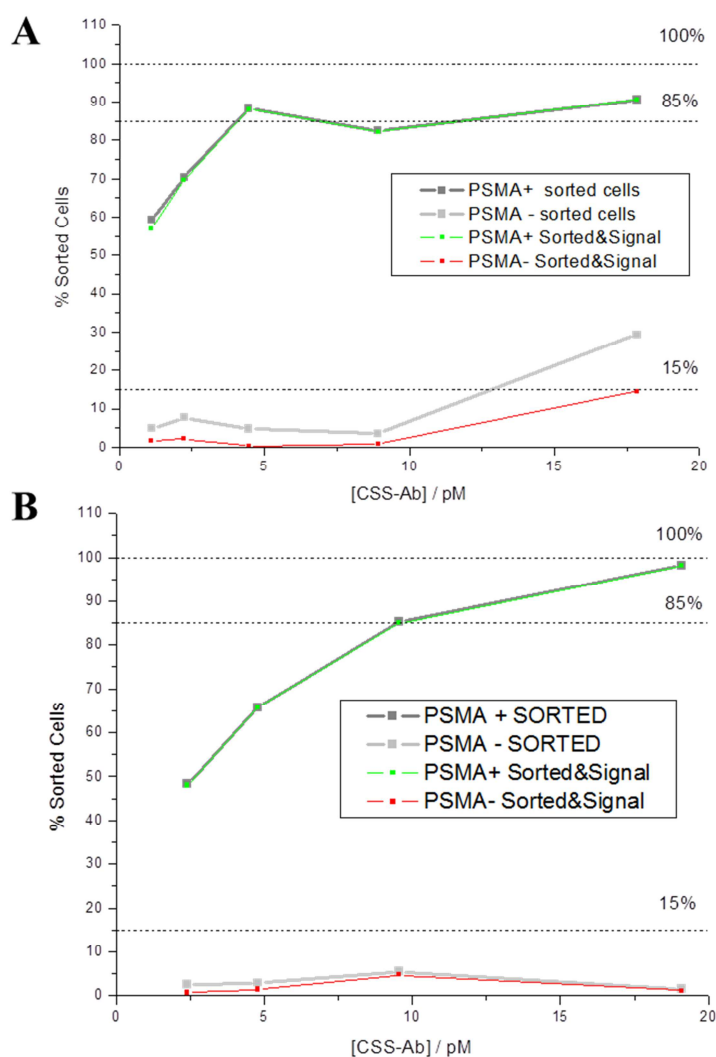


Figure 3.15 Sorted PSMA+ (PC3-PIP) and PSMA- (PC3) cells also with SERRS signals (green and red lines). For comparison, data from immunomagnetic sorting only are reported in both graphs (grey and light gray lines). (A) refers to the first batch of CSS-Ab as in figure 3.9A while (B) refers to the second batch as in figure 3.9B.

In both cases, the green line, which represents the percentage of PSMA+ cells that have been sorted and also show SERRS signal is superimposed to the grey lines representing data from immunosorting only. This means that all the sorted PSMA+ cells showed SERRS signal, as expected. In the case of PSMA- cells, the percentages of cells that also show SERRS signals (red lines in figure 3.15 A and B) is lower than the percentages of magnetically sorted cells. This is particularly evident in the first case (figure 3.15 A) where only a fraction of the sorted PSMA- present SERRS signal, in particular at the highest concentration. The presence of these sorted cells without SERRS signals only for the case of PSMA- cells, and considering that the

SERRS signals are very efficient, suggests that errors can be present in the immunomagnetic sorting, probably related to the pipetting of the cells which are not attracted by the magnet. This is also evident from the experiment done with the second batch of CSS-Ab, where this problem is not present.

The results show, however, that the SERRS signals of CSS-Ab nanostructures are observed also after the sorting procedures and that the positive cells can be identified with the SERRS analysis.

Multiplexed analyses have not been performed at the moment. However, as proof of principle we synthesized other CSS nanostructures (without antibodies) embedding different dyes in the shell. In figure 3.16 Raman SERS spectra of these nanostructures are reported, evidencing that the spectra of different dyes are easily distinguishable between them. This allows to foresee that the use of CSS-Ab also for a multiplexed analysis in multiplexing mode, which is not possible with commercial magnetic beads and a single immunomagnetic sorting.

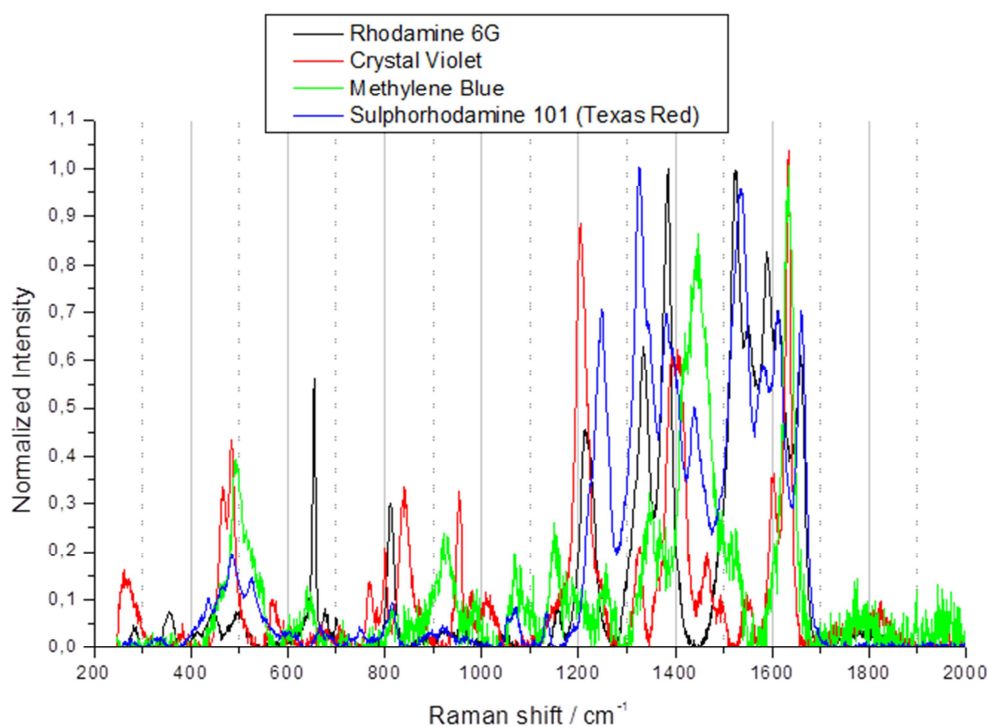


Figure 3.16 SERRS spectra of CSS nanostructures with different dyes (Rhodamine 6G, Crystal Violet, Methylene Blue and Sulphorhodamine 101) embedded in the silica shell. Spectra are recorded exciting at 633 nm and normalized to their most intense peak.

Photothermal treatment of cancer cells

In this section the application of CSS-Ab for photothermal treatment of cancer cells is reported. As explained in the introductory section, photothermal effect is due to the heat generated by gold nanoparticles irradiated in resonance with their localized surface plasmon (LSPR). CSS-Ab nanostructures have the LSPR maximum absorption in the spectral range of 600-700 nm, therefore, the cells were irradiated using a 647 nm continuous laser wavelength. Other laser parameters to be taken in account in photothermal experiments are the irradiation time and the power density (W cm^{-2}). The experiments were carried out by varying the irradiation time and maintaining constant the power density at values similar to those found in literature.¹⁴⁻¹⁸

Before performing irradiation of the cells the temperature increase following the irradiation was verified embedding the CSS-Ab in an agarose hydrogel. It is in fact known that hydrogels, with their high water content, can simulate a biological environment.¹⁹ Results of the experiments are reported below, and they show a notable increase of temperature.

Photothermal treatment experiments on cells have been performed using both PSMA+ (PC3 PIP) and PSMA- (PC3) cells with four different kinds of experiments. First, the effect of laser irradiation on cells non incubated with CSS-Ab verified only the effect of the laser on cells viability. In a second experiment PSMA+ cells were incubated with the CSS-Ab and the cell viability was evaluated at different irradiation times and at a fixed power density.

In the third experiment, a real situation was simulated using PSMA+ or PSMA- cells incubated with CSS-Ab to evaluate the photothermal effect in a situation as close as possible to a real one.

In the fourth experiment the so called “bystander effect”, namely the possibility that healthy non-targeted cells dies because of their proximity to targeted tumour cells, was evaluated being a phenomenon of particular interest for immunologists. One should recall that the bystander effect can derive both from heat released to nearby cells or because of the release of specific apoptotic/necrotic signals by dying cells which trigger the death mechanism of neighboring cells.^{20, 21} It is not the purpose of this thesis to investigate the importance of these mechanisms, and experiments were

done only to evaluate the presence of the effect. All experiments were done with a fixed exposure time.

Experimental section

Laser setup for photothermal experiments

Laser irradiation of cells and hydrogels were performed with a continuous Ar⁺/Kr⁺ mixed gas laser (Coherent, Innova 70) at 647.1 nm.

Hydrogel irradiation was performed using a beam with 5 mm diameter and 1.5 W cm⁻² power density. Cells irradiation was performed using a focused beam with ca. 1 mm diameter. The beam size have been measured by a Laser Beam Analyzer system (Spiricon) equipped with a CCD camera with 1600 x 1200 pixels and 4.4 μm pixel pitch. Power densities used in irradiations are: 38 W cm⁻² for irradiation of non-treated cells, 39 W cm⁻² for irradiation of CSS-Ab loaded PSMA+ (PC3-PIP) cells varying time, 36 W cm⁻² for irradiation of adherent cells and 39 W cm⁻² for irradiation in bystander effect experiment.

Preparation of CS and CSS nanostructures loaded agarose hydrogel

For hydrogel preparation we used a 1% w/w aqueous solution of agarose (Sigma-Aldrich, low EEO). The solution was heated until dissolution of agarose and then CS or CSS nanostructures were added to a final concentration of 20 pM. The solution was then cooled to allow hydrogel formation. Hydrogels were then cutted in discs with 1 cm diameter and 0.5 cm height and stored in dd water solution until their use. During laser irradiation, all hydrogels are maintained at 37°C in a home-made thermostatic chamber. Hydrogel temperature during irradiation is monitored every minute for 10 minutes using a FLIR E5 thermocamera.

Cell culture and viability

Cell culture were conducted as reported above in the corresponding part in the “Immunomagnetic sorting of cancer cells” section. Incubation and sample preparation depend on the experiment (see below). Cell viability is assessed with trypan blue assay performing the test at least 1.30 h after irradiation.

Irradiation of cells not incubated with CSS-Ab

PSMA+ (PC3-PIP) cells not incubated with CSS-Ab were made to adhere to 3.5 cm diameter wells containing RPMI 160 culture medium. Cells were irradiated for 5.00, 10.00 and 15.00 minutes and viability was evaluated right after irradiation (1.30 h after last irradiation), after 24 h and after 48 h. Every irradiation has been repeated 9 times to obtain statistically reliable data. Viability of control samples (non irradiated cells) was recorded before the beginning of irradiations, right after the last irradiation, after 24 h and after 48 h.

Irradiation times of PSMA+ (PC3-PIP) cells

PSMA+ (PC3-PIP) cells were incubated with CSS-Ab nanostructures at a concentration of 19.1 pM, for 1h at 4°C in the presence of 5% Bovine Serum Albumin (BSA) to block non-specific protein interactions. After incubation time cells were magnetically sorted and made to adhere in 3.5 cm diameter wells containing RPMI culture medium. Cells were irradiated for 30 sec, 1.30 min, 3.00 min, 5.00 min, 10.00 min and 15.00 min. Every irradiation has been repeated 6 times to obtain statistically reliable data. Viability of all samples has been evaluated at least 1.30 h after irradiation. Viability of control samples (cells incubated with CSS-Ab but non-irradiated) has been recorded before the beginning of irradiations and after the last irradiation.

Irradiation of adherent cells

PSMA+ (PC3-PIP) cells were made to adhere in 3.5 cm diameter wells containing RPMI culture medium. The same was done for PSMA- (PC3) cells. CSS-Ab nanostructures were then diluted in the RPMI medium inside the wells to a final concentration of 19.1 pM. Cells in RPMI medium+CSS-Ab were then incubated at 37°C for 30 minutes. After incubation time the liquid in the wells was removed and replaced with fresh culture medium. Several washes were performed to remove every CSS-Ab structure not bounded to cells. Irradiation on both PSMA+ and PSMA- cells was performed for 2.30 min, 5.00 min and 10.00 min, 6 times for every experiment. Viability for all samples has been evaluated at least 1.30 h after irradiation. Viability of control samples, consisting of PSMA+ or PSMA- cells incubated with CSS-Ab but non-irradiated, was recorded before the beginning of irradiations and at the end.

Bystander effect

A mix of PSMA+ (PC3-PIP) and PSMA- (PC3) cells were made to adhere in 3.5 cm diameter wells containing RPMI culture medium and then CSS-Ab nanostructures were added to a final concentration of 19.1 pM. Cells were then incubated at 37°C for 30 minutes. After the incubation time the liquid in the wells were removed and replaced with fresh culture medium. Several washes were performed to remove every CSS-Ab structure not bounded to cells. Irradiation of cells was performed for 2.00 min, 5.00 min and 10.00 min. The experiments were repeated 3 times for every experiment. Viability for all samples has been evaluated at least 1.30 h after irradiation. Viability of control samples, consisting of the same cells mix incubated with CSS-Ab but non-irradiated, was recorded before the beginning of irradiations and at the end. To determine the percentages of PSMA+ (PC3-PIP) and PSMA- (PC3) cells present in the wells, SERRS analysis of single cells was performed. The percentage of spectra in which crystal violet signal is found with respect to those in which no signal was present was assumed to be equal to the percentage of PSMA+ (PC3-PIP) over PSMA- (PC3) cells. Several hundreds of cells have been analyzed. SERRS measurements were performed directly on the wells containing culture medium using 633 nm laser, with 20× objective and a power of 1.54 mW.

Results

Hydrogel

UV-Visible spectra of CS and CSS loaded hydrogels compared with those of CS and CSS in solution do not show remarkable differences (Figure 3.17), meaning that structural integrity of particles is maintained when they are included in hydrogels.

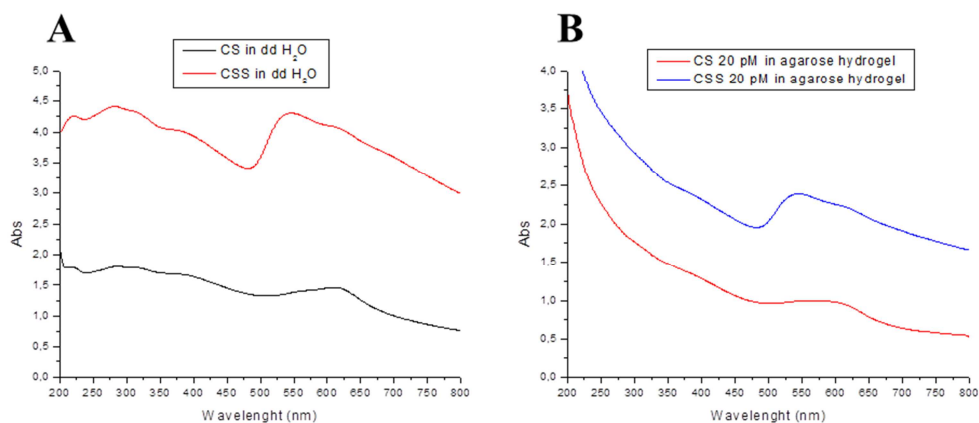


Figure 3.17 (A) UV-Vis spectra of aqueous solution of CS and CSS used for evaluation of photothermal effect. (B) UV-Vis spectra of CS and CSS loaded hydrogel.

Hydrogels were irradiated with 647 nm laser line for 10 minutes recording their temperature every minute. Measurements are reported in figure 3.18 and show a rapid increase of temperature for hydrogel containing CSS nanostructures (14°C in the first minute) while for those containing CS the increase was only of the 4-5°C. Temperature of CSS loaded hydrogel was increased of about 20°C in 10 minutes of irradiation while those with CS increased their temperature of only 4-5°C. This confirms that the presence of AuNPs is essential and that photothermal effect is efficient.

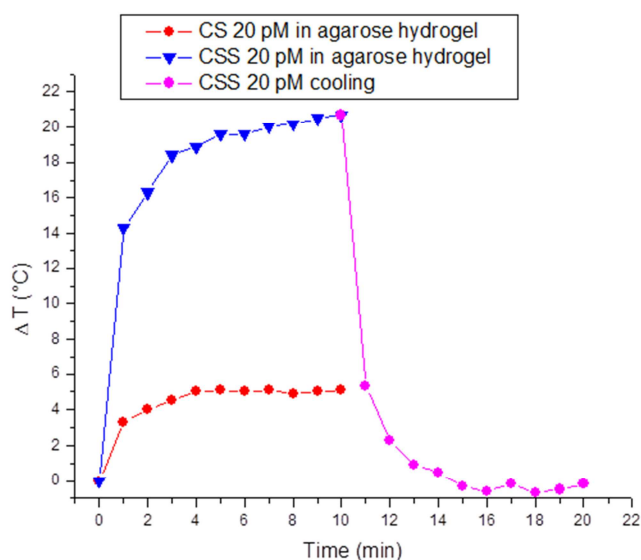


Figure 3.18 Temperature of CS (red) and CSS (blue and violet) loaded hydrogels irradiated for 10 minutes with a 647 nm laser line at a power density of 1.5 W cm^{-2} .

In figure 3.19 thermal images of hydrogels at the beginning and at the end of laser irradiation are reported.

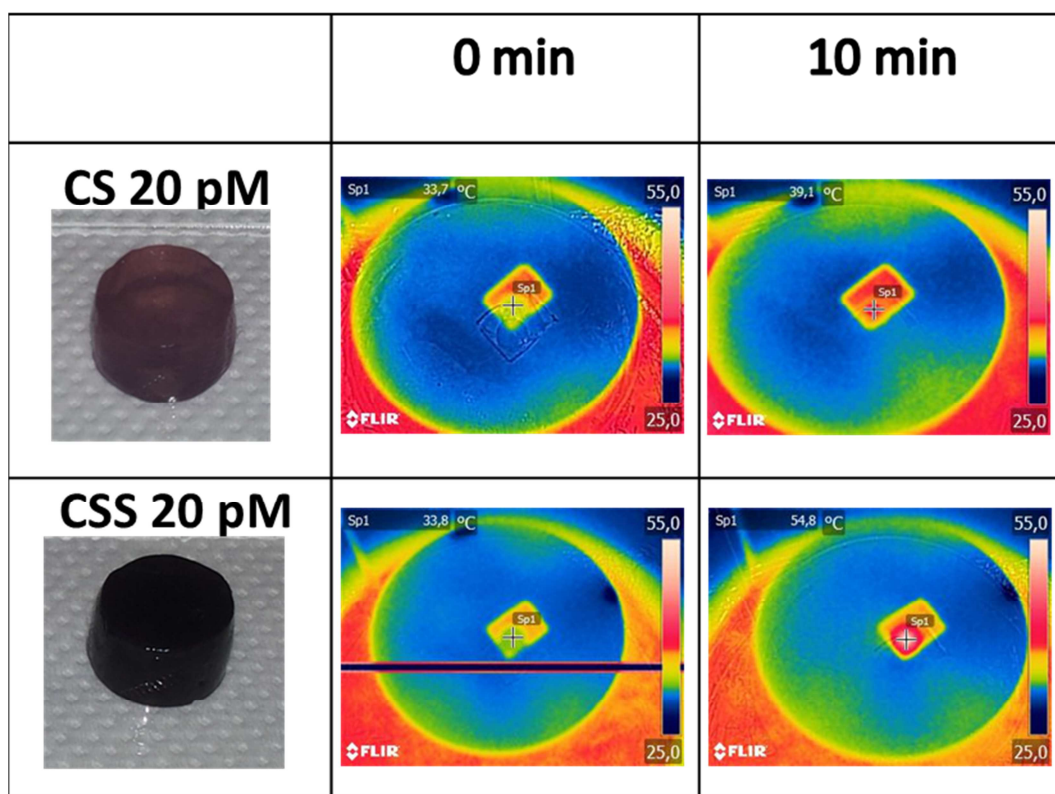


Figure 3.19 Hydrogels loaded with CS and CSS (photos on the left) and thermal images registered at the beginning and at the end of laser irradiation.

Irradiation of PSMA+ (PC3PIP) cells not incubated with CSS-Ab

This experiment shows the effect of the laser source on cell viability.

Uv-Visible spectra of the culture medium show that absorption at 647 nm was absent (Figure 3.20).

Histogram in figure 3.21 shows that after 5.00, 10.00 and 15.00 minutes of irradiation, the viability of cells is close to 100% and comparable to that of control samples (non-irradiated). No effect is observed also after 24 and 48 hour from irradiation. These results confirm that laser light has no effect on cell viability.

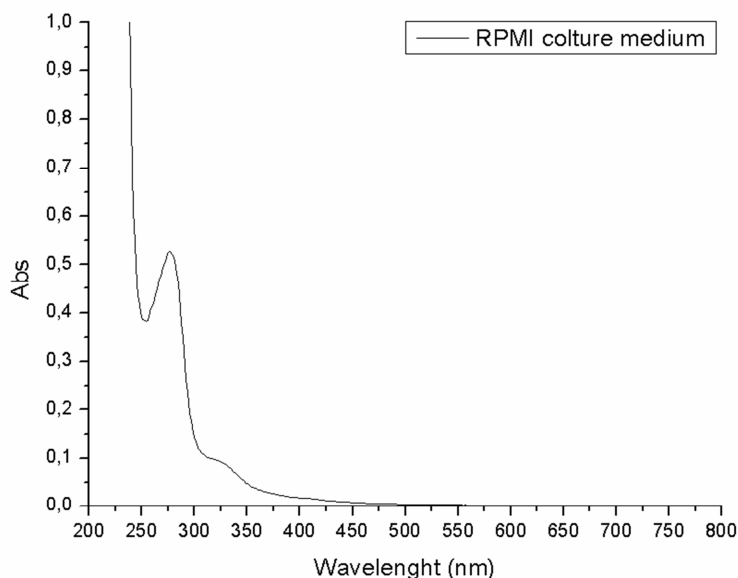


Figure 3.20 UV-Visible spectra of RPMI culture medium used during laser irradiation of PSMA+ (PC3-PIP) and PSMA- (PC3) cells. Spectra show no absorption at 647 nm, the wavelength used in photothermal treatment of cancer cells.

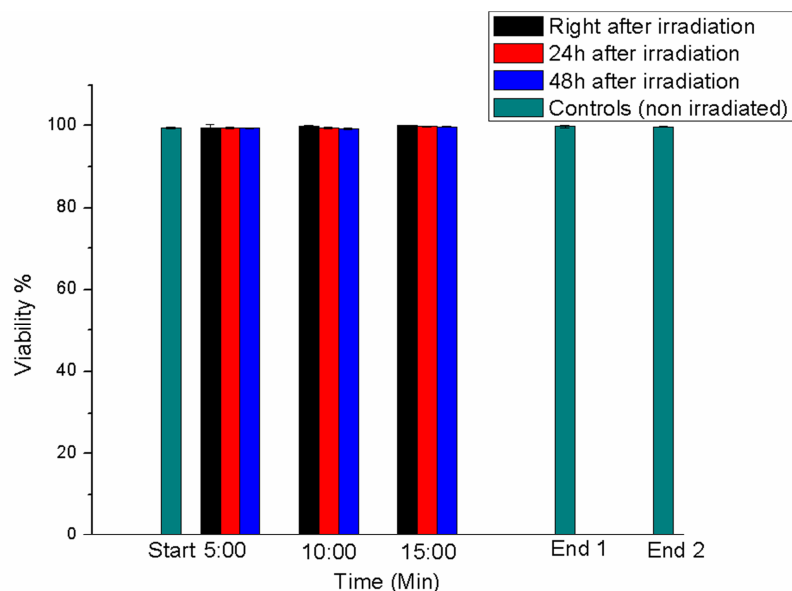


Figure 3.21 Viability of PSMA+ (PC3-PIP) cells non incubated with CSS-Ab nanostructures and irradiated for 5.00, 10.00 and 15.00 minutes with a 647 nm laser line at 38 W cm^{-2} . Viability is evaluated right after irradiation (black bars), after 24h from irradiation (red bars) and after 48h (blue bars). Viability of control samples (non-irradiated cells, green bars) is evaluated at the beginning of experiment (Start), after 24h (End 1) and after 48h (End 2).

Effect of irradiation time on PSMA+ (PC3-PIP) cells

Cells were magnetically sorted and made to adhere to wells in the presence of culture medium and then irradiated for 30 sec, 1.30, 3.00, 5.00, 10.00 and 15.00 minutes.

Histogram in figure 3.22 shows the PSMA+ (PC3-PIP) cells viability as a function of irradiation time. Viability rapidly decreases within 3 minutes of irradiation and reaches almost 0% for cell irradiated from 5 minutes to 15 minutes.

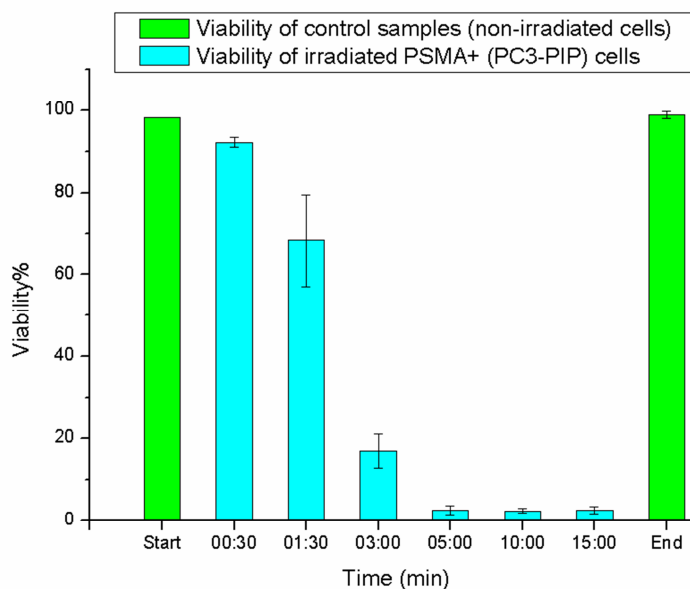


Figure 3.22 Viability PSMA+ (PC3-PIP) cells incubated with CSS-Ab as a function of irradiation time with a 647 nm laser line at 39 W cm^{-2} (cyan bars). Control samples (green bars) are cells incubated but not irradiated.

Results show great efficiency of the photothermal process on the viability of cells since also short irradiation times were sufficient for dramatic effect on cells viability. Looking at viability of control samples, one finds that treatment with CSS-Ab does not affect cells viability.

Photothermal effect on adherent cell

The difference between this experiment and the previous one is that now adherent cells are in the wells and CSS-Ab are inoculated directly in the culture medium. This procedure simulates the interaction that there would be between a tissue, whose cells are “static”, and CSS-Ab nanostructures that reach the tissue through extravasation. Clearly, in this case magnetic properties of particles were not necessary. To simulate better a biological environment, incubation was performed at 37°C . After incubation time (30 min) the liquid was removed and replaced with fresh culture medium.

Irradiation was performed on both PSMA+ (PC3-PIP) and PSMA- (PC3) cells for 2.30 min, 5.00 min and 10.00 min.

Results in figure 3.23 shows a drastic decrease of PSMA+ (PC3) cells viability only after 2.30 minutes of irradiation, with values falling from 95% to less than 10%. Viability slightly decreases as irradiation time is prolonged, reaching almost 2-3 % after 10 minutes of irradiation. Viability of irradiated PSMA- (PC3) cells remains practically unaltered and comparable with that of controls for all irradiation time. This, again, confirms the high targeting specificity of CSS-Ab nanostructures against PSMA+ cells only.

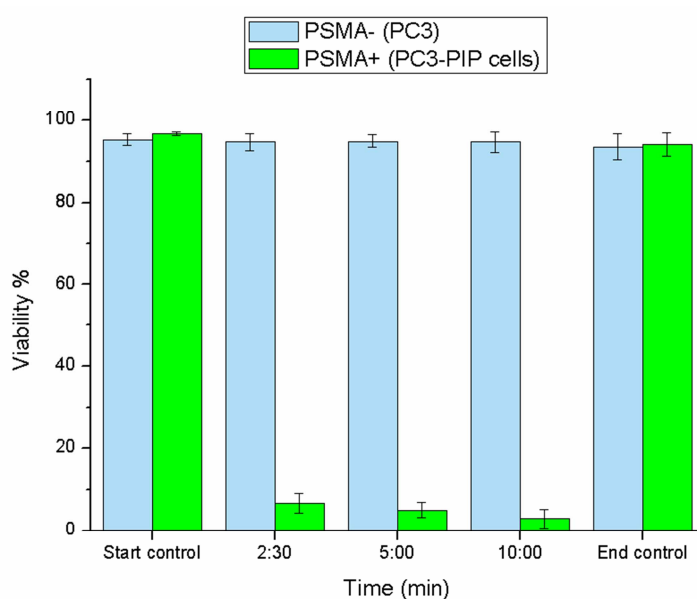


Figure 3.23 Cell viability after irradiation of PSMA+ (PC3-PIP, green bars) and PSMA- (PC3, cyan bars) adherent cells. Both cells type are incubated with CSS-Ab nanostructures and irradiated for 2.30, 5.00 and 10.00 minutes with a 647 nm laser line at 36 W cm^{-2} .

Figure 3.24 shows two images of PSMA+ and PSMA- cells irradiated for 5 minutes. Thanks to trypan blue staining, one finds that cells death occurred only in sample containing PSMA+ cells where they are irradiated by the laser spot.

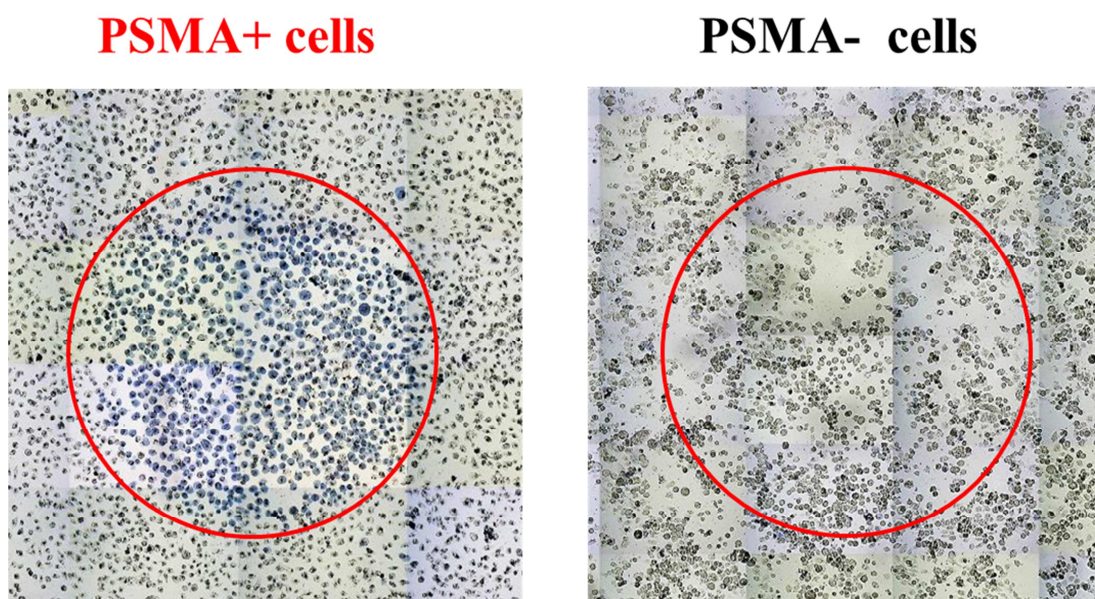


Figure 3.24 Two images of irradiated area taken with optical microscope. Red circles delimit irradiated area. As evidenced by trypan blue assay, cells death is present only for PSMA+ cells (left) and not for PSMA- cells (right).

Evaluation of bystander effect

The evaluation of the bystander effect was performed by irradiating a mix of PSMA+ (PC3-PIP) and PSMA- (PC3) cells. The purpose is to assess if dying cells stimulates apoptosis mechanism also in surrounding cells. Histogram in figure 3.25 shows that the viability of PSMA- cells incubated with CSS-Ab and then irradiated remains at high levels, comparable with those PSMA- cells that have not been irradiated. For this reason, when the two cell types are mixed, incubated with CSS-Ab nanostructures and irradiated, we expect the death of PSMA+ cells only while PSMA- cells should not be affected. The evaluation of the bystander effect is important because in a real situation tumoral cells can be close to healthy cells, so one has to consider the damaging of healthy cells by surrounding cancer cells undergoing photothermal treatment.

Mixed cells were incubated with CSS-Ab using the same procedure used for adherent cells. Since it is difficult to distinguish the two cell types with a microscope analysis, SERRS signals were used to determine the percentage of PSMA+ (PC3-PIP) and PSMA- (PC3) cells present in the sample, considering that only PSMA+ cells show these signals.

Histogram in figure 3.25 shows viability of mixed cells at three different irradiation times (2.30, 5.00 and 10.00 minutes). The red dashed line represents the percentage of PSMA- cells.

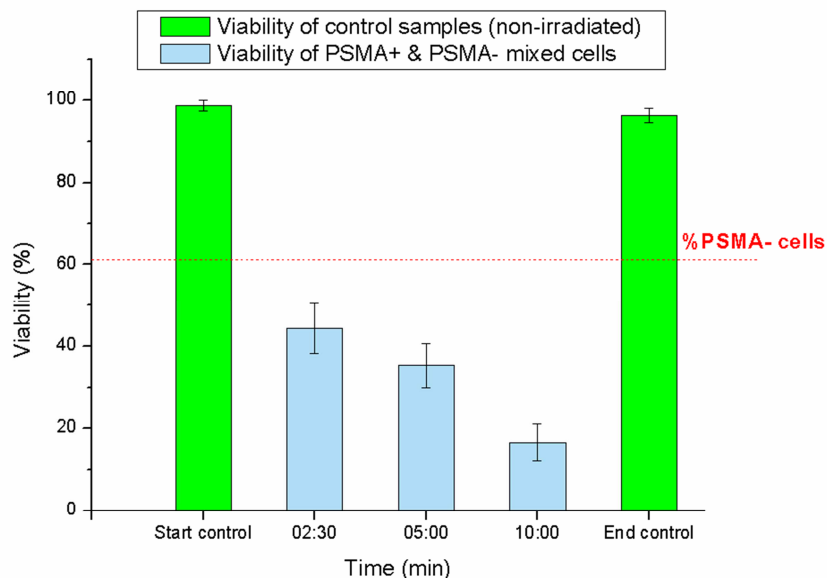


Figure 3.25 Viability after irradiation of PSMA+ (PC3-PIP) and PSMA- (PC3) mixed cells (cyan bars) and non-irradiated controls (green bars). Cells type are incubated with CSS-Ab nanostructures and irradiated for 2.30, 5.00 and 10.00 minutes with a 647 nm laser line at 39 W cm^{-2} . A viability value below the percentage of PSMA- cells means that the presence of bystander effect is present.

Results show that for all irradiation times viability values are below the percentage of PSMA- cells. This suggests that the bystander effect is present. In fact, if the system behaves as seen for adherent cells, only PSMA+ cells should have died and viability values should not have fallen below percentage of PSMA- cells. These results show that also PSMA- cells died during irradiation. As explained at the beginning of this section, the mechanism of the bystander effect in photothermal treatment is not yet well understood. Our preliminary study suggests that the effect exists, but more work is necessary to confirm and to explain its presence.

From core-shell-satellite to core-shell-shell: tuning the plasmon to NIR

In the previous section the efficiency of CSS-Ab nanostructures in photothermal treatment of prostatic cancer cells was shown. All experiments were performed using the 647 nm laser line but, recalling the dedicated section in the introduction, the use of a laser with a wavelength more shifted to the NIR spectral region, would be more appropriate because of its deeper penetration through tissues. The LSPR of nanostructured materials determines which laser line has to be used to exploit the photothermal effect. Since CSS-Ab have their LSPR in the range 600-700 nm spectral range, one would like to use nanostructures with absorption more shifted in the NIR region. Therefore, we tried to modify the optical properties of CSS nanostructures acting on the external silica shell. It is known, in fact, that particles with a continuous gold shell on a silica shell may show LSPR in NIR region, depending on shell characteristics, in particular its thickness with respect to the nanostructure diameter.

In this section the preliminary results on the synthesis of FeO_xNPs@dye-doped Silica@Au core-shell-shell nanostructures are presented.

FeO_xNPs@dye-doped silica core-shell (CS) nanostructures are synthesized and gold seeds consisting of AuNPs with 2-3 nm radius are conjugated to silica shell surface thanks to the presence of -SH groups on silica shell. The last step involves reduction of gold ions on silica shell using sodium borohydride as reductant.

Methods

The synthesis of FeO_xNP@dye-doped Silica core shell (CS) nanostructures proceeds as described in the section “Assembling of antibody functionalized core-shell-satellite (CSS-Ab) nanostructures”. After the synthesis, CS nanostructures were dispersed in PBS.

Synthesis of Au seeds

Gold nanoparticles obtained by LASiS using the same procedure reported in chapter 2 were fragmented using 532 nm pulsed laser (10 Hz) with a fluence of 260 mJ/cm². Before performing fragmentation, TWEEN 20 (Sigma) was added to AuNPs solution

to a final concentration of 0.5% v/v to stabilize the fragmented nanoparticles. After 30 minutes, fragmentation was stopped and the solution was centrifuged at 30000 g for 15 minutes. After centrifugation, the supernatant solution contains gold nanoparticles with 2-3 nm radius. Their average diameter was obtained through Mie-Gans fitting of the UV-Visible spectra and confirmed by TEM measurements (see figure 3.26).

Synthesis of CS-Seed

Gold seeds were added to a CS nanostructures solution (100 pM) to a final concentration of $5 \cdot 10^{-7}$ M. The solution was placed in a sonicating bath for 1h to promote seeds conjugation to silica shell. After sonication, CS-Seeds were purified from unconjugated seeds through magnetic separation.

Synthesis of core-shell-shell nanostructures

First a solution was prepared mixing 500 μ L of $\text{HAuCl}_4 \cdot x\text{H}_2\text{O}$ (0.009 M) with 2 mL of K_2CO_3 (0.011 M). The solution was then stirred for 15 minutes and then CS-Seeds nanostructures were added to a final concentration of $9 \cdot 10^{-11}$ M. The solution was stirred in the dark for 24 hours (dark aging). After dark aging, 68 μ L of a NaBH_4 solution (0.05 M) were slowly added to aged solution under stirring. Nanostructures were cleaned from reagents through magnetic separation and washing. Molar proportions for the reagents are HAuCl_4 :CS-Seed: NaBH_4 =1:1.2 $\cdot 10^{-9}$:0.8.

Results

TEM image of AuNPs with 2-3 nm radius conjugated to CS shell is reported in figure 3.27 where the seeds are observable as smaller dark spots.

The UV-Visible spectra of these core-shell-shell nanostructures is reported in figure 3.28 (black spectra) and compared with that of initial CS-seed nanostructures (violet spectra). Comparing the two spectra, one can notice a red-shift of the plasmonic band from 600-650 nm to 700-750 nm. This variation of LSPR position shows that morphological changes occurred in the structure.

A TEM image of a representative nanostructure after the gold salt reduction is reported in figure 3.29. One notes that, although much more small AuNPs are densely packed on the surface, with respect to those observed for the CS-Seed

nanostructures, the formation of a continuous shell is not obtained. The presence of a continuous shell would have shifted the spectrum more to the NIR spectral region. Clearly, further efforts must be done to control the morphology of CS-Seed nanostructures for obtaining a better result.

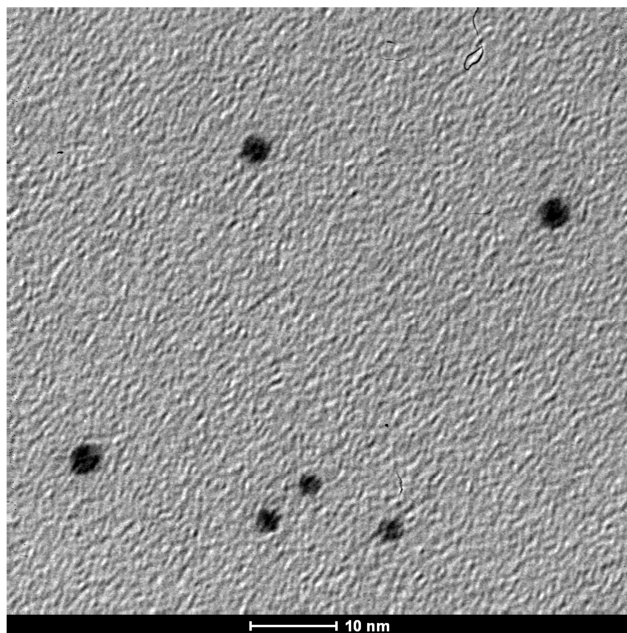


Figure 3.26 TEM images of AuNPs with 2-3 nm radius obtained with the fragmentation of gold nanoparticles with 10 nm radius. Fragmented AuNPs are used as seed.

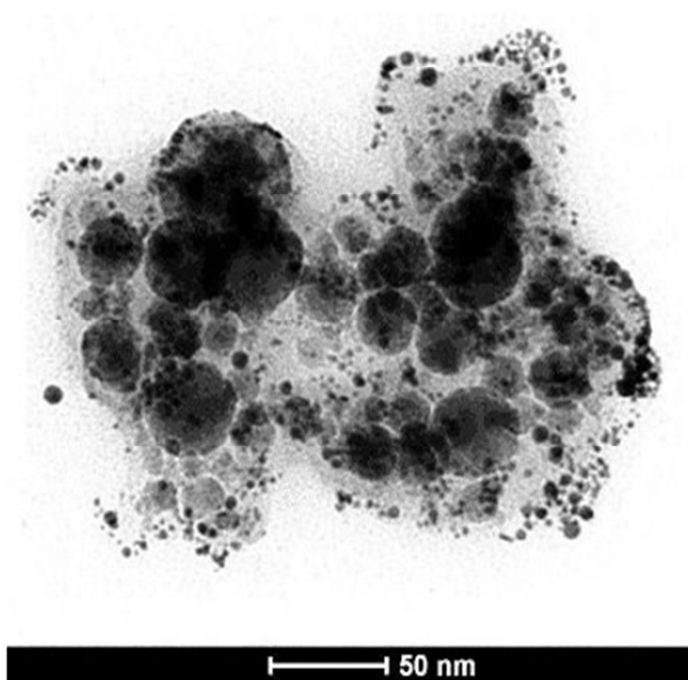


Figure 3.27 TEM micrograph of CS-Seed nanostructures.

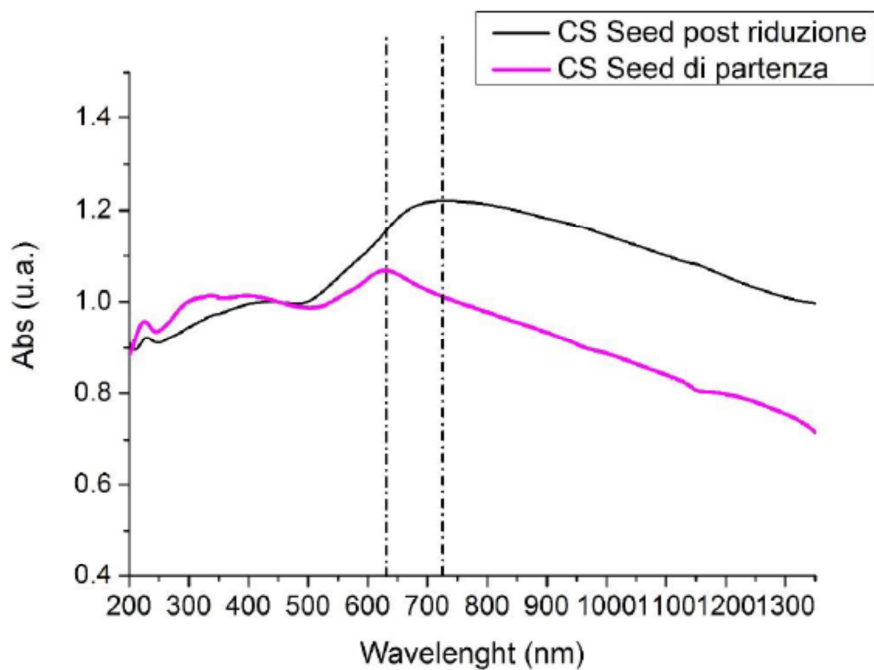


Figure 3.28 UV-Visible-NIR spectra of CS-seed nanostructures before (violet spectra) and after (black spectra) the reduction of gold ions. A red-shift of the plasmon band from 600-650 nm to 700-750 nm is observable.

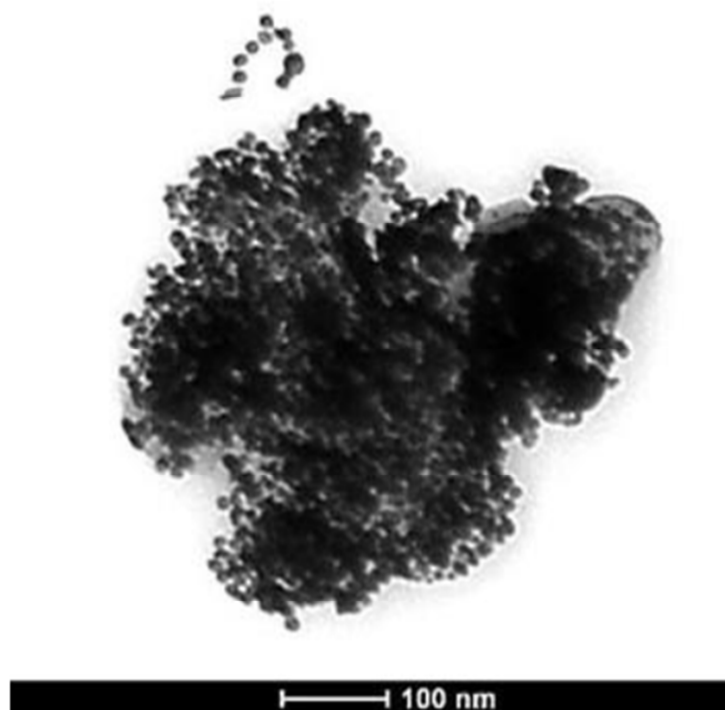


Figure 3.29 TEM micrograph of CS-Seed after the reduction of gold ions.

Conclusion

In this chapter the synthesis, characterization and *in vitro* application of magneto-plasmonic core-shell-satellite (CSS) nanostructures made of an iron oxide core surrounded by a dye-doped silica shell and gold nanoparticles as satellites are reported.

CSS nanostructures showed good magnetic and SERRS properties, suitable for their use in nanomedicine. CSS nanostructures were functionalized with D2B antibody (CSS-Ab), specific for the identification of the PSMA antigen, which is overexpressed by prostatic cancer cells. Immunomagnetic sorting efficiency of CSS-Ab nanostructures was evaluated showing specificity, accuracy and sensitivity close to 100%. The possibility to perform SERRS analysis at single cell level was also assessed showing promising results for CSS application in multiplexed analysis.

CSS-Ab nanostructures showed also good photothermal effect if irradiated with a 647 nm laser and their efficiency in photothermal treatment of cancer cell was evaluated. First, irradiation of PSMA+ (PC3-PIP) cells incubated with CSS-Ab at different times was performed. Low viability was observed after only 3 minutes of irradiation. In a second experiment adherent cells, which simulate 'static' cells found in a tissue, were used. Also in this case the viability for PSMA+ (PC3-PIP) cells were found very low after only 2,30 min of irradiation whereas, thanks to the CSS-Ab specificity, PSMA- (PC3) cells were practically unaffected.

In the last part the presence of the bystander effect was evaluated irradiating sample of mixed PSMA+ and PSMA- cell. The preliminary results show that bystander effect is present.

Finally, the morphological features of the CSS nanostructures were considered in order to tune their LSPR in the NIR region. Results show that the plasmon tuning is possible, but more experiments are needed to obtain a controlled shift of the plasmonic resonances in the NIR.

The nanostructures presented in this chapter can be considered a theranostic agent because of their possible use for diagnosis, exploiting the magnetic separation and the SERRS effect, and for therapy using the photothermal effect.

Future perspective for these nanostructures concerns the evaluation of their use in multiplexed analysis for diagnosis, and, for therapy, the use of magnetotherapy,

Chapter 3

namely of the generation of heat with variable magnetic field, together with phototherapy.

References

- (1) Verma, A.; Stellacci, F. Effect of surface properties on nanoparticle–cell interactions, *Small* **2010**, *6*, 12-21.
- (2) Amendola, V.; Riello, P.; Polizzi, S.; Fiameni, S.; Innocenti, C.; Sangregorio, C.; Meneghetti, M. Magnetic iron oxide nanoparticles with tunable size and free surface obtained via a “green” approach based on laser irradiation in water, *J Mater Chem* **2011**, *21*, 18665-18673.
- (3) Amendola, V.; Meneghetti, M.; Granozzi, G.; Agnoli, S.; Polizzi, S.; Riello, P.; Boscaini, A.; Anselmi, C.; Fracasso, G.; Colombatti, M. Top-down synthesis of multifunctional iron oxide nanoparticles for macrophage labelling and manipulation, *J Mater Chem* **2011**, *21*, 3803-3813.
- (4) Stöber, W.; Fink, A.; Bohn, E. Controlled growth of monodisperse silica spheres in the micron size range, *J. Colloid Interface Sci.* **1968**, *26*, 62-69.
- (5) Westcott, S. L.; Oldenburg, S. J.; Lee, T. R.; Halas, N. J. Formation and adsorption of clusters of gold nanoparticles onto functionalized silica nanoparticle surfaces, *Langmuir* **1998**, *14*, 5396-5401.
- (6) Dishon, M.; Zohar, O.; Sivan, U. From repulsion to attraction and back to repulsion: the effect of NaCl, KCl, and CsCl on the force between silica surfaces in aqueous solution, *Langmuir* **2009**, *25*, 2831-2836.
- (7) Meneghetti, M.; Scarsi, A.; Litt, L.; Marcolongo, G.; Amendola, V.; Gobbo, M.; Di Chio, M.; Boscaini, A.; Fracasso, G.; Colombatti, M. Plasmonic Nanostructures for SERRS Multiplexed Identification of Tumor-Associated Antigens, *Small* **2012**, *8*, 3733-3738.
- (8) Riener, C. K.; Kada, G.; Gruber, H. J. Quick measurement of protein sulfhydryls with Ellman's reagent and with 4, 4'-dithiodipyridine, *Anal Bioanal Chem*, **2002**, *373*, 266-276.
- (9) Bertorelle, F.; Ceccarello, M.; Pinto, M.; Fracasso, G.; Badocco, D.; Amendola, V.; Pastore, P.; Colombatti, M.; Meneghetti, M. Efficient AuFeO_x Nanoclusters of Laser-Ablated Nanoparticles in Water for Cells Guiding and Surface-Enhanced Resonance Raman Scattering Imaging, *J Phys Chem C* **2014**, *118*, 14534-14541.
- (10) Tykvart, J.; Navrátil, V.; Sedlák, F.; Corey, E.; Colombatti, M.; Fracasso, G.; Koukolík, F.; Bařinka, C.; Šácha, P.; Konvalinka, J. Comparative analysis of monoclonal antibodies against prostate-specific membrane antigen (PSMA), *Prostate* **2014**, *74*, 1674-1690.

- (11) Saha, B.; Evers, T. H.; Prins, M. W. How antibody surface coverage on nanoparticles determines the activity and kinetics of antigen capturing for biosensing, *Anal. Chem.* **2014**, *86*, 8158-8166.
- (12) Ghosh, A.; Wang, X.; Klein, E.; Heston, W. D. Novel role of prostate-specific membrane antigen in suppressing prostate cancer invasiveness, *Cancer Res.* **2005**, *65*, 727-731.
- (13) Thermofisher **Dynabeads® FlowComp™ Mouse CD4 Kit**. <https://www.thermofisher.com/order/catalog/product/11461D?ICID=search-product> (accessed 09/29, 2016).
- (14) Huang, X.; El-Sayed, I. H.; Qian, W.; El-Sayed, M. A. Cancer cell imaging and photothermal therapy in the near-infrared region by using gold nanorods, *J. Am. Chem. Soc.* **2006**, *128*, 2115-2120.
- (15) Huang, X.; Jain, P. K.; El-Sayed, I. H.; El-Sayed, M. A. Determination of the minimum temperature required for selective photothermal destruction of cancer cells with the use of immunotargeted gold nanoparticles, *Photochem. Photobiol.* **2006**, *82*, 412-417.
- (16) Huang, X.; Jain, P. K.; El-Sayed, I. H.; El-Sayed, M. A. Plasmonic photothermal therapy (PPTT) using gold nanoparticles, *Laser Med Sci*, **2008**, *23*, 217-228.
- (17) Huang, X.; El-Sayed, M. A. Plasmonic photo-thermal therapy (PPTT), *Alexandria Journal of Medicine* **2011**, *47*, 1-9.
- (18) El-Sayed, I. H.; Huang, X.; El-Sayed, M. A. Selective laser photo-thermal therapy of epithelial carcinoma using anti-EGFR antibody conjugated gold nanoparticles, *Cancer Lett.* **2006**, *239*, 129-135.
- (19) Hoskins, C.; Min, Y.; Gueorguieva, M.; McDougall, C.; Volovick, A.; Prentice, P.; Wang, Z.; Melzer, A.; Cuschieri, A.; Wang, L. Hybrid gold-iron oxide nanoparticles as a multifunctional platform for biomedical application, *J nanobiotechnology* **2012**, *10*, 1.
- (20) Purschke, M.; Laubach, H.; Anderson, R. R.; Manstein, D. Thermal injury causes DNA damage and lethality in unheated surrounding cells: active thermal bystander effect, *J. Invest. Dermatol.* **2010**, *130*, 86-92.
- (21) Melamed, J. R.; Edelstein, R. S.; Day, E. S. Elucidating the fundamental mechanisms of cell death triggered by photothermal therapy, *ACS nano* **2015**, *9*, 6-11.

Conclusion

In the overall nanotechnology panorama, nanostructured materials are emerging as realistic and possible solution to problems in nanomedicine. In the introductory section an overview of nanostructured materials for application in nanomedicine was given, with particular attention for those made of gold and iron oxide due to their useful optical and magnetic properties and their recognized biocompatibility. Although some nanomaterials are already commercialized and used in medicine, the perspectives for their future use can be foreseen to increase greatly, given also the funded programs around the world.

In this thesis, two magneto-plasmonic nanosystems for application in cancer research were presented. The first one consisting of gold and iron oxide aggregates and the second one of a core-shell-satellite type structure, with core iron oxide nanoparticles, a silica shell and satellite gold nanoparticles. The two nanostructures were obtained with nanoparticles synthesized with a green technique like the laser ablation in water. Clearly, these materials decrease harmful consequences that can be produced by reagents used in other type of nanoparticles synthesis and that can be found in the final products.

Magneto-plasmonic nano-aggregates were simply assembled by controlling surface charges on nanoparticles and were used for cell labeling and guiding. A more engineered core-shell-satellite nanostructure was also obtained and found to be efficient both for immunomagnetic sorting and for photothermal treatment of cancer cells. We quantified their efficiency and found that such a nanostructures can be used for both diagnostic and therapy purposes, namely as theranostic agents.

The work presented in this thesis can be considered one step closer to the use of highly pure nanostructured materials for diagnosis and treatment of diseases.

Publications and conferences

Publications

F. Bertorelle, M. Ceccarello, M. Pinto, G. Fracasso, D. Badocco, V. Amendola, P. Pastore, M. Colombatti and M. Meneghetti, Efficient AuFeO_x Nanoclusters of Laser-Ablated Nanoparticles in Water for Cells Guiding and Surface-Enhanced Resonance Raman Scattering Imaging, *J Phys Chem C*, 2014, **118**, 14534-14541.

Fabrizio Bertorelle, Marcella Pinto, Lucio Litti, Stefania Fiameni, Vincenzo Amendola, Giamaica Conti, Giuseppe Toffoli, Marco Colombatti, Giulio Fracasso, Moreno Meneghetti; Multivalence Activity of a Core-Shell-Satellite Structure Synthesized with a Green Approach for a SERS Verified Efficient Identification of Cancer Cells, 2016, *Submitted*.

F. Bertorelle, M. Pinto, R. Zapon, R. Pilot, L. Litti, S. Fiameni, M. Colombatti, G. Fracasso, M. Meneghetti; Core-shell-satellite nanostructures synthesized with a green method and their efficient use in photothermal treatment of cancer cells, 2016, *In preparation*.

Conferences

* Presenting author

Conference: Inside Raman, 8th-9th april 2014, Manchester, Poster Presentation

Authors: Fabrizio Bertorelle*, Marcella Pinto, Giulio Fracasso, Vincenzo Amendola, Marco Colombatti, Moreno Meneghetti

Title: AuFeO_x Nanoclusters for Biomedical Applications Using their Superparamagnetic and SERS Properties

Conference: GISR 2014, III Italian Meeting on Raman Spectroscopy and Non-Linear Optical Effects, Parma 9th-11th june 2014, Poster presentation

Authors: Fabrizio Bertorelle*, Marcella Pinto, Giulio Fracasso, Vincenzo Amendola, Marco Colombatti, Moreno Meneghetti

Title: Efficient Plasmonic/Magnetic AuFeO_x Nanoclusters for Cells Guiding and SERRS Imaging

Conference: European Material Research Society, EMRS Lille Spring Meeting 2015, Invited Oral Presentation, Symposium V, Lille (FR) 14th may 2015

Authors: Fabrizio Bertorelle*, Marcella Pinto, Giulio Fracasso, Vincenzo Amendola, Marco Colombatti, Moreno Meneghetti

Title: Design and synthesis of FeO_x NP@dye-doped MPTMS@AuNP core-shell-satellite nanosystems for SERS detection and immunomagnetic sorting of cancer cells

Conference: European Material Research Society, EMRS Lille Spring Meeting 2015, Poster presentation, Symposium V poster session, Lille (FR) may 2015

Authors: Fabrizio Bertorelle*, Marcella Pinto, Giulio Fracasso, Vincenzo Amendola, Marco Colombatti, Moreno Meneghetti

Title: Design and synthesis of FeO_x NP@dye-doped MPTMS@AuNP core-shell-satellite nanosystems for SERS detection and immunomagnetic sorting of cancer cells

Conference: Plasmonica 2015, July 2015, Padova, Poster Presentation

Authors: Fabrizio Bertorelle*, Marcella Pinto, Giulio Fracasso, Vincenzo Amendola, Marco Colombatti, Moreno Meneghetti

Title: Design and synthesis of FeO_x NP@dye-doped MPTMS@AuNP core-shell-satellite nanosystems for SERS detection and immunomagnetic sorting of cancer cells

Conference: Plasmonica 2015, July 2015, Padova, Oral Presentation

Authors: Vincenzo Amendola*, Rosalba Saija, Onofrio Maragò, Antonella Iatì, Stefano Scaramuzza, Annamaria Poletti, Fabrizio Bertorelle, Andrea Colusso, Lucio Litti, Moreno Meneghetti

Title: Innovative plasmonic nanostructures generated by laser ablation in liquid solution: magnetic-plasmonic nanoparticles for biomedical applications and Au-Fe nanoalloys with superior plasmon absorption

Conference: European Material Research Society, E-MRS spring meeting 2016, Symposium R : Multifunctional nanostructures for diagnostic and therapeutic of diseases of the E-MRS 2016 Spring Meeting, Lille (FR) from May 2 to 6, 2016. Poster presentation.

Authors: Fabrizio Bertorelle*, Marcella Pinto, Roberta Zappon, Robertino Pilot, Lucio Litti, Vincenzo Amendola, Marco Colombatti, Giulio Fracasso and Moreno Meneghetti

Title: A sub-micron architecture for efficient immunomagnetic sorting, SERS detection and photothermal treatment of cancer cells

Conference: 4th Conference on Advanced Nanoparticle Generation and Excitation by Lasers in Liquids (ANGEL) from 09 - 12 May 2016, Essen (DE). Oral presentation.

Authors: Fabrizio Bertorelle*, Marcella Pinto, Robertino Pilot, Lucio Litti, Stefania Fiameni, Vincenzo Amendola, Giamaica Conti, Giuseppe Toffoli, Marco Colombatti, Giulio Fracasso, Moreno Meneghetti

Title: Laser Ablated gold and iron oxide nanoparticles arranged in a core-shell-satellite architecture for efficient immunomagnetic sorting, SERS detection and photothermal treatment of cancer cells

Conclusion

Conference: GISR 2016, Italian Meeting on Raman Spectroscopies and Non Linear Optical Effects, Padova, 14-16 september 2016, Poster presentation.

Authors: Fabrizio Bertorelle*, Marcella Pinto, Roberta Zappon, Robertino Pilot, Lucio Litti, Vincenzo Amendola, Marco Colombatti, Giulio Fracasso and Moreno Meneghetti

Title: A sub-micron architecture for efficient immunomagnetic sorting, SERS detection and photothermal treatment of cancer cells

Aknowledgements

I would thank the Ph.D school in Materials Science and Engineering and the Nanostructures and Optics Laboratory (NOL) group leaded by prof. Moreno Meneghetti for the support in the realization of the project presented in this thesis.

The entire work has been possible also thanks to the collaboration of my friends and colleagues Dr. Andrea Colusso, Dr. Lucio Litti, Dr. Stefano Scaramuzza and Dr. Vincenzo Amendola.

For the realization of all experiments with cells special thanks goes to Dr. Marco Colombatti, Dr. Giulio Fracasso and Dr. Marcella Pinto from the immunology section of “Policlinico G.B. Rossi” of the University of Verona.

For the realization of photothermal experiments I would like to thank Dr. Roberto Pilot from University of Padova (Department of Chemical Sciences) for help in the optimization of laser setup.

I would also thank all undergraduate students that actively participated in the realization of this project: Dr. Martina Ceccarello and Dr. Giovanni Bressan. From this last group, a special remark goes to Dr. Roberta Zappon, which I estimate as a friend and colleague, for her precious help in the realization of all photothermal experiments and the “Tuning-the-plasmon-to-NIR” part.

Parts of this project were possible only thanks to the collaboration of: Dr. Francesco Boldrin and Dr. Federico Caicci for TEM images (University of Padova, Department of Biology), Dr. Denis Badocco (University of Padova, Department of Chemical Sciences) and Dr. Stefania Fiameni (National Research Council, Padova) for ICP-MS analysis, Prof. Fabrizio Mancin for the possibility of performing DLS and Z-potential measurements in his lab.